



TEZ ŞABLONU ONAY FORMU  
THESIS TEMPLATE CONFIRMATION FORM

1. Şablonda verilen yerleşim ve boşluklar değiştirilmemelidir.
2. Jüri tarihi Başlık Sayfası, İmza Sayfası, Abstract ve Öz'de ilgili yerlere yazılmalıdır.
3. İmza sayfasında jüri üyelerinin unvanları doğru olarak yazılmalıdır.
4. Tezin son sayfasının sayfa numarası Abstract ve Öz'de ilgili yerlere yazılmalıdır.
5. Bütün chapterlar, referanslar, ekler ve CV sağ sayfada başlamalıdır. Bunun için **kesmeler** kullanılmıştır. **Kesmelerin kayması** fazladan boş sayfaların oluşmasına sebep olabilir. Bu gibi durumlarda paragraf (¶) işaretine tıklayarak kesmeleri görünür hale getirin ve yerlerini **kontrol edin**.
6. Figürler ve tablolar kenar boşluklarına taşmamalıdır.
7. Şablonda yorum olarak eklenen uyarılar dikkatle okunmalı ve uygulanmalıdır.
8. Tez yazdırılmadan önce PDF olarak kaydedilmelidir. Şablonda yorum olarak eklenen uyarılar PDF dokümanında yer almamalıdır.
9. **Bu form aracılığıyla oluşturulan PDF dosyası arkalı-önlü baskı alınarak tek bir spiralli cilt haline getirilmelidir.**
10. Spiralli hale getirilen tez taslağınızdaki ilgili alanları imzalandıktan sonra, [Tez Jüri Atama Formu](#) ile birlikte bölüm sekreterliğine teslim edilmelidir.
11. Tez taslağınız bölüm sekreterliğiniz aracılığıyla format ve görünüm açısından kontrol edilmek üzere FBE'ye ulaştırılacaktır.
12. FBE tarafından kontrol işlemleri tamamlanan tez taslakları, öğrencilere teslim edilmek üzere bölüm sekreterliklerine iletilecektir.
13. Tez taslaklarının kontrol işlemleri tamamlandığında, bu durum öğrencilere METU uzantılı öğrenci e-posta adresleri aracılığıyla duyurulacaktır.
14. Tez taslakları bölüm sekreterlikleri tarafından öğrencilere iletileceği için öğrencilerimizin tez taslaklarını enstitümüzden elden alma konusunda ısrarcı olmamaları beklenmektedir.
15. Tez yazım süreci ile ilgili herhangi bir sıkıntı yaşarsanız, [Sıkça Sorulan Sorular \(SSS\)](#) sayfamızı ziyaret ederek yaşadığınız sıkıntıyla ilgili bir çözüm bulabilirsiniz.
1. Do not change the spacing and placement in the template.
2. Write defense date to the related places given on Title page, Approval page, Abstract and Öz.
3. Write the titles of the examining committee members correctly on Approval Page.
4. Write the page number of the last page in the related places given on Abstract and Öz pages.
5. All chapters, references, appendices and CV must be started on the right page. **Section Breaks** were used for this. **Change in the placement** of section breaks can result in extra blank pages. In such cases, make the section breaks visible by clicking paragraph (¶) mark and **check their position**.
6. All figures and tables must be given inside the page. Nothing must appear in the margins.
7. All the warnings given on the comments section through the thesis template must be read and applied.
8. Save your thesis as pdf and Disable all the comments before taking the printout.
9. **Print two-sided the PDF file that you have created through this form and make a single spiral bound.**
10. Once you have signed the relevant fields in your thesis draft that you spiraled, submit it to the department secretary together with your [Thesis Jury Assignment Form](#).
11. Your thesis draft will be delivered to the GSNAS via your department secretary for controlling in terms of format and appearance.
12. The thesis drafts that are controlled by GSNAS, will be sent to the department secretary to be delivered to the students.
13. This will be announced to the students via their METU students e-mail addresses when the control of the thesis drafts has been completed.
14. As the thesis drafts will be delivered to the students by the department secretaries, we are expecting from our students no to insist about getting their theses drafts from the Institute.
15. If you have any problems with the thesis writing process, you may visit our [Frequently Asked Questions \(FAQ\)](#) page and find a solution to your problem.

Yukarıda bulunan tüm maddeleri okudum, anladım ve kabul ediyorum. / I have read, understand and accept all of the items above.

Name : Seçil  
Surname : Güler  
E-Mail : [secil.guler@metu.edu.tr](mailto:secil.guler@metu.edu.tr)  
Date : 20.01.2020  
Signature : \_\_\_\_\_



A THESIS SUBMITTED TO  
THE GRADUATE SCHOOL OF NATURAL AND APPLIED SCIENCES  
OF  
MIDDLE EAST TECHNICAL UNIVERSITY

BY  
SEÇİL GÜLER

IN PARTIAL FULFILLMENT OF THE REQUIREMENTS  
FOR  
THE DEGREE OF MASTER OF SCIENCE  
IN  
PHYSICS

JANUARY 2020



Approval of the thesis:

**CHARACTERIZATION AND CONTACT RESISTIVITY STUDIES OF ITO THIN FILMS FOR USE IN SILICON HETEROJUNCTION SOLAR CELLS**

submitted by **SEÇİL GÜLER** in partial fulfillment of the requirements for the degree of **Master of Science in Physics, Middle East Technical University** by,

Prof. Dr. Halil Kalıpçılar  
Dean, Graduate School of **Natural and Applied Sciences**

\_\_\_\_\_

Prof. Dr. Altuğ Özpıneci  
Head of the Department, **Physics**

\_\_\_\_\_

Prof. Dr. A. Çıđdem Erçelebi  
Supervisor, **Physics, METU**

\_\_\_\_\_

Prof. Dr. Raşıit Turan  
Co-Supervisor, **Physics, METU**

\_\_\_\_\_

**Examining Committee Members:**

Prof. Dr. Mehmet Parlak  
Physics, METU

\_\_\_\_\_

Prof. Dr. A. Çıđdem Erçelebi  
Physics, METU

\_\_\_\_\_

Prof. Dr. Raşıit Turan  
Physics, METU

\_\_\_\_\_

Prof. Dr. Nurdan Demirci Sankır  
Material Science and Nanotechnology Engineering, TOBB ETU

\_\_\_\_\_

Assist. Prof. Dr. Gülsen Baytemir  
Engineering and Natural Sciences, Maltepe University

\_\_\_\_\_

Date: 20.01.2020

**I hereby declare that all information in this document has been obtained and presented in accordance with academic rules and ethical conduct. I also declare that, as required by these rules and conduct, I have fully cited and referenced all material and results that are not original to this work.**

Name, Last name: Seil Gler

Signature:

## ABSTRACT

### CHARACTERIZATION AND CONTACT RESISTIVITY STUDIES OF ITO THIN FILMS FOR USE IN SILICON HETEROJUNCTION SOLAR CELLS

GÜLER, Seçil

Master of Science, Physics

Supervisor: Prof. Dr. A. Çiğdem Erçelebi

Co-Supervisor: Prof. Dr. Raşit Turan

January 2020, 105 pages

Transparent conductive oxides (TCO) are widely used in optoelectronic devices such as flat panel displays and solar cells. Indium tin oxide, due to its wide optical bandgap and high transmittance in the visible spectrum, is commonly used for device applications such as anti-reflective coating, front TCO layer in silicon heterojunction solar cells. When ITO is used as TCO layer, the carrier transport mechanism through the junction is improved due to the decrease in the free carrier absorption. In this study, the effect of deposition conditions of ITO thin films on the material properties, as well as the material optimization towards the decrease of resistivity and carrier concentration simultaneously and the increase of the transparency and mobility values have been investigated. In order to achieve this goal, ITO thin films with various thicknesses were deposited on borosilicate glass substrates and n type silicon wafers by RF (Radio Frequency) magnetron sputtering using different deposition conditions. The main sputtering parameters were the sputtering power, substrate temperature, deposition pressure and oxygen content in the gas mixture. ITO films deposited under different conditions have been characterized in order to determine the optimum deposition parameters leading to ITO thin films with high conductivity,

high transmittance in the visible range as well as the low carrier concentration. The structural, morphological, electrical and optical properties of the deposited ITO films have been characterized by X-Ray Diffraction, Atomic Force Microscopy (AFM), four-point-probe, Hall Effect and spectrophotometric measurement techniques.

Besides the optimization studies of ITO thin films for Silicon Heterojunction Solar Cells, the specific contact resistivity studies between ITO and different layers in SHJ structure have been also carried out by using one dimensional transfer length method (1D-TLM).

In the last part of the thesis study, different optimized ITO layers were deposited as an anti-reflective coating layer in SHJ solar cells and effect of ITO film properties on SHJ cell parameters have been investigated.

**Keywords:** Transparent conductive oxide(TCO), indium tin oxide(ITO), silicon heterojunction solar cells, specific contact resistivity.

## ÖZ

### SİLİSYUM HETEROEKLEM GÜNEŞ HÜCRELERİNDE KULLANILAN İNDİYUM KALAY OKSİT İNCE FİMLERİNİN KARAKTERİZASYONU VE KONTAK DİRENCİ ÇALIŞMALARI

GÜLER, Seçil  
Yüksek Lisans, Fizik  
Tez Yöneticisi: Prof. Dr.A. Çiğdem Erçelebi  
Ortak Tez Yöneticisi: Prof.Dr. Raşit Turan

Ocak 2020, 105 sayfa

Şeffaf iletken oksitler düz panel ekranlar ve güneş pilleri gibi optoelektronik cihazlarda yaygın olarak kullanılmaktadır. İndiyum kalay oksit(ITO) görünür spektrumda geniş optik bant aralığı ve yüksek geçirgenliği nedeniyle, silisyum heteroeklem güneş hücreleri gibi aygıt uygulamalarında yansıma önleyici ön kaplama tabakası olarak kullanılmaktadır. ITO şeffaf iletken oksit tabakası olarak kullanıldığında, serbest taşıyıcı soğurmasını azaltmasından dolayı eklemdeki taşıyıcı transport mekanizması iyileşmektedir. Bu çalışmada, üretim parametrelerinin indiyum kalay oksit ince filmlerin özellikleri üzerindeki etkileri araştırılmaktadır ve düşük öz direnç, yüksek taşıyıcı yoğunluğu ve aynı zamanda yüksek mobilite ve optik geçirgenlik değerlerine sahip ince filmler elde edilmesine yönelik araştırmalar sürdürülmektedir. Bu değerlere ulaşmak için, farklı kalınlıktaki ITO ince filmler, farklı kaplama parametreleri kullanılarak borosilikat cam alttaşlar üzerine radyo frekansı(RF) saçırma sistemi ile kaplanmıştır. Temel üretim parametreleri RF gücü, kaplama basıncı, alttaş sıcaklığı ve gaz karışımındaki oksijen miktarıdır. Yüksek iletkenliğe, görünür bölgede yüksek geçirgenliğe ve düşük taşıyıcı yoğunluğuna sahip farklı koşullar altında üretilen ITO ince filmler; optimum üretim parametrelerinin ve malzeme özelliklerinin belirlenmesi için yapısal, morfolojik,

elektriksel ve optik özelliklerine yönelik olarak, X-Işını Kırınımı, Atomik Kuvvet Mikroskobu(AFM), dört nokta temaslı iletkenlik ölçüm sistemi ve spektrofotometrik ölçüm teknikleri kullanılarak karakterize edilmiştir. ITO ince filmlerinin karakterizasyon çalışmalarının yanı sıra, ITO / n-a Si: H ve ITO / p-a Si: H tabakaları arasındaki spesifik kontak dirençlerini azaltmak için, bu tabakalar arasındaki kontak direnci çalışmaları bir boyutlu transfer uzunluğu modeli(1D-TLM) yöntemi ile yapılmıştır.

Bu çalışmanın son kısmında, optimize edilen ITO ince filmleri, silikon heteroeklem güneş hücrelerinde yansıma önleyici tabaka olarak kaplanmış, ITO ince film özelliklerinin güneş hücrelerinin verim değerleri üzerindeki etkisi incelenmiştir.

Anahtar Kelimeler: Şeffaf iletken oksitler, indiyum kalay oksit, silisyum heteroeklem güneş pilleri, spesifik kontak direnci.

## Dedication

To my family and to my grandfather..

## ACKNOWLEDGMENTS

First of all, I would like to thank my supervisor Prof. Dr. Çiğdem Erçelebi. During my master's studies, she always encouraged me. I appreciated her patience. I learnt many things from her both experimentally and theoretically. She was always kind to me during my whole graduate study. Also, I would like to thank my co-supervisor Prof. Dr. Raşit Turan for his guidance and precious advices to my thesis studies. Moreover, I want to thank my daily supervisor Ergi Dönerçark. He helped me to acquire experimental know-how gain. I am also grateful to my colleague Hande Çiftçınar for her fellowship and precious contributions to my thesis studies. I would like to thank my friend and GÜNAM member Merve Demir for her great friendship. Besides, I would like to thank all GÜNAM employees, especially technicians Yücel Eke and Nevzat Görmez for their unique technical supports. Also, I am grateful to Buket Gökbakan for her unique friendship.

I would like to thank my family, especially my father. He supports me every time and he taught me never give up.

Special thanks go to my "partner" Deniz Bilgin. She always supports me during my graduate studies and she never left me alone in my hard times and also Beyza Durusoy; from our bachelor period, she was my positive side and she was always with me. I want to thank my best friend Fethiye Irmak Doğan. Even though the distances, I felt her presence in my side. I am also grateful to my special sisters Elif Bekoğlu and Merve Eşdur for their support and solidarity. Also, I wish to thank my flatmate Çiğdem Ekiz for creating peaceful atmosphere in our home. In addition, I would like to thank my friends Baran Yeşiltepe, Efe Arın and Hüsnü Şener. We had a lot of fun within these three years, even my stressful times.

I want to thank my special and precious friend Vassily Burwitz for his endless support.

Lastly, I would like to mention that this thesis was supported by TÜBİTAK Project numbered as 217M087.

## TABLE OF CONTENTS

<b>ABSTRACT</b>	<b>v</b>
<b>ÖZ</b>	<b>vii</b>
<b>ACKNOWLEDGMENTS</b> .....	<b>x</b>
<b>TABLE OF CONTENTS</b> .....	<b>xi</b>
<b>LIST OF TABLES</b> .....	<b>xiv</b>
<b>LIST OF FIGURES</b> .....	<b>xvi</b>
<b>LIST OF ABBREVIATIONS</b> .....	<b>xix</b>
<b>LIST OF SYMBOLS</b> .....	<b>xxi</b>
<b>CHAPTERS</b>	
<b>1 INTRODUCTION</b> .....	<b>1</b>
1.1 Types of Solar Cells .....	1
1.2 Silicon Heterojunction Solar Cells .....	4
1.3 TCO Layer and SHJ Solar Cells.....	5
1.4 Specific Contact Resistivity and SHJ Solar Cells .....	6
<b>2 THEORETICAL BACKGROUND</b> .....	<b>9</b>
2.1 Fundamental Information about Sun and Solar Cells.....	9
2.1.1 Solar Irradiance .....	9
2.1.2 Working Mechanism of Solar Cell.....	10
2.2 Silicon Heterojunction (SHJ) Solar Cells .....	15
2.2.1 ITO and SHJ Solar Cells.....	17
2.3 Transparent Conductive Oxides (TCO).....	18

2.3.1	Mobility and Scattering Mechanisms of TCO .....	20
2.3.2	Indium Tin Oxide (ITO) .....	22
2.4	Contact Resistivity Analysis .....	24
2.4.1	Metal Semiconductor Contacts .....	24
2.4.2	Contact Resistivity and Contact Resistance .....	28
<b>3 EXPERIMENTAL PROCEDURE AND CHARACTERIZATION</b>		
<b>TECHNIQUES</b>		<b>33</b>
3.1	Introduction .....	33
3.2	Sample Preparation and Cleaning Procedures .....	33
3.3	Deposition of doped a-Si:H layers by using PECVD .....	34
3.4	Deposition of ITO Thin Films by Sputtering .....	37
3.5	Characterization of ITO Thin Films .....	41
3.5.1	Four Point Probe .....	41
3.5.2	X Ray Diffraction Analysis .....	42
3.5.3	Atomic Force Microscopy .....	43
3.5.4	Transmission & EQE Measurements .....	44
3.5.5	EQE Measurements .....	46
3.5.6	Hall Effect Measurement .....	46
3.5.7	Spectroscopic Ellipsometry (SE) .....	48
3.6	Contact Resistivity Analysis .....	49
3.6.1	Metallization by Thermal Evaporation .....	51
3.6.2	Current –Voltage Measurements in Dark Condition .....	52
<b>4 RESULTS AND DISCUSSION</b>		<b>55</b>
4.1	Introduction .....	55
4.2	Electrical Characterizations .....	55

4.2.1	Change of resistivity with RF Power and Substrate Temperature ....	55
4.2.2	Effect of Oxygen/Argon Ratio on the Resistivity of the ITO Films ..	61
4.1.3	Effect of Deposition Rate and Deposition Pressure on the Resistivity ..	65
4.2.3	Mobility and Scattering Mechanisms .....	69
4.3	Structural Characterization .....	72
4.3.1	XRD Measurement Results.....	72
4.4	AFM Measurements .....	76
4.5	Optical Measurements .....	80
4.5.1	UV-Visible Spectra .....	80
4.6	Contact Resistivity Analysis .....	86
4.6.1	Contact Resistivity Measurements by TLM .....	87
4.7	SHJ Cells Results .....	91
<b>5</b>	<b>CONCLUSION .....</b>	<b>95</b>
	<b>REFERENCES</b>	<b>97</b>

## LIST OF TABLES

### TABLES

<b>Table 3.1</b> Deposition parameters of a Si: H layers by PECVD. ....	36
<b>Table 3.2</b> Deposition Parameters of ITO Thin Films with different power and substrate temperatures.....	40
<b>Table 3.3</b> Deposition parameters of ITO thin films with different Ar/oxygen ratio. ....	40
<b>Table 3.4</b> Deposition parameters of ITO thin films with different deposition pressure and robot arm speed.....	41
<b>Table 4.1</b> Sheet resistance and resistivity results of ITO1 samples before and after annealing. ....	56
<b>Table 4.2</b> Sheet resistance and resistivity results ITO2 samples before and after annealing. ....	56
<b>Table 4.3</b> Sheet resistance and resistivity results of ITO3 samples before and after annealing. ....	57
<b>Table 4.4</b> Sheet resistance and resistivity results of ITO4 samples before and after annealing. ....	58
<b>Table 4.5</b> Sheet resistance and resistivity results of ITO5 samples before and after annealing. ....	58
<b>Table 4.6</b> Sheet resistance and resistivity results of ITO6 samples before and after annealing. ....	59
<b>Table 4.7</b> Sheet resistance and resistivity results of ITO10 samples before and after annealing. ....	61
<b>Table 4.8</b> Sheet resistance and resistivity results of ITO11 samples before and after annealing. ....	62
<b>Table 4.9</b> Sheet resistance and resistivity results ITO12 samples before and after annealing. ....	62

<b>Table 4.10</b> Sheet resistance and resistivity results of ITO13 samples before and after annealing. ....	63
<b>Table 4.11</b> Sheet resistance and resistivity results of ITO17 samples before and after annealing. ....	63
<b>Table 4.12</b> Sheet resistance and resistivity results of ITO23 samples before and after annealing. ....	64
<b>Table 4.13</b> Sheet resistance and resistivity results of ITO20 samples before and after annealing. ....	66
<b>Table 4.14</b> Sheet resistance and resistivity results of ITO21 samples before and after annealing. ....	67
<b>Table 4.15</b> Sheet resistance and resistivity results of ITO22 samples before and after annealing. ....	68
<b>Table 4.16</b> Mobility, carrier density, Hall coefficient and resistivity of ITO thin films with different deposition parameters. ....	71
<b>Table 4.17</b> Mobility, carrier density, Hall coefficient and resistivity with respect to different oxygen content. ....	72
<b>Table 4.18</b> Crystallite size, interplanar distance and FWHM values of deposited films. ....	76
<b>Table 4.19</b> Surface Roughness values of ITO films with and without post annealing. ....	80
<b>Table 4.20</b> Optical Bandgap values as deposited ITO films without oxygen. ....	84
<b>Table 4.21</b> Optical bandgap of grown ITO Thin films grown with different O <sub>2</sub> / Ar ratio. ....	86
<b>Table 4.22</b> Transfer length, contact resistance and contact resistivity of ITO/Ag layer. ....	90

## LIST OF FIGURES

### FIGURES

<b>Figure 1.1.</b> Poly <b>(a)</b> and Monocrystalline <b>(b)</b> Silicon solar cells [3].	2
<b>Figure 1.2.</b> CIGS Thin Film Solar Cells [6]	2
<b>Figure 1.3.</b> Dye Synthesized solar cells [10]	3
<b>Figure 1.4</b> Best cell efficiencies [11].	4
<b>Figure 1.5</b> HIT solar cell structure developed by Sanyo [17]	5
<b>Figure 2.1.</b> Solar radiation spectrum at the earth’s surface [34]	9
<b>Figure 2.2</b> Energy band diagram of a p – n junction under thermal-equilibrium..	11
<b>Figure 2.3</b> Equivalent circuit model of solar cell [36].	12
<b>Figure 2.4</b> I-V characteristic of solar cell in dark and under illumination [37]	13
<b>Figure 2.5</b> External Quantum Efficiency graph.	14
<b>Figure 2.6</b> Schematic diagram of a Silicon Heterojunction Solar Cells [39].	16
<b>Figure 2.7</b> Schematic band diagram of silicon heterojunction solar cell based on n type FZ c-Si wafer [40].	17
<b>Figure 2.8</b> Interface between ITO and p a-Si:H layer [42].	18
<b>Figure 2.9</b> Transmission, Reflection and Absorption spectrum of ZnO, adapted from [33].	20
<b>Figure 2.10</b> The cubic bixbyite structure of In <sub>2</sub> O <sub>3</sub> [57].	23
<b>Figure 2.11</b> Conduction mechanism of metal – semiconductor (n type) interaction depending on the doping concentration [60].	25
<b>Figure 2.12.</b> Ohmic contact formation for n and p type semiconductors, <b>(a)</b> p type semiconductor, <b>(b)</b> n type semiconductor [61].	26
<b>Figure 2.13.</b> Schotkky contact formation for p and n type semiconductors, <b>(a)</b> p type semiconductor, <b>(b)</b> n type semiconductor [62]	28
<b>Figure 2.14.</b> <b>(a)</b> Current flow path between the two contacts <b>(b)</b> rectangular TLM pattern.	30
<b>Figure 2.15.</b> Plot of total resistance as a function of contact spacing where d1 and d2, d3 show different contact spacing.	31

<b>Figure 3.1.</b> Schematic representation of PECVD chamber. ....	35
<b>Figure 3.2</b> Schematic configuration of GÜNER System [69]. ....	37
<b>Figure 3.3</b> Representation of sputtering process. ....	38
<b>Figure 3.4</b> Schematic configuration of RF magnetron sputtering system. ....	39
<b>Figure 3.5</b> Schematic configuration of four point probe system. ....	42
<b>Figure 3.6</b> Schematic configuration of GI-XRD system. ....	43
<b>Figure 3.7</b> Configuration of Atomic Force Microscopy at Central Laboratory. ....	44
<b>Figure 3.8</b> Perkin Elmer Lambda 45 Spectrophotometer. ....	45
<b>Figure 3.9</b> PVE300 Bentham device [70] . ....	46
<b>Figure 3.10</b> Hall Effect Measurement System. ....	48
<b>Figure 3.11</b> Schematic configuration of Spectroscopic Ellipsometry ....	49
<b>Figure 3.12</b> The test structures used to determine ITO/Ag contact resistivity. ....	50
<b>Figure 3.13</b> The test structures with passivating i and p a-Si:H layers. ....	51
<b>Figure 3.14</b> Prepared shadow masks for TLM measurements. Mask 1 design is adapted from [73]. ....	51
<b>Figure 3.15</b> Schematic representation of thermal evaporation system [36]. ....	52
<b>Figure 3.16</b> Solar Simulator System. ....	53
<b>Figure 4.1</b> Change of resistivity with RF Power (for samples <i>ITO6</i> , <i>ITO5</i> and <i>ITO4</i> ). ....	60
<b>Figure 4.2</b> Resistivity values at different annealing temperatures. ....	60
<b>Figure 4.3</b> Change of resistivity with $O_2/Ar$ ratio. ....	64
<b>Figure 4.4</b> Resistivity values with respect to different robot arm speed. ....	67
<b>Figure 4.5</b> Change of resistivity with respect to different deposition pressure. ....	68
<b>Figure 4.6</b> XRD Pattern of <i>ITO4</i> film with different annealing temperature. ....	73
<b>Figure 4.7</b> XRD pattern of <i>ITO12</i> (1 % $O_2/Ar$ ratio) sample with different annealing temperature. ....	74
<b>Figure 4.8</b> XRD Pattern of <i>ITO23</i> (0.4 % $O_2/Ar$ ratio) sample. ....	75
<b>Figure 4.9</b> XRD Pattern of ITO Thin Films ( As deposited <i>ITO4</i> , <i>ITO23</i> , <i>ITO12</i> ) ....	75

<b>Figure 4.10</b> AFM Image of ITO4(reference) sample <b>(a)</b> without annealing, <b>(b)</b> annealed at 225 °C. ....	77
<b>Figure 4.11</b> AFM Image of ITO12 sample grown with 1 % O <sub>2</sub> /Ar ratio <b>(a)</b> without annealing, <b>(b)</b> annealed at 225 °C.....	78
<b>Figure 4.12</b> AFM Image of ITO23 sample grown with 0.4% O <sub>2</sub> /Ar ratio <b>(a)</b> without annealing, <b>(b)</b> annealed at 225 ° C.....	79
<b>Figure 4.13</b> Transmission <b>(a)</b> and Absorption <b>(b)</b> Spectra of ITO4, ITO5 and ITO6 samples.....	81
<b>Figure 4.14</b> Transmission <b>(a)</b> and Absorption <b>(b)</b> Spectra of ITO films grown with different Oxygen/Ar ratio.....	82
<b>Figure 4.15</b> Tauc plot of ITO4 <b>(a)</b> and ITO5 <b>(b)</b> samples. ....	83
<b>Figure 4.16</b> Tauc Plot of ITO6 sample. ....	83
<b>Figure 4.17</b> Tauc Plot of ITO10 <b>(a)</b> and ITO11 <b>(b)</b> samples. ....	85
<b>Figure 4.18</b> Tauc Plot of ITO12 <b>(a)</b> and ITO17 <b>(b)</b> samples. ....	85
<b>Figure 4.19</b> I-V characteristic of TLM patterns with different contact diameters. ....	87
<b>Figure 4.20</b> <b>(a)</b> and <b>(b)</b> Resistance vs. contact separation graphs <b>(c)</b> designed test structure, <b>(d)</b> contact designs.....	88
<b>Figure 4.21</b> <b>(a)</b> I-V measurements of TLM test structure with passivating layer for ITO/Ag layer <b>(b)</b> Resistance vs Distance graph, <b>(c)</b> cross view of test structure. ..	89
<b>Figure 4.22</b> <b>(a)</b> I-V characteristic of TLM test structure with passivating layer to determine specific contact resistivity of ITO/p a-Si:H layer.....	91
<b>Figure 4.23</b> EQE results of SHJ cells deposited with different ITO layer. ....	92
<b>Figure 4.24</b> I-V characteristic of SHJ cells deposited with different ITO layer.....	93

## **LIST OF ABBREVIATIONS**

### **ABBREVIATIONS**

Silicon Heterojunction (SHJ)

Indium Tin Oxide (ITO)

Transparent Conductive Oxide (TCO)

RF (Radio frequency)

AM (Air mass)

Transfer Length Method (TLM)

Photovoltaic (PV)

CIGS (Copper Indium Gallium Selenide)

DSSC (Dye synthesized solar cells)

RCA (Radio Corporation of America)

XRD (X-Ray Diffraction)

AFM (Atomic Force Microscopy)

Sccm (standard cubic centimeter per minute)

HIT (Heterojunction with intrinsic thin layer)

PECVD (Plasma Enhanced Chemical Vapour Depositon)

EQE (External Quantum Efficiency)

FF (Fill Factor)

FZ (Float Zone)

RMS (Root mean square)

PVD (Physical Vapour Deposition)

FWHM (Full Width of Half Maximum)

a.u (arbitrary unit)

BSF (Back surface field)

IQE (Internal quantum efficiency)

NIR (Near infrared region)

CZ (Czochralski)

## LIST OF SYMBOLS

### SYMBOLS

$V_{oc}$ : Open circuit voltage

$J_{sc}$ : Short circuit current density

$\alpha$ : absorption coefficient

a-Si:H: Hydrogenated amorphous silicon

$\mu$ : Mobility

$\lambda$ : wavelength

$h$ : Planck constant

c-Si: Crystal silicon

$R_{shunt}$ : Shunt resistance

$V_d$ : Drift Velocity

$R_c$ : Contact resistance

$L_T$ : Transfer Length

$R_{series}$ : Series resistance

$R_{sh}$ : Sheet resistance

$q$ : electronic charge

$\nu$ : applied frequency

B: corrected peak width

t: thickness

d: interplanar distance

$R_H$ : Hall coefficient

J: Current density

n: Carrier concentration

$\sigma$ : Conductivity

$\eta$ : Efficiency

$I_0$ : Intensity of incident light

$I_T$ : Intensity of transmitted light

T: Ambient temperature

k: Boltzmann constant

G: Optical generation rate

$N_0$ : Photon flux

SiO<sub>2</sub>: Silicon dioxide

$\phi_M$ : Work function of metal

$\phi_S$ : Work function of semiconductor

$\chi$ : electron affinity

$P_{in}$ : Input power

$V_{mp}$ : Maximum voltage

$I_{mp}$ : Maximum current

$I_{light}$ : Light generated current

$I_0$ : Reverse saturation current

$E_c$ : Conduction band level

$E_v$ : Valance band level

$V_{bi}$ : Built in potential

$V$ : Applied voltage

$I_{sc}$ : Short circuit current

KOH: Potassium Hydroxide

HF: Hydroflouric acid

$m^*$ : effective mass

$\tau$ : relaxation time

$l$ : mean free path

$\epsilon$ : permittivity of free space

$E_b$ : Potential barrier height

Sn: Tin

$\phi_{b0}$ : Front contact barrier height

$E_a$ : Activation energy

$\rho$ : Complex reflectance ratio

$E_{sbb}$ : Surface band bending



## **CHAPTER 1**

### **INTRODUCTION**

The study of the photovoltaic (PV) devices goes back to 1839. Photovoltaic Effect was discovered by Becquerel in 1839. In 1876, the first PV device was fabricated by William Adams and Richard Day by using hot platinum and selenium [1]. Moreover, in the 1930s, Schotkky discovered the metal – semiconductor barrier concept [2]. After these discoveries, in 1970s, PV devices were started to be used in satellites and space-crafts. However, these PV devices were not cost effective. After the 1980s, PV companies started to seek solutions to decrease PV device costs. The reason is that the people started to seek alternative energy sources in order to supply world's energy consumption. In the last few decades, the use of renewable energy sources has become more important to cope with world's energy problem. PV solar energy is one of the promising energy sources for world's energy consumption. For this reason, it is attracting more attention in the last years.

#### **1.1 Types of Solar Cells**

There are many different types of PV device structures based on different organic and inorganic materials. They are classified as 1<sup>st</sup>, 2<sup>nd</sup> and 3<sup>rd</sup> generation solar cells. First generation solar cells are based on multicrystalline and monocrystalline silicon technologies. Monocrystalline silicon solar cells are more efficient than multicrystalline based in terms of conversion efficiency; however, multicrystalline wafer based solar cells are more cost efficient. Nowadays, silicon-based solar cells have become more dominant in PV markets due to its abundancy and cost

effectiveness. In Figure 1.1, the photograph of mono and multicrystalline wafer-based solar cells are shown.

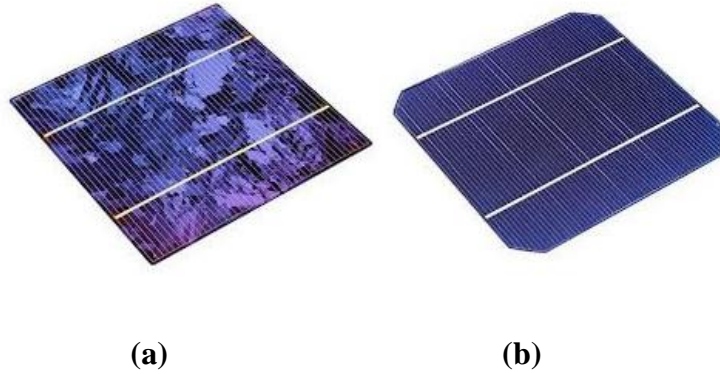


**Figure 1.1.** Poly (a) and Monocrystalline (b) Silicon solar cells [3].

The second generation solar cells are thin film based solar cells and there are many different kind of solar cell including different base materials such as Cadmium Telluride (CdTe), amorphous silicon, Copper Indium Gallium Selenide (CIGS) solar cells (Figure 1.2). Glass and flexible materials can be used as a substrate material for thin film solar cells. Maximum lab efficiency of CIGS thin film solar cells is %22 [4]. The main advantage of thin film solar cells is that their absorber base materials have high absorption coefficient, thus small active layer is enough for the absorption of incoming photons [5]. However, these kind of solar cells suffers from leakage of stability.

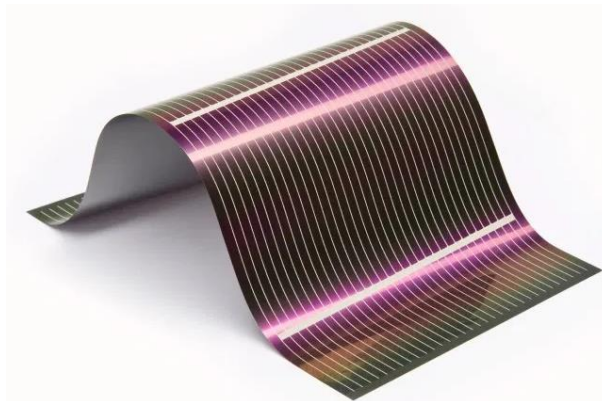


**Figure 1.2.** CIGS Thin Film Solar Cells [6] .

The third generation solar cells cover various organic and inorganic materials and multi junction structures (tandem solar cells). In all structures of the 3<sup>rd</sup> generation solar cells, the target is to produce low cost and efficient devices. Dye synthesized solar cells (DSSC), polymer based solar cells, nanocrystal solar cells and quantum dot solar cells are some kind of 3<sup>rd</sup> generation solar cells (Figure 1.3). Although the production of dye synthesized and organic solar cells is cost effective, efficiency values are low [7]. Besides the use of organic and inorganic materials for the photovoltaic devices, multijunction concept was built up as the 3<sup>rd</sup> generation solar cell concept. According to the Shockley Quessier limit, maximum theoretical efficiency is % 33 for a single p-n junction with bandgap of 1.34 eV at 1.5 AM solar spectrum [8]. For this reason, multijunction concept has been developed to increase the efficiency limit. Nowadays, four terminal multijunction tandem solar cells have reached efficiency of % 47.1 and module efficiency of this structure is expected to increase in the next years [9].

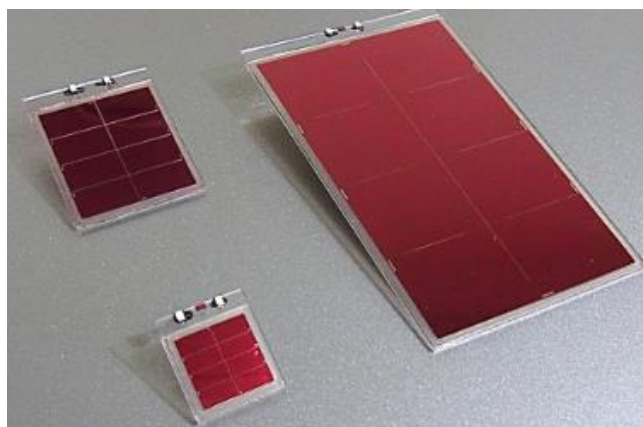


**Figure 1.3.** Dye Synthesized solar cells [10] .

To summarize all kind of solar cells, the graph of Best Research-Cell Efficiencies is given in Figure 1.4, which includes all different kinds of solar cells such as single junction, multi junction and thin film solar cells. It is a well-known graph reported by National Renewable Energy Laboratory (NREL) updated in 2018.

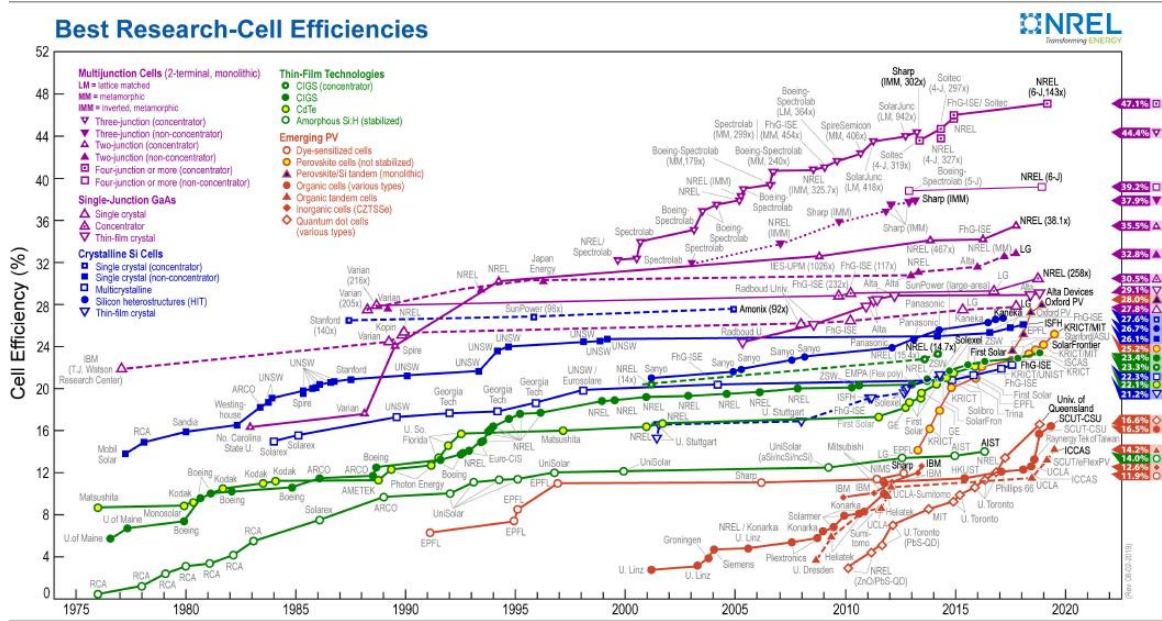
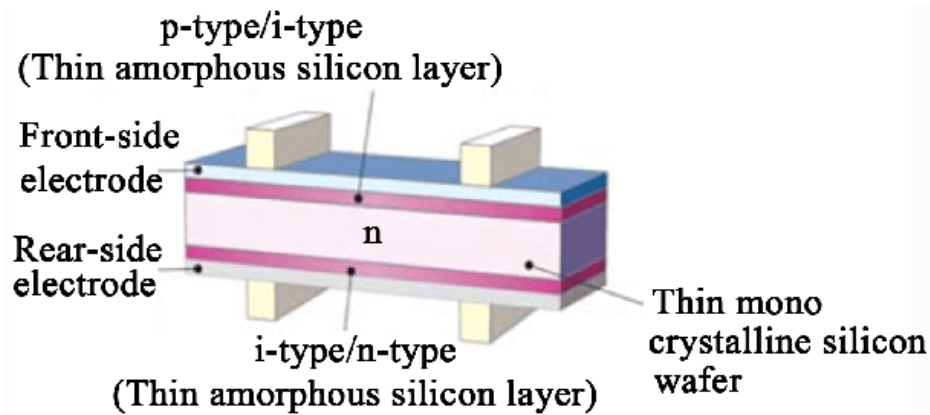


Figure 1.4 Best cell efficiencies [11].

## 1.2 Silicon Heterojunction Solar Cells

Among the silicon solar cells, c-Si and a Si:H heterojunction solar cell structure is still one of the promising technology since it has high open circuit voltage, low temperature process and it is cost efficient. C-Si/a Si:H heterojunction device was first fabricated by Fuhs in 1974 [12]. After this discovery, first Silicon Heterojunction Solar Cell (SHJ) was reported by Hamakawa in 1983 [13]. In 1992, a new heterojunction solar cell concept was developed by Sanyo (now Panasonic) with conversion efficiency of %18.1 [14]. In this structure, c-Si and doped a-Si:H layers were sandwiched between thin intrinsic a-Si:H layers in order to enhance passivation quality. Sanyo commercialized its name as “Heterojunction with Intrinsic Thin layer (HIT)”. In 2015, 25.1 % conversion efficiency was achieved for SHJ solar cells by Kaneka [15]. Moreover, in 2018, world’s record conversion efficiency (26.7 %) was achieved for SHJ-back contact solar cells [16]. In Figure 1.5, HIT structure developed by Sanyo is shown. More detailed structural and theoretical information for HIT solar cells will be given in Chapter 2.



**Figure 1.5** HIT solar cell structure developed by Sanyo [17] .

### 1.3 TCO Layer and SHJ Solar Cells

There are many parameters affecting SHJ device performance. For SHJ solar cells, to improve carrier transport mechanism between c-Si and a-Si:H layers as well as to increase the lateral conductivity of the fingers, optimization and deposition of TCO layer is a crucial step. Transparent conductive oxides have high transparency in the visible range and high electrical conductivity. In 1907, TCOs were reported the first time by Badeker who discovered that cadmium could be transparent as well as conductive when it is oxidized [18]. After that, many different combinations of TCOs were discovered by using different metallic elements. Nowadays, Tin doped Indium Oxide (ITO), Aluminum doped Zinc Oxide (AZO), Fluorine doped Tin Oxide (FTO), Hydrogenated Indium Oxide (IO:H), tungsten doped indium oxides (IWO), Zinc-doped Indium Oxide (IZO) are most frequently used TCO materials [19]. Since TCOs both have high transparency and conductivity, they are used as front electrode for solar cell applications [19]. In addition, they are also suitable for flat panel displays and light emitting diodes (LED) [20]. As an alternative material to TCOs, new conducting and transparent materials have been studied such as nanowires, organic polymers etc. These materials are also used as front electrodes for optoelectronic device applications [21]. Indium Tin Oxide is one of the most commonly used TCO for optoelectronic applications since it has high transparency

and conductivity which was first discovered by Rupprecht in 1954 [22] . It has 85 – 90 % transmittance in the visible range and its lowest resistivity value is in the order of  $10^{-5} \Omega \cdot \text{cm}$  [23]. ITO is also used as the front electrode for solar cell applications especially in SHJ solar cells [24]. However, Indium is an expensive material and its abundance is relatively low compared to other TCO materials. Due to its rareness, recycling process has been applied for Indium [25]. There are many methods to deposit ITO thin films such as spray pyrolysis, thermal evaporation, e-beam evaporation and sputtering. Depending on the deposition condition and deposition method, ITO film properties can be varied [26]. Sputtering technique is one of the most commonly used deposition methods for the growth of ITO films [27].

#### **1.4 Specific Contact Resistivity and SHJ Solar Cells**

For the high efficiency of SHJ solar cells, low contact resistivity is an essential issue since it affects the device performance significantly. Reduction of the negative effect of contact resistivity by decreasing its value, is a significant step to improve the Fill Factor and to optimize  $V_{oc}$  and  $J_{sc}$  values. SHJ solar cells have two extra contact resistances compared to the conventional c-Si cells which are contact resistance of TCO/a-Si:H and contact resistance of a-Si:H/c-Si layers. For this reason, contribution of series resistance to the efficiency is higher than the conventional c-Si solar cells. According to literature, contact resistivity between TCO layer and metal contact is between  $10^{-2}$  and  $10^{-5} \Omega \cdot \text{cm}^2$  [28], while contact resistivity of TCO/a-Si:H layer is in the order of  $\Omega \cdot \text{cm}^2$  [29][30]. There are many methods to measure the specific contact resistivity between different layers in heterojunction structure [31]. To investigate the contact resistivity of intrinsic a-Si:H, doped a-Si:H and ITO layers as well as the ITO and metal contacts, different measurement techniques were upgraded. The most widely used technique to measure the contact resistivity are Transfer Length or Transmission Line Method (TLM). In this study, TLM was used to determine the specific contact resistivity of ITO and metal contact as well as the contact resistivity between a-Si:H and ITO layers.

Transfer Length Method was first discovered by Shockley who introduced a rectangular TLM pattern for use in solar cell current–voltage characteristics [32]. In this study, this method was performed to investigate the specific contact resistivity values between different layers in SHJ structure. Detailed theoretical information about TLM will be given in Chapter 2.

This thesis is consisted of two different parts. First part of the thesis includes the characterization and optimization of ITO thin films for use in SHJ solar cells. In the second part, to investigate the specific contact resistivity of the metal contact, optimized ITO films and a-Si:H layers, different contact resistivity studies were performed by TLM. Lastly, SHJ cells were fabricated by using different optimized ITO layer and the effect of ITO layer on the performance of SHJ solar cells structure was investigated.

This thesis is presented in the following structure: Chapter 2 gives theoretical background information about sun and solar cells, SHJ solar cells, TCOs, properties of ITO, contact formations and Contact Resistivity Methods. In Chapter 3, information about experimental procedure and characterization techniques used in this study will be given. Chapter 4 presents the results and discussions on the ITO characterization, contact resistivity analysis and SHJ cells. Finally, in Chapter 5, the conclusions on the results given in Chapter 4 will be presented.



## CHAPTER 2

### THEORETICAL BACKGROUND

#### 2.1 Fundamental Information about Sun and Solar Cells

##### 2.1.1 Solar Irradiance

Sun is a blackbody with a temperature of around  $5777^{\circ}\text{K}$  [33]. Solar irradiance means power per unit area received from the sun. Solar radiation reaching at the earth's surface is around  $1360 \text{ W/m}^2$ . However, there are some attenuation problems which affects incoming solar radiation to the earth surface through the atmosphere. When incoming light comes through the atmosphere, some of them are scattered or absorbed. The main reason of losses in solar spectrum belongs to absorption of water and  $\text{CO}_2$  molecules in the atmosphere. Solar spectrum of the earth surface is shown in Figure 2.1.

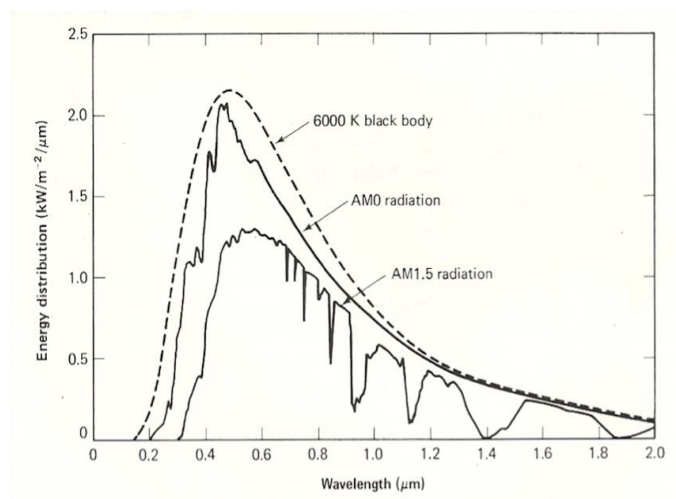


**Figure 2.1.** Solar radiation spectrum at the earth's surface [34] .

In order to examine effect of solar radiation reaching at the earth's surface, air mass (AM) is defined and it is calculated as follows;

$$AM = \frac{\text{optical path length}}{\text{overhead optical path length of the sunlight}} = \frac{1}{\cos \theta}, \quad (\text{Eq. 2.1})$$

where  $\theta$  is the angle between overhead path length of the sunlight and path length of sunlight with respect to its overhead path length before coming to earth surface. When  $\theta=0$ , Air Mass will be equal to 1 and this is called AM1 spectrum. When  $\theta$  is around  $48.2^\circ$ , it is called AM1.5 spectra and which corresponds to sunny and clear day on the earth. AM1.5 spectra is accepted as universal standard. AM1.5 spectra is composed of two parts. AM1.5 "Global" and AM1.5 "Direct". Global spectrum includes both direct and diffuse radiation, while direct spectrum includes only direct radiation. In Figure 2.1 AM1.5 and AM0 spectra are also shown.

### **2.1.2 Working Mechanism of Solar Cell**

Solar cell is an optoelectronic device which converts sunlight into electricity directly by generating both voltage and current. There are three possible ways when incident photon is in contact with the surface of the solar cell; absorption, reflection and transmission. If incoming photons have an energy equal or greater than the bandgap of the bulk material, it is absorbed by the material leading to creation of electron – hole pairs. Absorption of the incident photon is the first step of solar cell operation. Fundamental steps in solar cell operation are light absorption, carrier generation, separation of charge carriers and collection of charge carriers through the metal contact. When the incident photon is absorbed by the base material, absorbed photons create electron hole pairs.

Operation principle of solar cells is explained in the basis of a p-n junction. When p and n type semiconductors are in contact, p-n junction forms. Due to the charge

carrier concentration differences between p and n side, diffusion currents of electrons and holes flow through the junction which creates a space charge region (depletion region) at the junction. Region outside the space charge region is called quasi neutral region. In thermal equilibrium, total net current will be zero through the junction. Separation of charge carriers lead to creation of induced electric field. This internal electric field and fermi level differences result in built in potential  $V_{bi}$ . Diffusion current forms due to the concentration gradient while induced electric field results in drift current of the carriers. Drift and diffusion processes are shown in Figure 2.2 where  $E_c$  and  $E_v$  conduction and valance band levels,  $E_{Fp}$  and  $E_{Fn}$  are the fermi levels of the p and type material in thermal equilibrium.

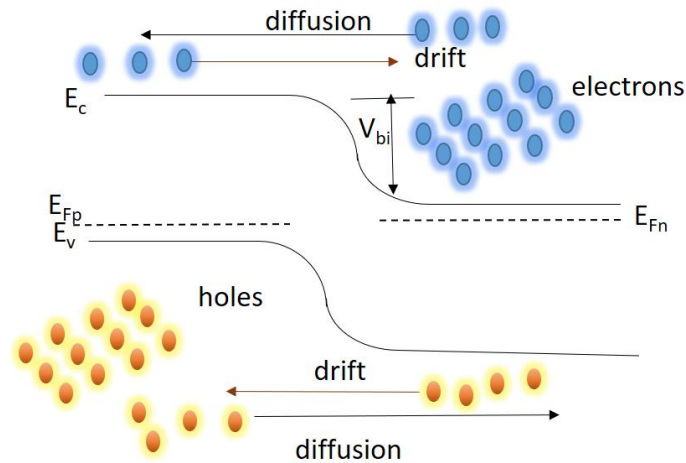


**Figure 2.2** Energy band diagram of a p – n junction under thermal-equilibrium.

When a voltage is applied to a solar cell, under dark condition, it behaves like an ideal p-n junction diode. Ideal diode equation is written as,

$$I = I_o \left( e^{qV/kT} - 1 \right), \quad (\text{Eq. 2.2})$$

In Eq. 2.2,  $I$  is the net current,  $I_o$  is the reverse saturation current,  $q$  is the electronic charge,  $k$  is the Boltzmann constant,  $V$  is the applied voltage,  $T$  is the ambient temperature.

When light shines on the solar cell, since more electrons are created due to the photo generation, ideal diode equation will be revised. Net current can be written as;

$$I = I_{\text{light}} - I_o \left( e^{qV/kT} - 1 \right), \quad (\text{Eq. 2.3})$$

where  $I_{\text{light}}$  represents the light generated current. Eq.2.3 can be extended as,

$$I = I_{\text{light}} - I_o \left( e^{q(V+I R_s)/nkT} - 1 \right) - \frac{V+I R_s}{R_{sh}}, \quad (\text{Eq. 2.4})$$

where  $R_s$  and  $R_{sh}$  parasitic resistances namely series and shunt resistance and  $n$  is the diode ideality factor which takes values between 1 and 2. Ideality factor determines how the solar cell is close an ideal diode. Series resistance is the resistance due to the contact resistance between base and emitter layers, metal and semiconductor, rear contact and the base material. On the contrary, shunt resistance is related to manufacturing defects. Low shunt resistance leads to decrease of collection of charge carriers [35]. In Figure 2.3, equivalent circuit model of a solar cell is shown.

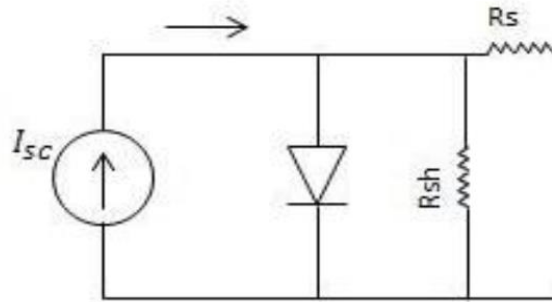


**Figure 2.3** Equivalent circuit model of solar cell [36].

Light generated current is related to generation rate. Generation rate is expressed as,

$$G = \alpha N_0 e^{-\alpha x}, \quad (\text{Eq. 2.5})$$

here  $\alpha$  is the absorption coefficient,  $N_0$  is the number of photons per unit area which is called photon flux,  $x$  is the penetration distance (cm) of the photon through the absorber layer. Thus, generation rate is highest at the surface of the absorber layer and decreases exponentially through the absorber layer.

Open circuit voltage ( $V_{oc}$ ) and short circuit current ( $I_{sc}$ ) values are two important solar cell parameters.  $I_{sc}$  is the maximum current at zero voltage.  $I_{sc}$  depends on the optical properties of solar cell, like absorption of the bulk layer and reflection.  $V_{oc}$  is the maximum voltage at zero current.  $V_{oc}$  can be derived from Eq.2.3. and expressed as;

$$V_{oc} = \frac{nkT}{q} \ln\left(\frac{I_{light}}{I_0} + 1\right). \quad (\text{Eq. 2.6})$$

Figure 2.4 shows I-V characteristic of a solar cell under dark and illuminated conditions. In dark, solar cell current voltage characteristic behaves like the I-V of an ideal diode. However, under illumination, due to the photo generation, I-V curve of an ideal diode shifts to the upper part of the y axis. In addition, inverse slope of I-V curve of the solar cell at zero voltage gives  $R_{SH}$  and at zero current gives  $R_s$  values.

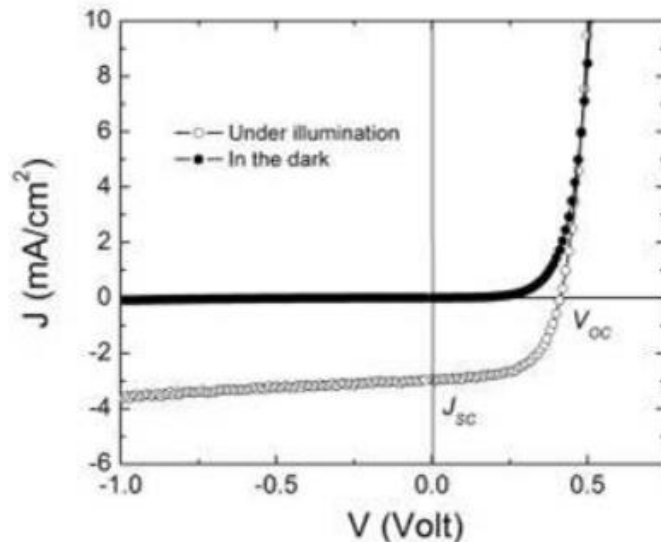


**Figure 2.4** I-V characteristic of solar cell in dark and under illumination [37] .

Fill factor and Conversion Efficiency are two other important parameters of a solar cell. Fill factor (FF) is the ratio of the product of maximum voltage ( $V_{mp}$ ) and maximum current ( $I_{mp}$ ) to the product of  $V_{oc}$  and  $I_{sc}$ . Mainly, Fill Factor is to be around 80% for the high efficiency solar cells [38]. Conversion Efficiency is defined as the ratio of energy output from the solar cell and input power.

$$\text{Fill Factor(FF)} = \frac{V_{mp} \cdot I_{mp}}{V_{oc} \cdot I_{sc}} . \quad (\text{Eq. 2.7})$$

$$\text{Efficiency}(\eta) = \frac{\text{FF} \cdot V_{oc} \cdot I_{sc}}{P_{in}} . \quad (\text{Eq. 2.8})$$

**Quantum Efficiency** is also one of the solar cell parameter defined as ratio of number of incident photons to collected photons. For an ideal solar cell, if all the incoming photons are collected, quantum efficiency must be equal to 1. External quantum efficiency (EQE) includes both reflection and transmission losses (Figure 2.5). However, Internal quantum efficiency(IQE) does not include transmitted and reflected photons. By extracting the transmission and reflection losses, EQE measurements can be corrected.

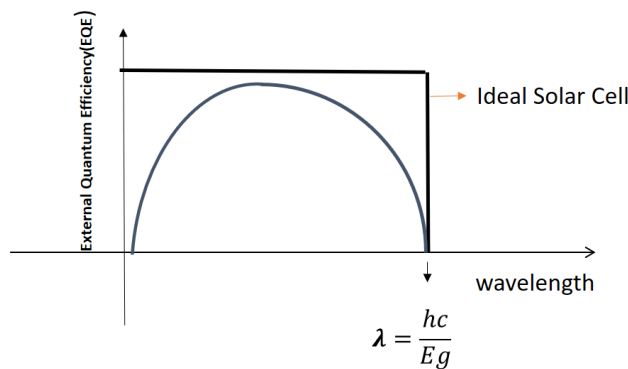


**Figure 2.5** External Quantum Efficiency graph.

## 2.2 Silicon Heterojunction (SHJ) Solar Cells

Unlike homojunctions, in SHJ solar cells, heterojunction forms between two dissimilar semiconductors. Due to the bandgap differences between different semiconductors such as c-Si and a-Si:H, band discontinuities occur at the valence and conduction band edges.

SHJ solar cell is composed of heterojunction between c-Si and doped a-Si:H layers. Cleaning process is applied as a formation of first step of SHJ solar cells. RCA (Radio Corporation of America) 1 and RCA2 cleaning procedure are performed to remove the organic and metallic impurities from the c-Si surface respectively. Second step is the texturing process in order to decrease the reflection losses. Surface of the c-Si wafer is textured by using KOH (Potassium Hydroxide) solution. After texturing process, intrinsic a-Si:H layer is deposited both rear and front side of the textured wafer to provide a good surface passivation. Thickness of the a-Si:H layer is very significant because at the front side, thicker a-Si:H layer increases parasitic absorption and at the rear side, thickness of a-Si:H layer is crucial to improve passivation quality [16]. Onto the n type c-Si wafer, p type a-Si:H layer is deposited to create front junction. On the rear side of the wafer n type a-Si:H layer is deposited to create back surface field (BSF). Deposited p type a-Si:H and n type a-Si:H layers are around 12 nm. Since the doped a-Si:H layers have low lateral mobility and conductivity, TCO layer is needed to increase lateral carrier transport through both front and rear junction. Finally, metallization is done for both front and rear junctions in order to collect the photo generated carriers. Figure 2.6 illustrates a typical SHJ solar cell formed by the above mentioned processes.

The key issue of SHJ solar cell is that i a-Si:H layer provides excellent surface passivation and due to the increase of surface passivation quality, minority carrier lifetime increases effectively. Main advantages of SHJ solar cell are listed below;

- low temperature process below 200 °C
- simple process flow compared to conventional Si solar cells

-usage of thin wafers

-possibility to change the properties of doped a-Si:H layer

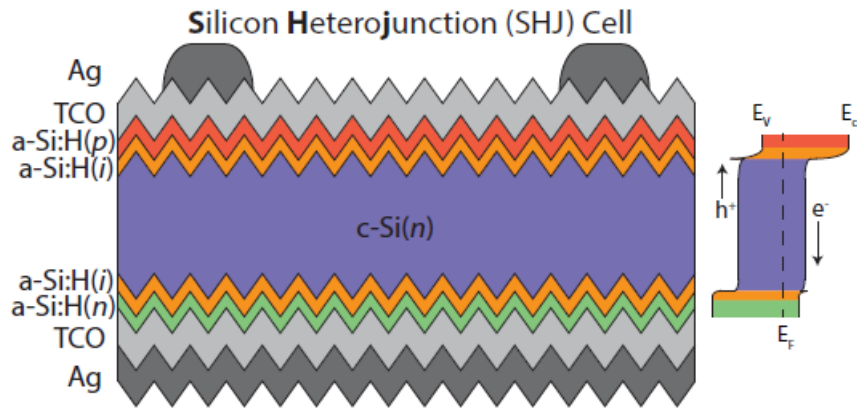


**Figure 2.6** Schematic diagram of a Silicon Heterojunction Solar Cells [39].

Since a-Si:H layers have wide bandgap compared to c-Si (a-Si:H 1.7 eV and c-Si 1.2 eV), band widening occurs at the junctions. This helps collection of the minority charge carriers both in front and rear junctions. On the front side of SHJ solar cells, in the conduction band, large band offset between p-i-n regions leads to formation of barrier for electrons and this allows electrons to flow through n type c-Si wafer. In the same manner, on the rear side of the cell, large band offset in the valance band results in formation of barrier for holes and holes can only travel through the front side (Figure 2.7). However, due to the large band offset, minority carrier at the front and rear side are trapped and they can only travel by tunneling.

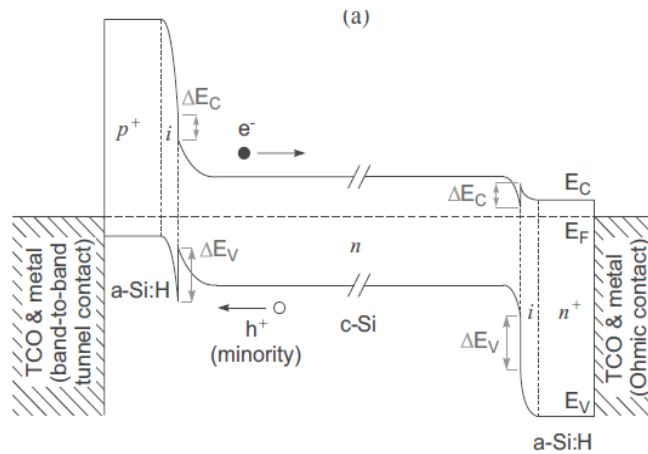


**Figure 2.7** Schematic band diagram of silicon heterojunction solar cell based on n type FZ c-Si wafer [40].

### 2.2.1 ITO and SHJ Solar Cells

Transparent Conducting Oxide which will be discussed in detail in the next section, is one of the layers which has an importance for the production of high efficiency SHJ solar cells. Due to its low resistivity and high transparency, ITO is utilized for anti-reflective front electrode for SHJ solar cells. In addition, ITO layer improves lateral transport between the fingers [41].

Main disadvantage of ITO layer is that, it leads to parasitic absorption especially in the blue range of the electromagnetic spectrum [33]. In order to reduce the parasitic absorption, it is important to decrease free carrier density of ITO layer.

Although the contact between n type a-Si:H and ITO layer is ohmic, Schottky contact forms between p type a-Si:H and ITO layer. For n based SHJ solar cells, front barrier height between p a-Si:H and ITO is one of the key parameters to achieve better cell performance. It is important to decrease Schottky barrier height between p a-Si:H and ITO layer in order to improve the carrier transport mechanism. To decrease the barrier height between ITO and p a-Si:H, the work function of ITO and deposition parameters of p a-Si:H thin film are very crucial. In Figure 2.8, the contact formation

between typical TCO and p a-Si:H layer is shown where  $E_a$  is the activation energy of p a-Si:H layer,  $\phi_{b0}$  is the front contact barrier height between p a-Si:H and TCO,  $\phi_m$  is the work function of TCO layer,  $\chi$  is the affinity of p a-Si:H layer,  $V_{bi}$  is the built in potential,  $E_{sbb}$  is the surface band bending,  $E_b$  is the surface potential barrier between TCO and p a-Si:H layer.

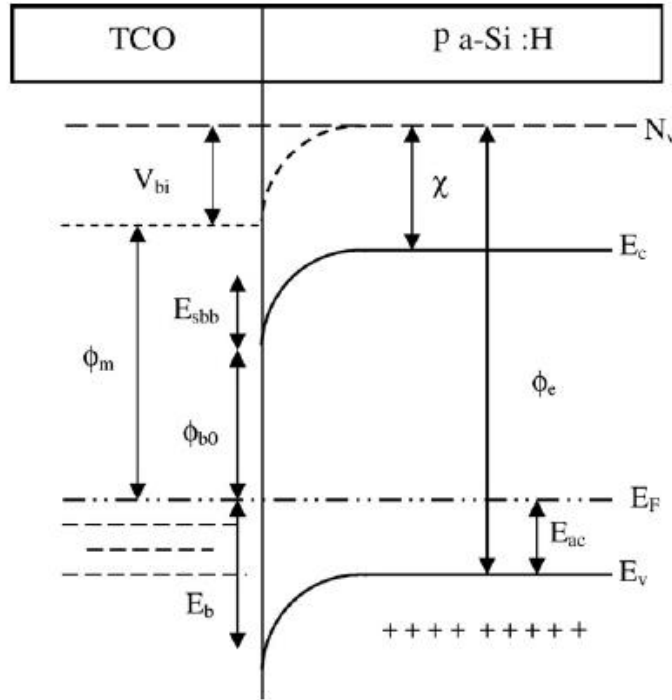


**Figure 2.8** Interface between ITO and p a-Si:H layer [42].

### 2.3 Transparent Conductive Oxides (TCO)

TCOs have high transmittance in the UV-Visible range in the spectrum. The transmission property of TCOs is due to the wide bandgap value of it. Since TCO has a wide bandgap which is greater than 3 eV, it makes TCO transparent, in the visible range of the spectrum. Highly conductive and transparent properties make TCOs

excellent anti-reflective front electrode materials. Conduction mechanism of TCO can be explained by the defects in the structure.

There are some drawbacks for TCO materials. In the short wavelength region, transmittance of TCO is very low due to high absorption of photons with higher energy than the bandgap. This absorption type called parasitic absorption. In the long wavelength region, incoming photon energy is lower than the bandgap and as a result transmittance is low. Near infrared region (NIR), transmittance dramatically decreases, this leads to increase of free carrier absorption. Free carrier absorption can be explained by Drude Theory [43]. In Drude Theory, frequency dependent electric permittivity is written as;

$$\epsilon(\omega) = (n(\omega) - ik(\omega))^2 \quad (\text{Eq.2.9})$$

$$1 + \chi(\omega) = 1 - \frac{\omega_p^2}{\omega^2 + \frac{i}{\omega't}}$$

where  $\chi(\omega)$  is the dielectric susceptibility,  $n-ik$  is the complex refractive index and  $\omega_p$  is the plasma frequency and it is expressed as;

$$\omega_p = \frac{ne^2}{\epsilon_0 m_e^*} , \quad (\text{Eq.2.10})$$

where,  $n$  is the charge carrier concentration,  $e$  is the elementary charge,  $m_e^*$  effective mass of an electron,  $\epsilon_0$  is the permittivity of free space. By neglecting imaginary part of the dielectric susceptibility and making an approximation,  $\omega t \gg 1$ ,  $\epsilon$  is written as;

$$\epsilon \sim 1 - \frac{\omega_p^2}{\omega^2} . \quad (\text{Eq.2.11})$$

If  $\omega > \omega_p$  the material will be transparent; however, when  $\omega < \omega_p$ , refractive index will be imaginary which leads to increase in reflectivity of the material. If the approximation,  $\omega t \gg 1$ , is not valid, imaginary part of  $\chi$  should be taken into consideration. Decreasing plasma frequency causes the increase of imaginary part of the  $\chi$ . In other words, increasing plasma wavelength ( $\lambda_p$ ) leads to increase in absorption. If the wavelength is longer than plasma wavelength, reflectivity of the material increases which can be seen in Figure 2.9. For solar cell applications, TCOs should be transparent in the active region. However, plasma frequency is related to free carrier density ( $n$ ). Thus, it is important to find the balance between plasma frequency and free carrier density to decrease the free carrier absorption.

Moreover, in the visible range of the spectrum, interference fringes can be observed which are related to film thickness. Absorption, transmission and reflection spectra of ZnO as a representative of TCO materials, is illustrated in Figure 2.9 [33].

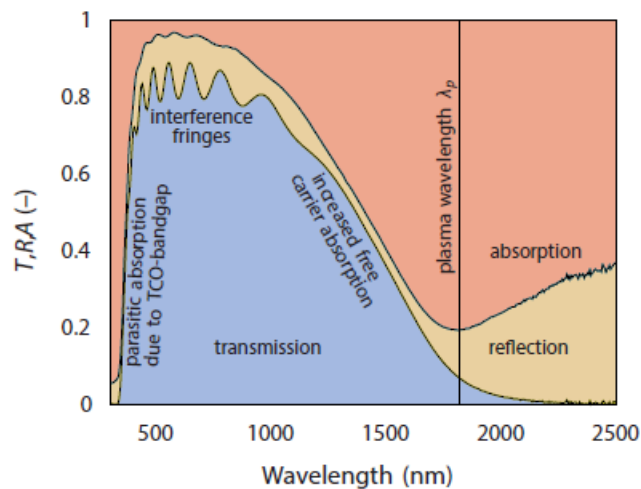


**Figure 2.9** Transmission, Reflection and Absorption spectrum of ZnO, adapted from [33].

### 2.3.1 Mobility and Scattering Mechanisms of TCO

Mobility is an important parameter for TCOs. Mobility values of TCO materials are related to the scattering mechanism. There are three main scattering mechanisms

limiting to mobility; which are ionized impurity, neutral and grain boundary scatterings. The mobility expression for n-type conduction is given as;

$$\mu = \frac{q \cdot \tau}{m^*} = \frac{q \cdot l}{m^* V_e}, \quad (\text{Eq. 2.12})$$

where  $q$  is the electron charge  $m^*$  is the effective mass of electrons,  $\tau$  is the relaxation time between two successive collisions,  $V_e$  is the electron velocity,  $l$  is the mean free path of electrons. Although there are some p type TCOs, most frequently used TCOs are n type semiconductors. For that reason, only electrons are considered as the charge carrier.

**Ionized impurity scattering** is mainly caused by the activation of dopant impurity atoms. This mechanism starts to be more dominant when the carrier concentration is greater than a minimum value,  $N_D > 10^{19} \text{cm}^{-3}$ . Zawadzki [44] was first formulized this scattering parameter which was then improved by Pisarkiewicz [45]. In this expression, non-parabolicity of conduction band has taken into account. In Eq. 2.13, the mobility expression for ionized impurity scattering is given by;

$$\mu_i = \frac{3(\epsilon_r \epsilon_0)^2 h^3 N}{Z^2 m^{*2} q^3 N_i} \frac{1}{\delta_d F_i^{np}}, \quad (\text{Eq. 2.13})$$

Where  $\epsilon_r$  is the relative permittivity of dielectric material,  $\epsilon_0$  is the permittivity of the free space,  $Z$  is the total charge of dopant atoms,  $N_i$  is the concentration of ionized impurities,  $F_i$  is the screening function and it depends on the  $\delta_d$  value which is related to degeneracy of semiconductor.

**Grain boundary scattering** is also one of the possible scattering mechanism in TCOs. If TCO's composed of polycrystalline structure, grain boundary scattering can be dominant scattering mechanism. It is the only temperature dependent scattering mechanism. Depending on the grain size, defect states and vacancies in the crystal structure grain boundaries can have an active role during the scattering of the charge carriers. There are two possible ways when electrons are crossing the grain boundaries which are tunneling and thermionic emission. Seto [46] was

developed a model for the grain boundary scattering on polycrystalline silicon. According to his theory, mobility is expressed as,

$$\mu_{gb} = \frac{qL}{\sqrt{2\pi m^* kT}} e^{-\left(\frac{E_b}{kT}\right)}, \quad (\text{Eq. 2.14})$$

where  $q$  is the electron charge,  $L$  is the grain size,  $k$  is the Boltzmann constant,  $T$  is the temperature,  $m^*$  is the effective mass of electron,  $E_b$  is the potential barrier height due to the charge accumulation at the grain boundaries.

**Neutral impurity scattering** is also another dominant scattering mechanism for TCOs. It was first discovered by Cavid Erginsoy [47]. He observed the scattering between electrons and hydrogen atoms and he adjusted his theory to semiconductor basis. Low deposition temperature such as room temperature for the TCO deposition, results in inactive dopant atoms and this leads to neutral impurity scattering [48]. Mobility equation for neutral impurities improved by Erginsoy is given as;

$$\mu_{ni} = \frac{m^* q^3 h^3}{20 \epsilon_r \epsilon_0 N_n \hbar^3}, \quad (\text{Eq. 2.15})$$

where  $N_n$  is the concentration of neutral impurities and the other parameters are the same as in the above equations.

### 2.3.2 Indium Tin Oxide (ITO)

Indium Tin Oxide which is tin doped indium oxide, is composed of indium oxide ( $\text{In}_2\text{O}_3$ ) and Sn. It has cubic bixbyite structure since  $\text{In}_2\text{O}_3$  has this crystal structure and it is more dominant than Sn concentration when ITO structure is not heavily doped. Cubic bixbyite structure is also called C type rare-earth oxide structure with space group  $T_H^7 \text{ Ia}3$  [49]. It exhibits fluorite-related structure in which one oxygen atom is missing in one of the  $\langle 111 \rangle$  direction. In other words, there are some oxygen vacancies in the (111) plane. Indium atoms can be positioned either b sites or d sites. In b sites, the structure has body diagonal oxygen vacancies; however, in d sites, the structure has face diagonal oxygen vacancies. In this crystal structure, there are 80

atoms in one-unit cell [50]. There are 8 atoms in b sites, while there are 24 atoms in d sites per unit cell. Figure 2.10 shows cubic bixbyite structure of  $\text{In}_2\text{O}_3$ .

Since It has high direct bandgap range approximately between 3-4 eV, it has high transmittance in the visible range. However, Klein pointed out that ITO bandgap can be indirect with a value of around 2.8 eV [51]. Understanding of conducting behavior of TCO material is complex but basically oxygen vacancies and impurity atoms (Sn) make ITO conductive. Conductivity mechanism of ITO is related to scattering mechanism of free carriers [52]. Since ITO is heavily doped n type degenerate semiconductor, Fermi level can lie above the conduction band. This phenomenon is explained by Burstein-Moss Shift [53]. Increment of the carrier concentration leads to blue shifting of edge [54]. Mobility and the carrier density values of ITO vary between 20 and 40  $\text{cm}^2/\text{V}\cdot\text{s}$  and of  $10^{19}$ - $10^{21}$   $\text{cm}^{-3}$  respectively [55]. Work function of ITO can vary with the deposition method and deposition conditions. ITO work function can be tunable between 4.0-4.9 eV depending on the deposition condition, especially oxygen partial pressure, during the deposition process [56].

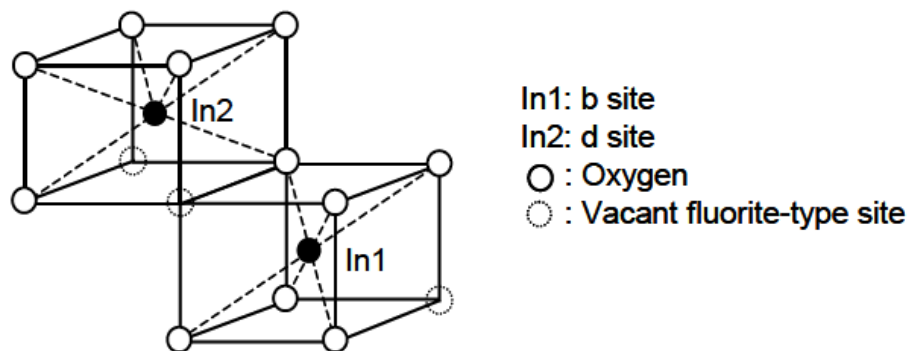


**Figure 2.10** The cubic bixbyite structure of  $\text{In}_2\text{O}_3$  [57].

## 2.4 Contact Resistivity Analysis

Besides the optimization studies of ITO, in order to characterize the specific contact resistivity values of ITO and different layers in SHJ solar cells, different methods were applied in the scope of the thesis. In this part of the chapter, background information about contacts and contact resistivity, metal semiconductor contact formation and measurements of contact resistivity techniques will be given.

### 2.4.1 Metal Semiconductor Contacts

There are two types of metal-semiconductor contacts which are Schottky and ohmic contacts. Contact differences related to potential barrier height are created at the surface. According to Schottky Mott theory [58], when the metal and semiconductor are brought together, fermi levels align until they reach up the equilibrium and due to the their work function differences, potential difference forms at the interface and this leads to band bending in the energy band diagram which is called potential barrier.

Depending on the doping concentration of the semiconductor, carrier transport mechanism can vary. According to thermionic emission theory, when barrier height is much bigger than  $kT$  value, this allows carriers to follow the thermionic emission process. For lowly doped n type semiconductors such as  $N_D$  (donor concentration)  $\leq 10^{17} \text{ cm}^{-3}$ , thermionic emission process is dominant for the carrier transport. In this process, carriers are transferred by thermal excitation. In n type semiconductor, when  $N_D$  is between  $10^{17}$  and  $10^{19} \text{ cm}^{-3}$  thermionic-field emission will be dominant. In this case, thermal excitation of carriers occurs where the barrier is narrow for tunneling process. For  $N_D > 10^{19} \text{ cm}^{-3}$  field emission transport is dominant and more linear I-V characteristic is observed. In field emission, instead of first two process, carrier transport is dominated only by tunneling since the barrier is sufficiently narrow for tunneling process (Figure 2.11).

One can say that the thermionic emission theory is more dominant for the Schottky contacts as the current transport mechanism of metal-semiconductor junction is related to majority carrier in the junction [59].

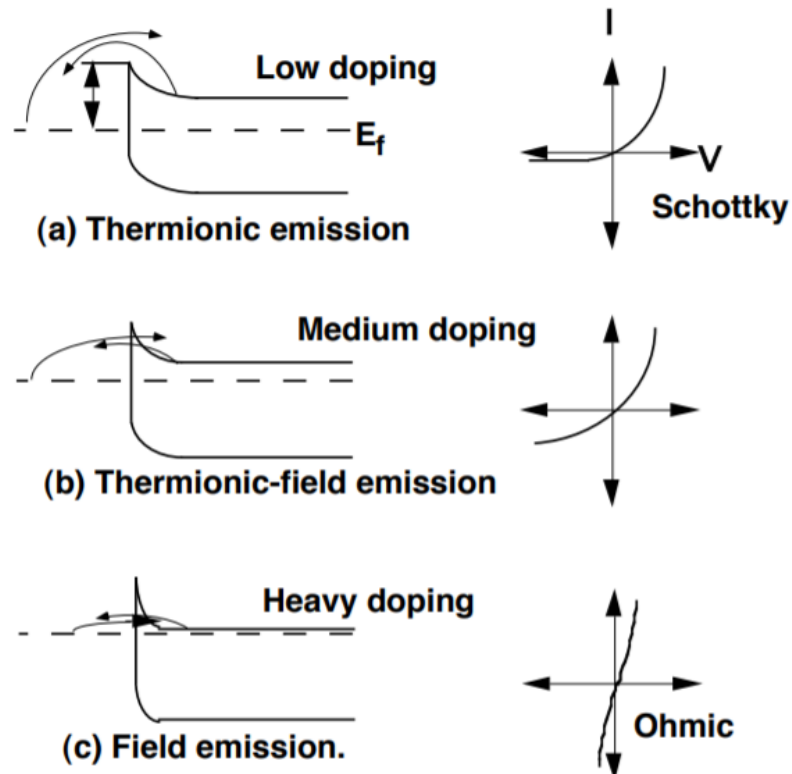


**Figure 2.11** Conduction mechanism of metal – semiconductor (n type) interaction depending on the doping concentration [60].

#### 2.4.1.1 Ohmic Contacts

In the ideal metal semiconductor contacts, the contacts must be ohmic. When metal semiconductor contacts are ohmic, it shows linear I-V characteristics in both reverse and forward bias. In ohmic contact formation, majority carriers easily flow in both directions since barrier height between metal and semiconductor is small compared to rectifying contacts. For n type semiconductor, if work function of the metal ( $\phi_M$ ) is smaller than the work function of semiconductor ( $\phi_S$ ), barrier between metal and semiconductor is small and electron flow is easily supplied between the metal and semiconductors. No depletion region occurs at the interface of metal and

semiconductor. Similar contact formation is obtained for p type material when  $\phi_M > \phi_S$ . Holes flow easily across the metal semiconductor interface. Figure 2.12 shows ohmic contact formation for p and n type semiconductors where  $\chi$  is the electron affinity of semiconductors,  $\phi_M$  and  $\phi_S$  metal and semiconductor work functions respectively,  $E_{Fs}$  and  $E_{Fm}$  are fermi levels of semiconductor and metal.

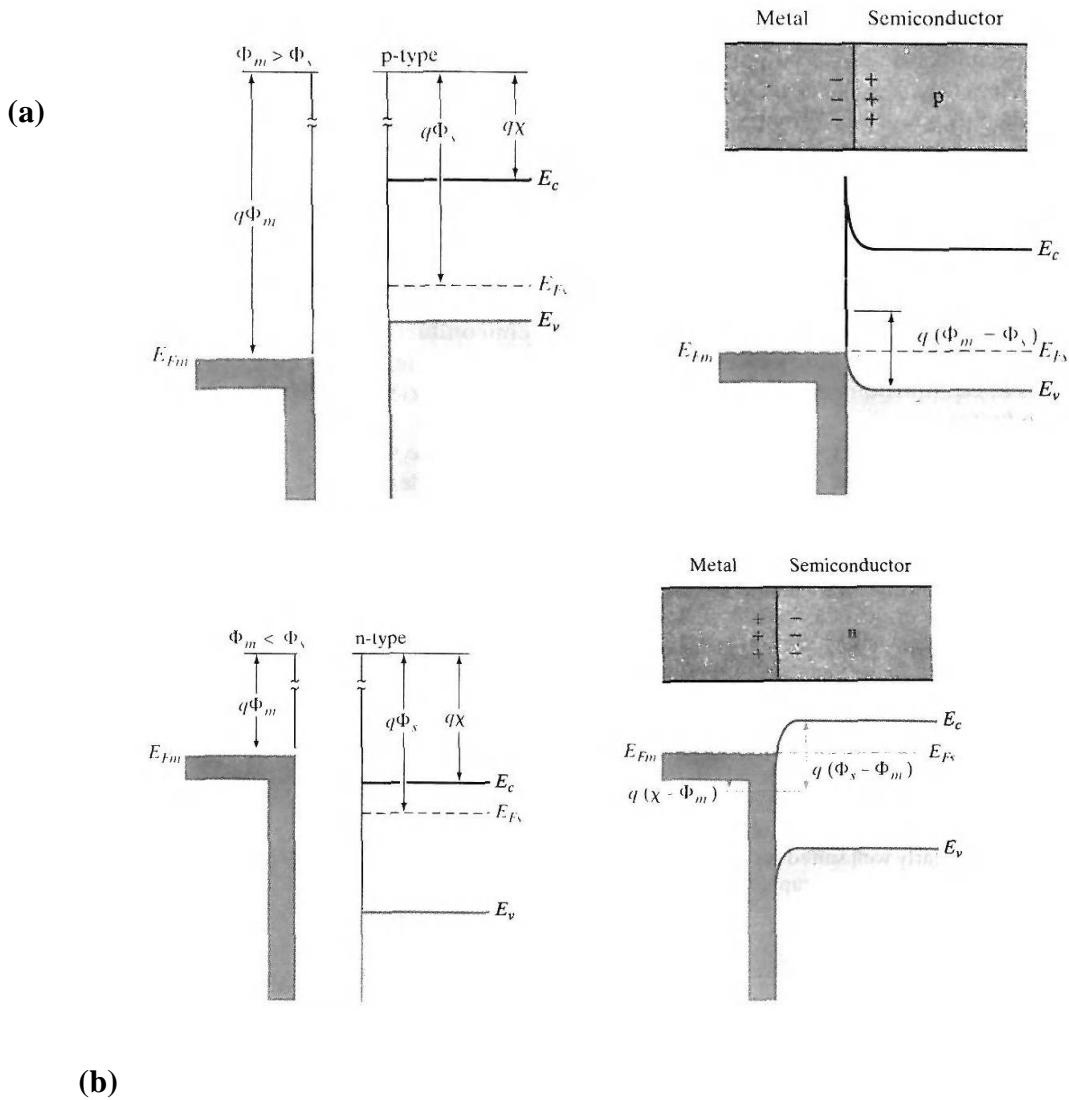
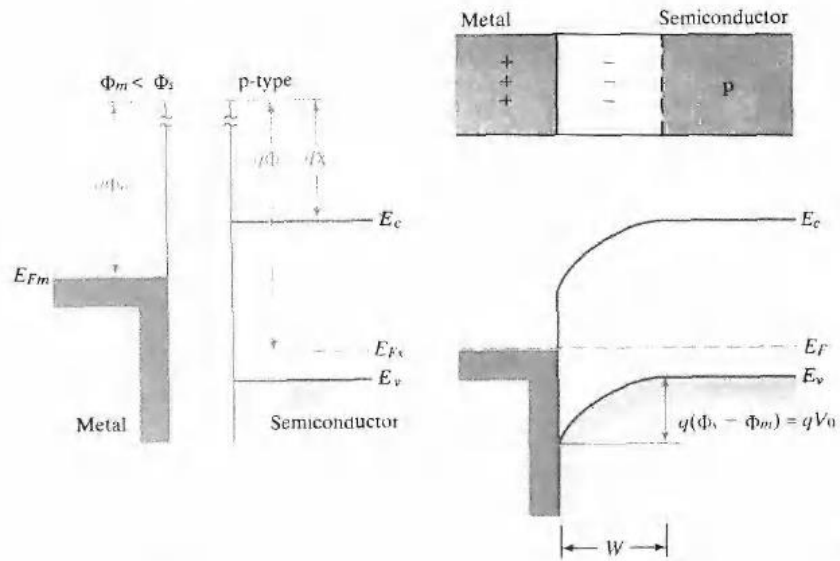


**Figure 2.12.** Ohmic contact formation for n and p type semiconductors, (a) p type semiconductor, (b) n type semiconductor [61].

### 2.4.1.2 Schottky Contacts

Unlike ohmic contacts, Schottky contacts are rectifying contacts which show non-linear I-V characteristics. For n type semiconductor, if  $\phi_M$  is greater than  $\phi_S$ , electrons in the semiconductor have lower potential energy than the metal side and barrier forms at the interface of metal and semiconductor. Electrons in the conduction band, need to cross the barrier to participate in conduction mechanism. For p type semiconductor, same situation occurs when  $\phi_M > \phi_S$ . Schottky contact formation of p and n type materials are illustrated in Figure 2.13. Metal Semiconductor Schottky contacts behave like a p-n junction diode and depletion region occurs at the metal-semiconductor interface and depletion width  $W$  is shown in the Figure 2.13.

(a)





dimensional current flow analysis were done by Kennedy and Murley assuming that the contact resistance is to be zero [64]. Their study revealed that the current crowding occurs at the contacts. They realized that only some part of the contacts has an active role on the current transfer. This resulted in improving transfer length concept. TLM theory was first experienced by Murmann and Widman assuming the existence of both sheet and contact resistance [65]. In 1972, TLM theory was improved by Berger [66] and according to his theory, apart from the Kennedy and Murley, contact resistance is not assumed to be zero but semiconductor sheet thickness is assumed to be zero and this assumption allows the current flows only one direction. Berger extended his TLM theory and in this case sheet thickness is not zero but current flow is still only one direction. According to his theory, contact resistance can be written in terms of the sheet resistance ( $R_{sh}$ ) and  $\rho_c$  which are the two encountered resistances when current flow metal to semiconductor or vice versa. According Berger's TLM theory, potential distribution and contact resistance ( $R_c$ ) can be written as;

$$V(x) = \frac{I\sqrt{R_{sh}\rho_c}}{W} \frac{\cosh(\frac{L-x}{L_T})}{\sinh(L/L_T)}. \quad (\text{Eq. 2.16})$$

When  $x=0$ , contact resistance can be extracted as Eq.2.16

$$R_c = \frac{\sqrt{R_{sh}\rho_c}}{W} \coth(L \sqrt{\frac{R_{sh}}{\rho_c}}), \quad (\text{Eq. 2.17})$$

where  $W$  is the contact width,  $L_T$  is the transfer length,  $L$  is the contact length,  $I$  is the current flow through the contact. When  $x = 0$ , highest voltage value is obtained and voltage drop is observed proportional to  $1/e$ . Due to this potential drop, only part of the contact can get involved to current transfer. This active part of the contact is called transfer length  $L_T$  and it can be expressed as;

$$L_T = \sqrt{\frac{\rho_c}{R_{sh}}}. \quad (\text{Eq. 2.18})$$

Transfer length can be considered as effective distance in which the most of the current is transferred from metal to semiconductor or vice versa. In Figure 2.14.a current flow path and transfer length are illustrated.  $L_T$  should not be wider than the contact length in order to make correct evaluation about specific contact resistivity [67].

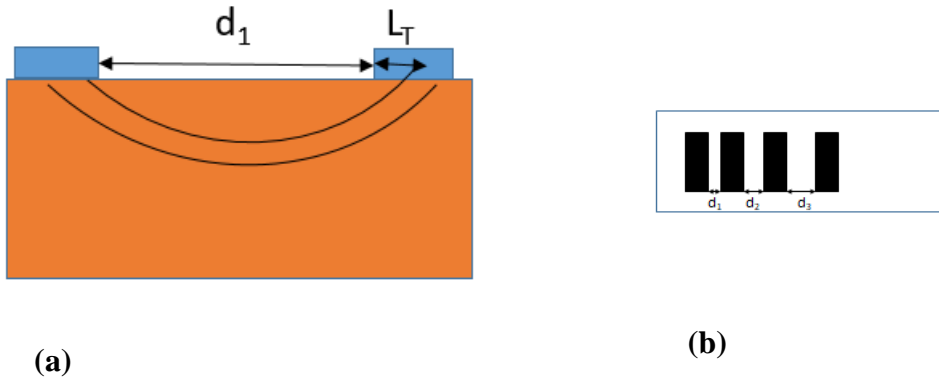


**Figure 2.14.** (a) Current flow path between the two contacts (b) rectangular TLM pattern.

By applying Ohm's law and applying linear fit to the graph of total resistance vs. contact separation,  $R_{sh}$ ,  $L_T$  and  $\rho_c$  values can be extracted. As can be seen in Figure 2.15, slope of the linear fit gives  $R_{sh}/W$  value, intercept of the negative x axis corresponding to  $2L_T$  and intercept of the y axis corresponding to  $2R_c$ . By using  $R_c$ ,  $L_T$  and  $W$  values, specific contact resistivity can be extracted. Eq. 2.19 is a mathematical expression of contact resistivity.

$$\rho_c = R_c L_T W \quad (\text{Eq.2.19})$$

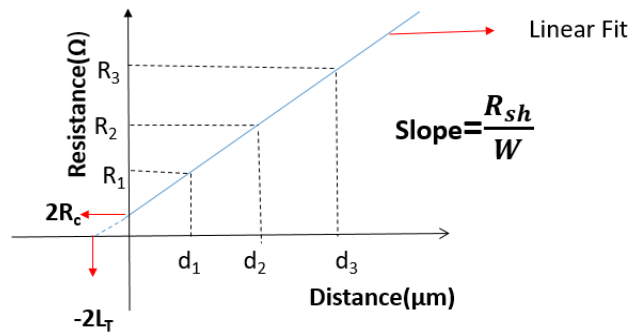


**Figure 2.15.** Plot of total resistance as a function of contact spacing where  $d_1$  and  $d_2$ ,  $d_3$  show different contact spacing.

When TLM is applied to calculate specific contact resistivity, many assumptions were undertaken. For example, resistance of the metal contact is neglected. Although metal contacts have negligible resistance values, it leads to little error on the contact resistivity values. In addition, extraction of contact resistivity from TLM theory is based on constant electrical and contact parameters. However, these parameters can lose their invariability even if experimentally no error is observed [67].



## CHAPTER 3

### EXPERIMENTAL PROCEDURE AND CHARACTERIZATION TECHNIQUES

#### 3.1 Introduction

In this chapter, the sample preparation and deposition procedure of ITO thin films and characterization techniques used in this study will be given. ITO thin films were deposited onto borosilicate glass substrates and n type FZ and CZ wafers via magnetron sputtering. Then, they were characterized by using different characterization techniques such as the Four Point Probe, Atomic Force Microscopy, X ray Diffraction, Hall Effect, Spectroscopic Ellipsometry and Spectrophotometry.

To deposit the samples which are used in contact resistivity analysis, PECVD (Plasma Enhanced Chemical Vapor Deposition) cluster, sputtering and thermal evaporation systems were used. Firstly, intrinsic and doped a-Si:H layers were deposited onto n type FZ and CZ wafers via PECVD. Secondly, ITO layer was deposited onto the a-Si:H layers by using magnetron sputtering. Finally, metallization was performed by using thermal evaporation method. During the sputtering and metal evaporation, shadow masks were used to determine the contact resistance of the desired layers. Then, different I-V measurements were performed in order to determine specific contact resistivity between the different layers in the SHJ structure.

#### 3.2 Sample Preparation and Cleaning Procedures

Before each deposition, substrates were cleaned by RCA-2 (Radio Corporation of America) and Piranha solutions. Glass substrate are cleaned by acetone–alcohol and Piranha solution while n type wafers were cleaned by using Piranha and RCA- 2 solutions. These cleaning procedures are explained below;

### **RCA-2 Cleaning**

RCA-2 cleaning is based on the removal of metallic impurities from the Si surface. Chemical solution is prepared by using hydrogen peroxide ( $\text{H}_2\text{O}_2$ ), hydrochloric acid (HCl) and deionized water. The solution temperature is around 70 °C. It oxidized the surface of the Si (oxide layer is less than 2nm) and this thin oxide layer is removed by HF dipping before each deposition.

### **Piranha Cleaning**

Piranha solution is one of the most robust chemical solution which is used to remove the organic impurities from the Si surface. It is consisted of a mixture of sulfuric acid ( $\text{H}_2\text{SO}_4$ ) and hydrogen peroxide ( $\text{H}_2\text{O}_2$ ). Piranha solution is an exothermic reaction and solution temperature can rise to 100-130 °C. In this study, Piranha solution was used for the organic residues from Si surface and borosilicate glass substrate [68].

### **Ultrasonic Acetone –Alcohol Cleaning**

Ultrasonic acetone–alcohol solution was used to clean borosilicate–float glass substrates. Cleaning procedures were performed in two steps. Glass substrates were first cleaned by acetone solution for 15 minutes in ultrasonic bath and rinsed by deionized water. As the second step, glass substrates were cleaned by ultrasonic alcohol solution for 15 minutes and then rinsed by deionized water.

### **3.3 Deposition of doped a-Si:H layers by using PECVD**

Deposition of a-Si:H layers were performed by (PECVD). It is one of the chemical vapor deposition techniques which is mainly used to deposit the doped and intrinsic a-Si:H layers from the gas phase to the solid phase. Low deposition temperature is one of the main advantage of the PECVD process. Plasma consists of free radicals, electrons, ions, molecules, neutral atoms and other species. When these molecules and atoms are interacting with the surface of the substrate, reaction product is deposited as a thin film.

After each deposition, both walls of the chamber and cathode are covered by previous deposition radicals. If no cleaning procedure were applied, after a couple of deposition runs, radicals drop to the chamber as a powder. This powder source causes the contamination of chambers and chamber walls. Plasma etching process were applied in order to prevent chamber contamination.  $C_2H_6/O_2$  mixture or  $NF_3$  gases were used during the plasma cleaning. In addition, He gas is used during the plasma etching to decrease plasma etch rate. Since He is a noble gas, it does not get involved in any reaction with free radicals.

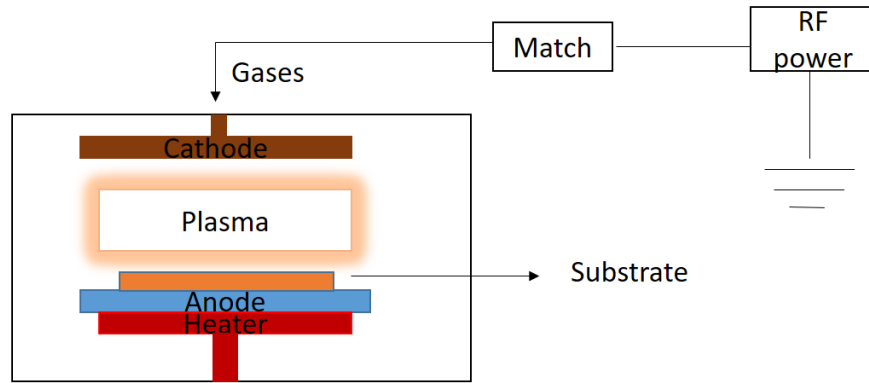


**Figure 3.1.** Schematic representation of PECVD chamber.

PECVD system in GÜNAM (GünEr System) was developed by Vaksis (Vakum Systems) which is designed for the deposition of a:Si layers, SHJ solar cells, nano and micro-crystalline Si. It is composed of Inductively Coupled Plasma (ICP) and three Capacitively Coupled Plasma (CCP), sputter, transfer and Load Lock chambers. Except from Load Lock chamber, other chambers are kept under vacuum in order to prevent contamination. CCP is one of the industrial plasma source which is mainly consisted of two separate electrodes. As presented in Figure 3.1, one of them is connected to the RF source (cathode), other (anode) is grounded. In GünEr system, there are three separate CCP chambers and each of them is responsible for

the deposition of different doped a-Si:H and i a-Si:H layers. As shown in Figure 3.2, each CCP chamber is connected to the transfer chamber. The use of separate chambers prevents contamination of the chambers. To deposit the doped p and n type a Si:H layers, besides SiH<sub>4</sub> and H<sub>2</sub> gases, B<sub>2</sub>H<sub>6</sub> and PH<sub>3</sub> gases were introduced to the different CCP chambers respectively. RF Power source used in CCP chambers is equal to 13.56 MHz with a maximum power output of 600W.

Deposition parameters such as substrate temperature, gas ratios, and deposition time of doped and intrinsic a Si:H layers, which are used for the contact resistivity analysis and the fabrication of SHJ solar cells are given Table 3.1. For all a-Si:H depositions, RF power was equal to 30 Watt. Deposition pressure of n and p type a-Si:H layers was equal to 1mTorr, while the deposition pressure of intrinsic a Si:H layer is 1.2 mTorr.

**Table 3.1** Deposition parameters of a Si: H layers by PECVD.

<b>Sample Code</b>	<b>SiH<sub>4</sub></b> (sccm)	<b>H<sub>2</sub></b> (sccm)	<b>PH<sub>3</sub></b> (sccm)	<b>B<sub>2</sub>H<sub>6</sub></b> (sccm)	<b>Substrate Temperature</b> (°C)	<b>Deposition Time</b> (seconds)
i a-Si:H(TLM)	40	120	-	-	200	20
i aSi:H(SHJcell)	40	120	-	-	200	25
p a-Si:H(TLM)	13	190		34	175	180
n a-Si:H (TLM)	13	125	25	-	200	90
p a-Si:H(TLM)		190		34	175	45
n a-Si:H (TLM)	13	125	25	-	200	45
n a-Si:H(SHJ cell)	13	125	25	-	200	57
p a-Si:H(SHJ cell)	13	190	-	34	175	100

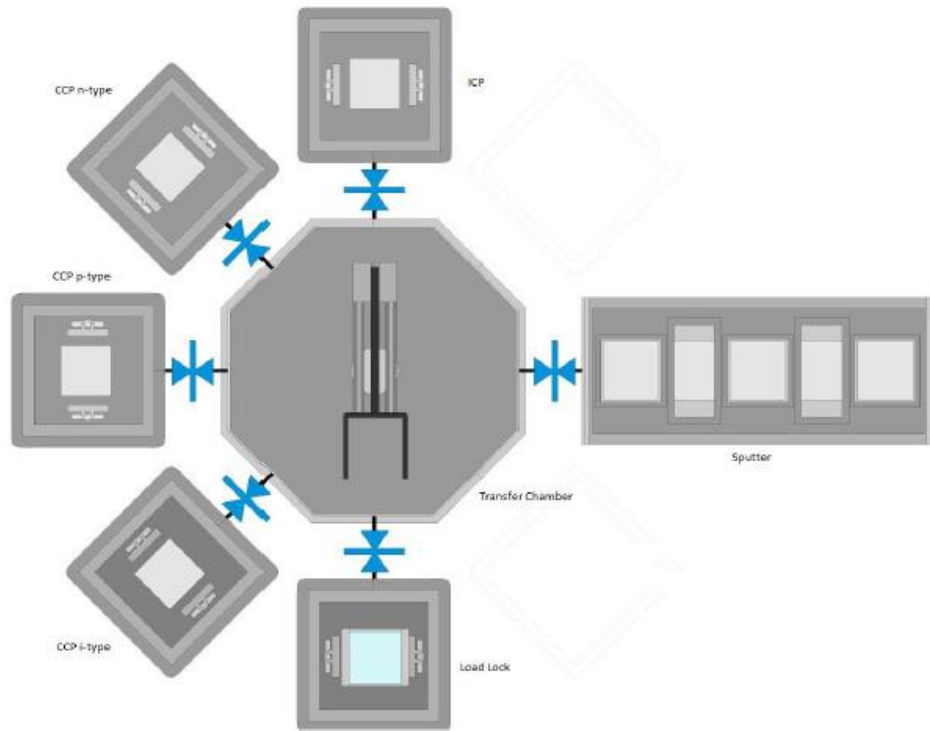


**Figure 3.2** Schematic configuration of GÜNER System [69].

### 3.4 Deposition of ITO Thin Films by Sputtering

Sputtering is one of the most common physical vapor deposition techniques. In this technique, no surface reaction occurs during the film deposition which leads to uniform film deposition, controllable film thickness and surface adhesion. DC (Direct Current) and RF sources are used for plasma excitation. DC sputtering is only for conductive targets while RF sputtering is used for both conductive and non-conductive targets. In the sputtering technique, atoms are ejected from a target to the substrate by high energetic ion bombardment. Due to the ion bombardment, secondary electrons are emitted from the target. It is important to increase the density

of secondary electrons to maintain plasma discharge. In RF magnetron sputtering, the magnetic field is created parallel to the target surface which increases the plasma density by increasing density of secondary electrons (Figure 3.3).

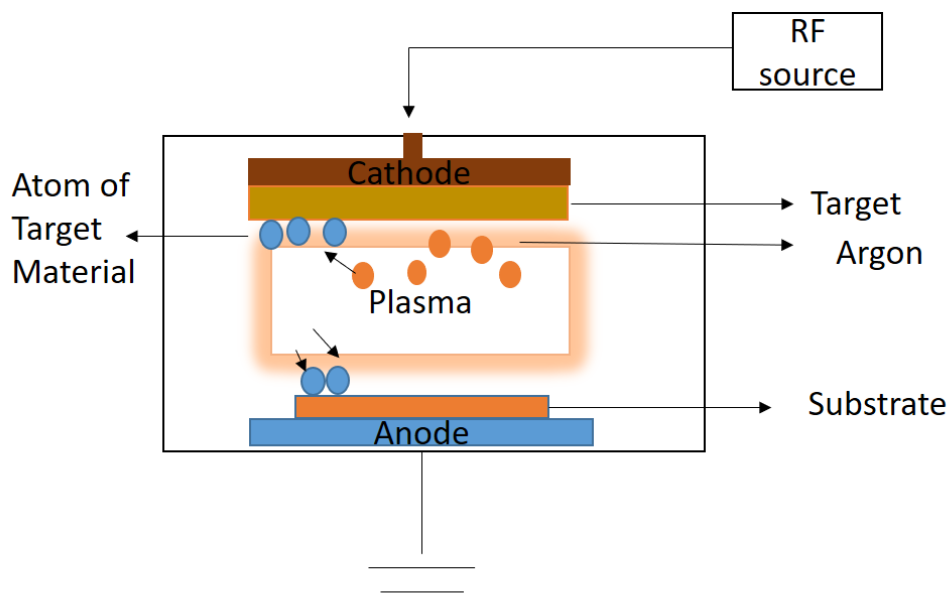


**Figure 3.3** Representation of sputtering process.

The sputter target used consists of indium tin oxides ( $\text{In}_2\text{O}_3:\text{SnO}_2 = 90:10$  wt. %) with a purity of 99.9 %. The system was evacuated to a base pressure of  $2 \times 10^{-6}$  Torr by using mechanical and turbo molecular pump and sputter chamber was presputtered for 10 minutes before each deposition. The RF source was used at 13.6 MHz and 5kW. Another robot arm is placed into sputter chamber which helps holder to lateral movement between the heaters.

In this study, RF Magnetron sputtering was used to deposit ITO layers. The deposition of ITO layers for contact resistivity studies was carried out through a shadow mask. In addition to  $\text{Ar}^+$ , oxygen is added to inert gas mixture in order to investigate the change of ITO film properties with the oxygen content. Oxygen

partial pressure has a significant effect on the ITO film properties such as conductivity and mobility.

As shown in Figure 3.4, sputtering chamber is consisted of two ceramic targets and three heaters. First target is the AZO target which is located between heater 1 and heater 2, while second one is ITO target which is located between heater 2 and heater 3. Apart from PECVD chambers, in sputter chamber, heating process is carried out from above which enables to decrease heating process of the substrate.

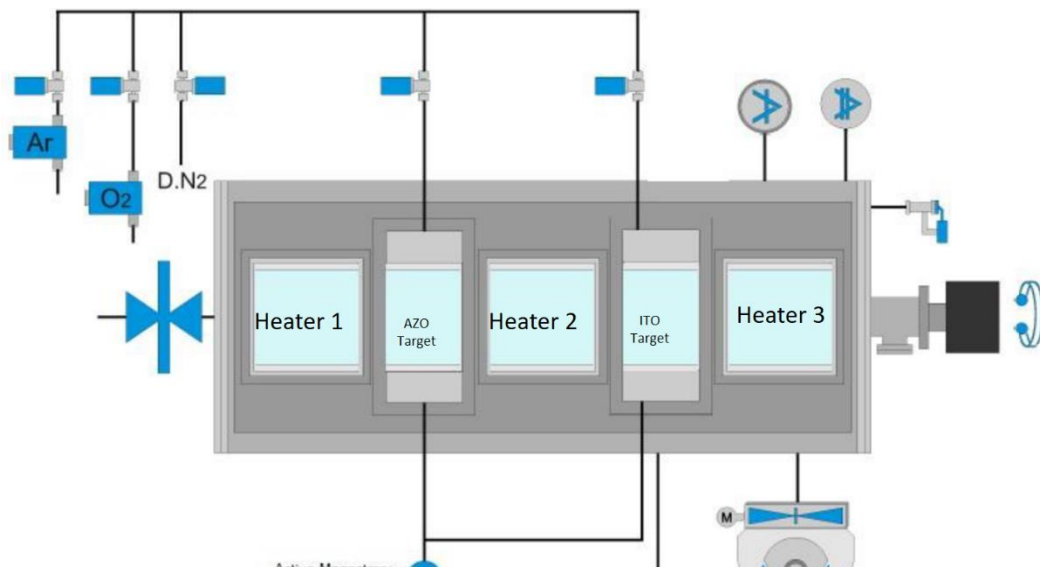


**Figure 3.4** Schematic configuration of RF magnetron sputtering system.

In Table 3.2, 3.3 and 3.4 different deposition parameters of ITO thin films with their thicknesses are given.

In Table 3.2, deposition pressure, Ar flow rate and robot arm speed were kept constant which are equal to 3 mTorr, 125 sccm and 20 cm/min, respectively. However, substrate temperature, deposition time and RF power were variable parameters. In Table 3.2, variable deposition parameters and film thicknesses are given for the ITO films of the first six deposition runs.

**Table 3.2** Deposition Parameters of ITO Thin Films with different power and substrate temperatures.

<b>Deposition Parameters</b>	<b>ITO1</b> 96 nm	<b>ITO2</b> 93 nm	<b>ITO3</b> 180 nm	<b>ITO4</b> 230 nm	<b>ITO5</b> 80 nm	<b>ITO6</b> 100 nm
SubstrateTemperature	100 °C	100 °C	100 °C	200 °C	200 °C	200 °C
Sputtering Power	400 W	300 W	200 W	400 W	300 W	200 W
Deposition time	25 min	25 min	25 min	35 min	35 min	35 min

After the determination of the optimum deposition parameters of ITO films grown without oxygen, in order to examine oxygen content on ITO thin film properties, ITO thin films were deposited by changing the Oxygen/Ar ratio. Oxygen was added to gas mixture and the ratio of Oxygen gas to total gas flow ( $O_2/(O_2+Argon)$  flow) is called  $O_2/Ar$  ratio. Other parameters are kept constant. Substrate temperature was 200 °C, deposition pressure was equal to 3 mTorr, and RF power was equal to 400 Watt. Moreover, robot arm speed and deposition time were also kept constant which were equal to 20 cm/min and 20 min. In Table 3.3, thicknesses and deposition parameters of ITO films with different  $O_2/Ar$  ratios are given.

**Table 3.3** Deposition parameters of ITO thin films with different Ar/oxygen ratio.

<b>Deposition Parameters</b>	<b>ITO10</b> 79 nm	<b>ITO11</b> 88 nm	<b>ITO12</b> 138 nm	<b>ITO13</b> 148 nm	<b>ITO17</b> 158 nm	<b>ITO23</b> 155 nm
$O_2 /Ar$ % ratio	5%	3%	%1	%0.8	0.6 %	0.4 %

Moreover, to investigate the effect of deposition pressure and robot arm speed on ITO thin film properties, ITO thin films were deposited by changing deposition pressure and robot arm speed. In Table 3.4, changing deposition parameters during the deposition are given. Other parameters were kept constant. ITO4 deposition parameters were taken as reference parameters, only deposition pressure and robot arm speed were the variable parameters in this set.

**Table 3.4** Deposition parameters of ITO thin films with different deposition pressure and robot arm speed.

<b>Deposition Parameters</b>	<b>ITO19 200 nm</b>	<b>ITO20 200 nm</b>	<b>ITO21 236 nm</b>	<b>ITO22 163 nm</b>
Deposition Pressure	3 mTorr	3 mTorr	2 mTorr	4 mTorr
Deposition Time	26 min	30 min	20 min	20 min
Speed	15cm/min	10cm/min	20cm/min	20cm/min

In conclusion, in this part of the chapter, background information about deposition techniques, cleaning procedure and different deposition parameters of a Si:H and ITO layer were given.

### **3.5 Characterization of ITO Thin Films**

Structural, optical and electrical characterization of ITO thin films were performed by using different characterization techniques. In this part of the chapter, background information about the characterization techniques used will be given.

#### **3.5.1 Four Point Probe**

Four-point probe is a useful and easy technique that leads us to gain information about sheet resistance of the sample. It has four probes, two of which give voltage while outer couple of probes measure current. In this study, sheet resistances of ITO films were measured JANDEL-RM3-AR four-point probe measurement system. If the thickness of the semiconductor is known, the resistivity of the material can be calculated. The resistivity of the semiconductor can be calculated using Eq. 3.1 if probe spacing(s) is higher than the semiconductor thickness. If probe spacing is smaller than the material thickness, correction factor must be considered to calculate film resistivity. In our case, probe spacing is higher than the film thickness and resistivity can be calculated by using Eq 3.1 where  $t$  is the thickness of the film,  $R_{\text{sheet}}$  is the sheet resistance of the film.

$$R_{\text{sheet}} = \frac{\rho}{t} \quad (\text{Eq. 3.1})$$

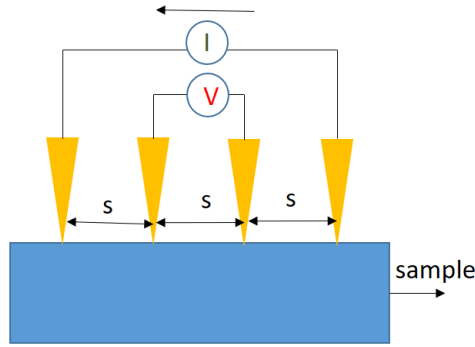


**Figure 3.5** Schematic configuration of four point probe system.

### 3.5.2 X Ray Diffraction Analysis

X ray Diffraction analysis is one of the main technique to obtain crystallographic information of the material. By using X ray diffraction analysis, film's crystalline size, preferential crystalline growth and strain parameter of the film can be obtained.

In order to obtain the XRD pattern of ITO thin films, Grazing-Incidence angle XRD (GI-XRD) analysis was used. Since X-ray has a large penetration depth, X rays can penetrate to the substrate and it is not easy to get crystallographic information of thin film with a thickness below 200 nm. Difference between GI- XRD method and the usual one come from the detector's angle. In Figure 3.6 schematic configuration of GI-XRD method is illustrated. By changing the detector's angle, path of the X rays is increased and penetration through the substrate can be under control to some extent. In this study, GI-XRD analyses were performed in Central Laboratory at METU using a CuK $\alpha$  source ( $\lambda=1.54\text{\AA}$ ). Incidence angle of detector was changed between 0.4-0.6 $^\circ$ .

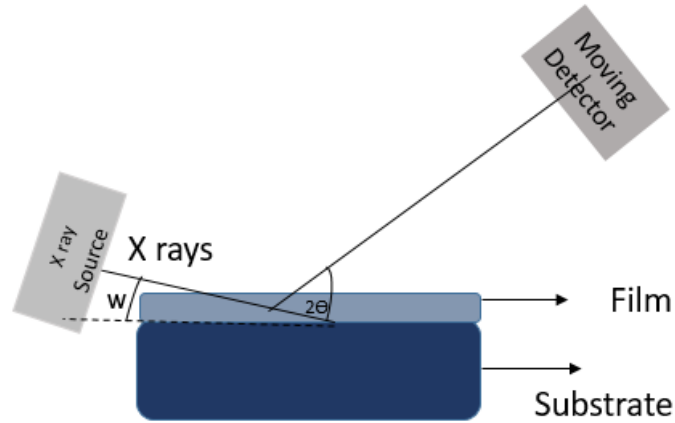


**Figure 3.6** Schematic configuration of GI-XRD system.

If incidence angle and incident X ray source are known, interplanar distance,  $d$ , can be calculated by using Bragg's Law which is given as;

$$n\lambda = 2d\sin\theta. \quad (\text{Eq.3.2})$$

In addition, crystallite size can be calculated by using Scherrer Formula.

$$t = \frac{0.9\lambda}{B\sin\theta}, \quad (\text{Eq. 3.3})$$

Where  $t$  is the crystallite size,  $B$  is the corrected peak width,  $\lambda$  is the x-ray wavelength, 0.9 is approximately equal to shape factor.

### 3.5.3 Atomic Force Microscopy

Atomic Force Microscopy (AFM) is a technique that gives the information about surface topography and surface roughness. One of the main advantage of AFM is that besides conducting materials, surface analysis of non-conducting materials can be performed by using it. It is composed of sharp cantilever with a sharp tip on its end. AFM image of ITO thin films were analyzed by Veeco MultiMode V AFM sytem in the Central Laboratory at METU. In Figure 3.7 configuration of AFM is shown.



**Figure 3.7** Configuration of Atomic Force Microscopy at Central Laboratory.

### 3.5.4 Transmission & EQE Measurements

Transmission measurement of ITO thin films were performed by Perkin Elmer Lambda 45 Spectrophotometer (Figure 3.8) in the wavelength range between 300-900 nm by using an integrated sphere. Background measurements were carried out by using a borosilicate float glass substrate as a reference in order to eliminate substrate effect.

Incident light comes through the material, some of them absorbed by the material, transmitted through the material or reflected from the surface. According to Beer Lambert's Law, intensity of the incident light decays exponentially depending on the material thickness. Absorption coefficient can be calculated using the expression given by,

$$I_T = I_0 e^{-\alpha t}, \quad (\text{Eq. 3.4})$$

where  $t$  is the thickness of the film,  $\alpha$  is the absorption coefficient,  $I_T$  and  $I_0$  intensity of the transmitted and incident light. Eq 3.4 can also be written as,

$$\alpha(\lambda) = -\frac{(\ln T)}{t}, \quad (\text{Eq. 3.5})$$

where  $t$  is the thickness of the film,  $T$  is the transmittance of the sample and it is simply calculated by dividing transmitted light intensity and incident light intensity ( $I_T/I_0$ ). After calculation of absorption coefficient, optical bandgap can be obtained by using Eq. 3.6,

$$(\alpha h\nu) = A(h\nu - E_g)^k. \quad (\text{Eq. 3.6})$$

where  $A$  is the independent constant which is related to the transition probability,  $h$  is the Planck constant,  $\nu$  is the applied frequency,  $\alpha$  is the absorption coefficient,  $k$  is constant related to the bandgap structure of the semiconductor. For direct transitions,  $k$  is equal to  $1/2$ , ITO films exhibit direct transition between valance and conduction band.

Optical bandgap of ITO can be calculated by using Tauc plot which is extracted from Eq.3.6. Linear fit of  $(\alpha h\nu)^2$  versus  $h\nu$  graph gives energy bandgap of the semiconductor. Moreover, since ITO has transmittance in the UV-Visible range of the spectrum, effect of the reflection spectra is negligible.



**Figure 3.8** Perkin Elmer Lambda 45 Spectrophotometer.

### 3.5.5 EQE Measurements

EQE measurements were performed by PVE300 Bentham Spectroscopy device in the wavelength range between 250 -1200 nm. Schematic configuration of the device is shown in Figure 3.9. The device also includes reflection & transmission setup and EQE setup. Monochromoter, halogen and Xenon lamps, vacuum controller unit and stage utility were used during the measurements.

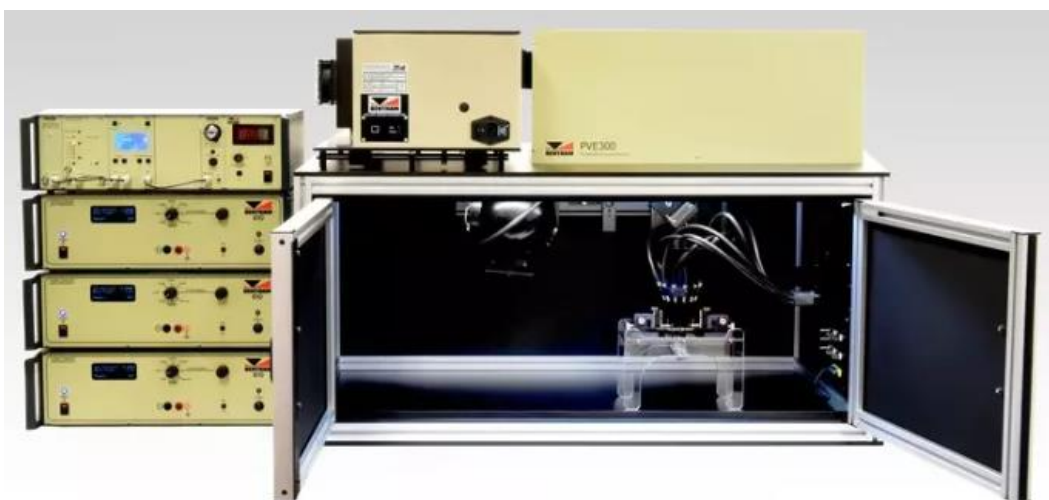


**Figure 3.9** PVE300 Bentham device [70] .

### 3.5.6 Hall Effect Measurement

Hall Effect measurements of ITO thin films were performed by NanoMagnets Hall Effect Instrument System (Figure 3.10) at room temperature and at constant magnetic field. During these measurements current was applied by Keithley 220 current source and voltage was read from Keithley 619 source. To form ohmic contact between metal and ITO thin films, surface of the films was coated with Ag by using shadow mask with van der Pauw geometry. The thickness of deposited metal layer was around 400 nm. After deposition, samples were annealed at 100 °C for 30 minutes to improve the ohmic contact formation.

In semiconducting materials, motion of charge carriers is related to conduction mechanism of the material. For this reason, it is important to understand the motion of charge carriers, carrier concentration and mobility. Hall Effect experiment is an important tool which gives information about carrier mobility and concentration which was proposed by Hall [71]. When external magnetic field is applied to the material in the perpendicular direction of motion of charge carriers, Lorentz force will appear which is formulated as Eq.3.8 where  $q$  is the magnitude of carrier charge and  $\vec{V}$  is the drift velocity of the electrons and  $\vec{E}$  and  $\vec{B}$  applied electric and magnetic field respectively.

$$q(\vec{V} \times \vec{B}) + q\vec{E} = 0 . \quad (\text{Eq.3.8})$$

If the current flow is in the x direction and the applied magnetic field in z direction, at the equilibrium, Lorentz force can be written as Eq.3.9

$$E_y = -\frac{1}{nq} B_z J_x , \quad (\text{Eq.3.9})$$

where  $J_x$  is the current density created by drift velocity and it is written as;

$$\vec{J} = qn\vec{V}, \quad (\text{Eq.3.10})$$

where  $\vec{V}$  is the drift velocity of the charge carriers,  $n$  is the concentration of charge carriers.

By using Ohm's Law, current density can be expressed as a function of conductivity and applied Electric field (Eq.3.11). Also, mobility ( $\mu$ ) is expressed drift velocity per unit electric field (Eq.3.12)

$$\vec{J} = \sigma \vec{E} . \quad (\text{Eq.3.11})$$

$$\vec{V} = \mu \vec{E} . \quad (\text{Eq.3.12})$$

Using relationship between Eq. 3.11 and Eq.3.12 conductivity,  $\sigma$ , is expressed as Eq.3.14.

$$\sigma = nq\mu. \quad (\text{Eq.3.14})$$

Hall Coefficient can be defined as Eq.3.14 which is inversely proportional to the concentration of charge carriers. Negative sign refers to type of charge carriers.

$$R_H = -\frac{1}{nq} \quad (\text{Eq.3.14})$$



**Figure 3.10** Hall Effect Measurement System.

### **3.5.7 Spectroscopic Ellipsometry (SE)**

Thickness of ITO thin films were measured by using spectroscopic ellipsometry technique. Basically, Spectroscopic ellipsometry is the measurement technique to characterize thickness and optical properties such as refractive index, extinction coefficient and optical bandgap of the semiconductors. Main advantage of ellipsometry is that it is a non-destructive and contactless thin film characterization technique. Polarized incident light interacts with the surface of the sample and then

reflected from the surface by using another polarizer (Figure 3.11). Change in polarization states results in having information about optical properties of the samples.

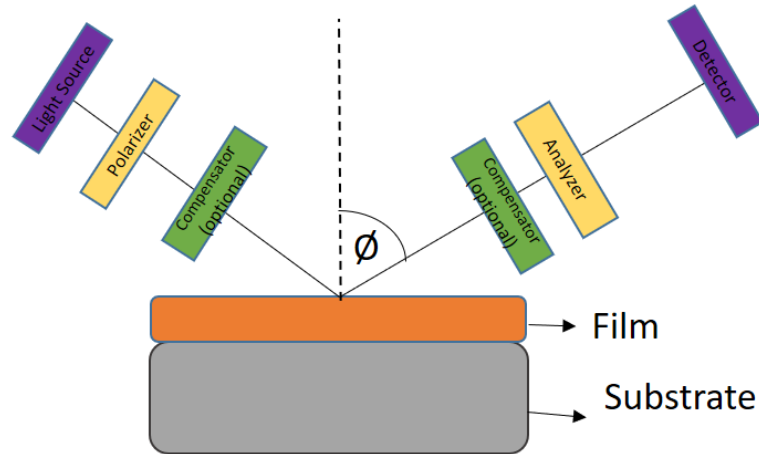


**Figure 3.11** Schematic configuration of Spectroscopic Ellipsometry

$$\rho = \frac{R_p}{R_s} = \tan\varphi e^{i\Delta} \quad (\text{Eq.3.15})$$

Complex reflectance ratio,  $\rho$ , measured by ellipsometry and it is equal to ratio of  $R_p$  and  $R_s$  which are the two parameters related to s and p polarization states. Reflectance ratio can also be expressed by,  $\tan\varphi$ , amplitude ratio, and the phase difference,  $\Delta$  (Eq.3.15). By using these measurements, some optical parameters of semiconductor can be extracted from ellipsometry.

Since ITO is heavily doped n type degenerate semiconductor, to calculate its thickness and its electrical & optical properties, Drude model was used to determine conductivity values and Tauc-Lorentz model was used to determine thickness of the thin films.

### 3.6 Contact Resistivity Analysis

The samples used in contact resistivity analysis were prepared by using two shadow masks, PECVD, sputtering and evaporation systems. After metallization by

evaporation, the samples were annealed at 20 °C for 15 minutes to improve ohmic contact formation. To calculate specific contact resistivity of the ITO layer and metal contacts, two different TLM masks were prepared by using laser marker and multi crystalline wafer. In Figure 3.14, contact separations and contact dimensions are shown for the two different shadow masks. Also, to prevent current flow to the opposite direction (current flow through a wafer) and to make more reliable contact resistivity analogy, SiO<sub>2</sub> layer was deposited onto n type wafers. Deposited SiO<sub>2</sub> layer was around 1 um. After deposition of SiO<sub>2</sub> layer, two different types of samples were prepared. Prepared samples to measure contact resistivity value of ITO/Ag layers are illustrated in Figure 3.12. In addition, for the same reasons, different test structures were developed in order make more consistent extraction from the TLM measurements. Intrinsic a-Si:H and p a-Si:H layers were deposited onto rear side of the n type wafer to passivate the rear side and to minimize the current loss to the opposite direction [72]. In Figure 3.13, prepared test structures with rear side passivation, are shown.

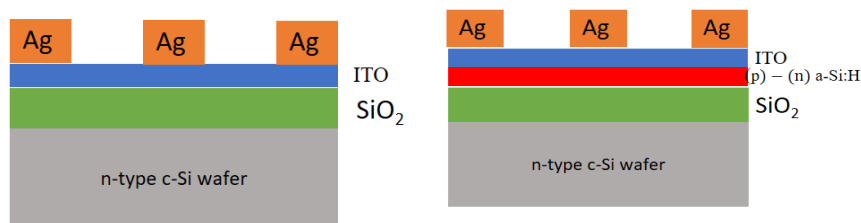


**Figure 3.12** The test structures used to determine ITO/Ag contact resistivity.

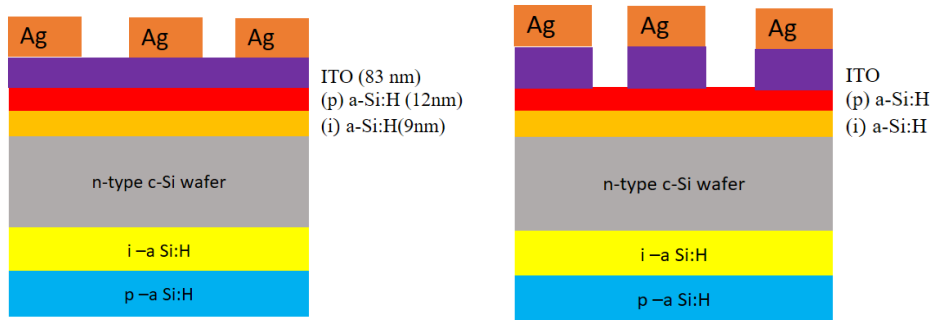


**Figure 3.13** The test structures with passivating i and p a-Si:H layers.

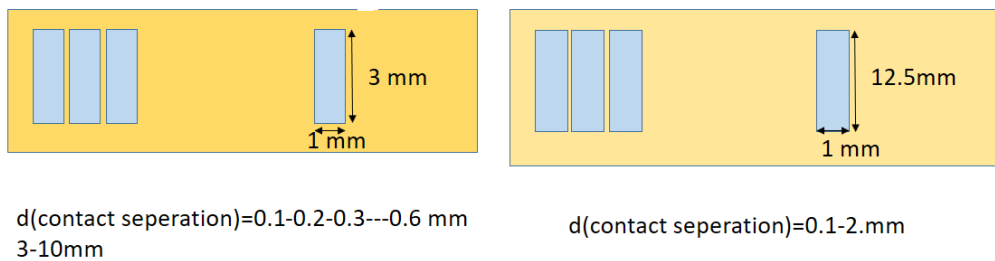


**Figure 3.14** Prepared shadow masks for TLM measurements. Mask 1 design is adapted from [73].

### 3.6.1 Metallization by Thermal Evaporation

Thermal Evaporation System was used to deposit metal contact for the samples that use in Hall Effect and contact resistivity analysis. Thermal Evaporation is one of the most common PVD process and it is basically consisted of vacuum chamber, vacuum pump, sample holder, resistive boat and power supply. Resistive boat is used to heat source material. Boat is heated by electrical resistance and source material is melted under high vacuum. By means of high vacuum, melted source material goes up through the substrate without interacting any other material inside the chamber. Thermal evaporation system is schematically shown in 3.15. Base pressure was around  $2 \times 10^{-5}$  Torr during the deposition.

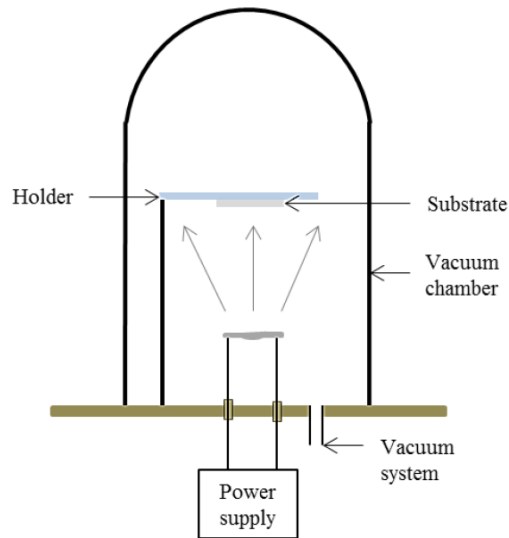


**Figure 3.15** Schematic representation of thermal evaporation system [36].

### 3.6.2 Current –Voltage Measurements in Dark Condition

I-V measurements were performed by using the Protoflex Solar Simulator system under the dark conditions. In Figure 3.16, solar simulator and one of the sample used in contact resistivity analysis is shown. Voltage was applied between +1 and -1 Volt from the Keithley 2425 source and the current is measured. There are four probes in this system, two of which are responsible from voltage, while the others are responsible for current detection. These four probes are signatone probes which means they have magnets which restrict the motion of probes. This results in decreasing damage of the metal contact and helps to make more accurate I-V measurements. In our TLM analysis, voltage was applied to the front side of the sample and resulting current was determined from the Keithley 2425 source.

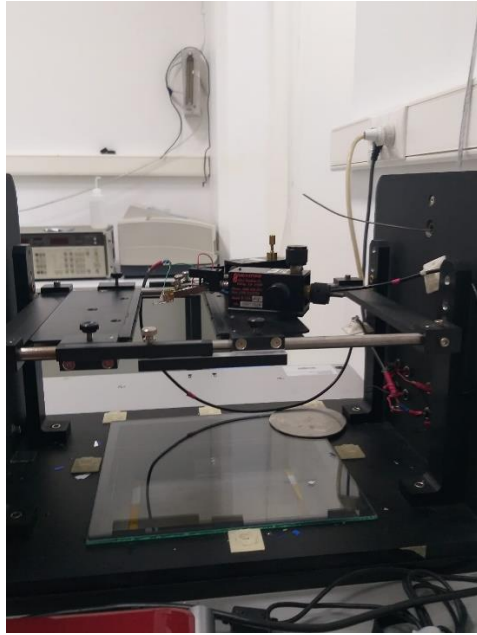


**Figure 3.16** Solar Simulator System.



## **CHAPTER 4**

### **RESULTS AND DISCUSSION**

#### **4.1 Introduction**

In this chapter, electrical, optical, structural and morphological characterization results of the deposited ITO thin films will be presented and discussed. Electrical characterization includes resistivity, sheet resistance and mobility measurements. In this part, effect of deposition parameters and the post annealing temperature on the electrical properties of ITO thin films will be discussed. In the structural and morphological characterization part, effect of O<sub>2</sub>/Ar ratio in the deposition chamber and post-annealing temperature on crystallographic and topographic properties of ITO films will be argued. In addition, specific contact resistivity measurement results of different layers in the SHJ structure and different methods used for the contact resistivity analysis will be discussed. As the last part, performance of SHJ cells deposited with different ITO layers and the effect of ITO layers on SHJ cell parameters will be discussed in detail.

#### **4.2 Electrical Characterizations**

##### **4.2.1 Change of resistivity with RF Power and Substrate Temperature**

The deposition of ITO thin films was first performed by changing RF power and substrate temperature. In the first three deposition cycles (sample are coded as ITO1, ITO2 and ITO3), substrate temperature was 100 °C and RF power was 200, 300, 400 Watt. Other parameters such as deposition pressure (3 mTorr), robot arm speed which controls holder speed during the deposition (20 cm/min) and Ar flow rate (125 sccm) were kept constant. In this set, the sheet resistance of ITO thin films before the post annealing process were changing between 50 Ω/square and 18 Ω/square and

the film resistivity was in the order of  $10^{-4}$   $\Omega$ .cm. Although there were some exceptions, lowest resistivity values were obtained when the annealing temperature was kept at 200 °C, then at the substrate temperature of 225 °C resistivity values slightly increased. Table 4.1; 4.2 and 4.3, average sheet resistance and resistivity values of ITO thin films deposited at the substrate temperature of 100 °C, with different power values are given.

**Table 4.1** Sheet resistance and resistivity results of ITO1 samples before and after annealing.

Sample Code	Annealing Temperature (°C)	Average sheet resistance ( $\Omega$ /square)		Resistivity ( $\Omega$ .cm)	
		Before Annealing	After Annealing	Before Annealing	After Annealing
ITO1  RF Power 200 W	150	50.3	32.5	$4.83 \times 10^{-4}$	$3.12 \times 10^{-4}$
	175	45.3	30.5	$4.35 \times 10^{-4}$	$2.93 \times 10^{-4}$
	200	51.4	21.5	$4.93 \times 10^{-4}$	$2.06 \times 10^{-4}$
	225	46.7	28.6	$4.48 \times 10^{-4}$	$2.75 \times 10^{-4}$

**Table 4.2** Sheet resistance and resistivity results ITO2 samples before and after annealing.

Sample Code	Annealing Temperature (°C)	Average sheet resistance ( $\Omega$ /square)		Resistivity ( $\Omega$ .cm)	
		Before Annealing	After Annealing	Before Annealing	After Annealing
ITO2  RF Power 300 W	150	34.1	15.3	$3.17 \times 10^{-4}$	$1.42 \times 10^{-4}$
	175	37.2	20.4	$3.46 \times 10^{-4}$	$1.90 \times 10^{-4}$
	200	38.5	11.8	$3.58 \times 10^{-4}$	$1.10 \times 10^{-4}$
	225	35.1	35.6	$3.26 \times 10^{-4}$	$3.31 \times 10^{-4}$

**Table 4.3** Sheet resistance and resistivity results of ITO3 samples before and after annealing.

Sample Code	Annealing Temperature (°C)	Average sheet resistance ( $\Omega$ /square)		Resistivity ( $\Omega$ .cm)	
		Before Annealing	After Annealing	Before Annealing	After Annealing
ITO3					
RF Power 400 W	150	20.07	10.8	$3.61 \times 10^{-4}$	$1.94 \times 10^{-4}$
	175	19.54	11.8	$3.52 \times 10^{-4}$	$2.12 \times 10^{-4}$
	200	18.27	11.5	$3.29 \times 10^{-4}$	$2.07 \times 10^{-4}$
	225	20.95	25.9	$3.77 \times 10^{-4}$	$4.66 \times 10^{-4}$

In the following three deposition cycles, substrate temperature was increased to 200 °C and RF power values were kept at 200, 300, 400 Watt. For all three sets of thin film samples (coded as ITO4, ITO5, ITO6), resistivity values are obtained in the order of  $10^{-4} \Omega$ .cm which are almost the same as the values of the films obtained in the first deposition cycle and average sheet resistance values change in between 9 and 37  $\Omega$ / square (Table 4.4, Table 4.5 and Table 4.6). For these samples the post annealing process on the obtained parameters seem to be less effective when compared to the first group of samples (ITO1, ITO2 and ITO3) which were grown at the substrate temperature of 100 °C and the low value of substrate temperature might be the reason of stronger effect of the post annealing process on the resistivity values.

**Table 4.4** Sheet resistance and resistivity results of ITO4 samples before and after annealing.

Sample Code	Annealing Temperature (°C)	Average sheet resistance ( $\Omega$ /square)		Resistivity ( $\Omega$ .cm)	
		Before Annealing	After Annealing	Before Annealing	After Annealing
RF Power 400 W	150	9.17	9.07	$2.10 \times 10^{-4}$	$2.08 \times 10^{-4}$
	175	9.26	9.06	$2.13 \times 10^{-4}$	$2.08 \times 10^{-4}$
	200	9.21	9.49	$2.12 \times 10^{-4}$	$2.18 \times 10^{-4}$
	225	9.28	8.94	$2.13 \times 10^{-4}$	$2.05 \times 10^{-4}$

**Table 4.5** Sheet resistance and resistivity results of ITO5 samples before and after annealing.

Sample Code	Annealing Temperature (°C)	Average sheet resistance ( $\Omega$ /square)		Resistivity ( $\Omega$ .cm)	
		Before Annealing	After Annealing	Before Annealing	After Annealing
RF Power 300 W	150	15.1	14.4	$2.84 \times 10^{-4}$	$2.70 \times 10^{-4}$
	175	14.9	13.8	$2.80 \times 10^{-4}$	$2.60 \times 10^{-4}$
	200	15.8	13.6	$2.96 \times 10^{-4}$	$2.55 \times 10^{-4}$
	225	14.8	14.1	$2.78 \times 10^{-4}$	$2.65 \times 10^{-4}$

**Table 4.6** Sheet resistance and resistivity results of ITO6 samples before and after annealing.

Sample Code	Annealing Temperature (°C)	Average sheet resistance ( $\Omega$ /square)		Resistivity ( $\Omega$ .cm)	
		Before Annealing	After Annealing	Before Annealing	After Annealing
ITO6 RF Power 200 W	150	37.4	35.5	$3.73 \times 10^{-4}$	$3.55 \times 10^{-4}$
	175	32.7	31.3	$3.26 \times 10^{-4}$	$3.13 \times 10^{-4}$
	200	30.5	29.9	$3.04 \times 10^{-4}$	$2.98 \times 10^{-4}$
	225	33.3	34.8	$3.33 \times 10^{-4}$	$3.47 \times 10^{-4}$

In all six depositions, resistivity values of ITO films are in the order  $10^{-4} \Omega$ .cm with a slight decrease with post annealing process. Among the six different ITO films deposited with different growth parameters, deposition parameters of the ITO4 sample, chosen as a standard recipe for the ITO thin film depositions, such as 200 °C and 400 W for the substrate temperature and RF power respectively. The effect of the other deposition parameters on the film properties were kept under investigation. The main reason of choosing ITO4 deposition conditions as a standard recipe, is that, ITO4 thin films have lowest resistivity values before the post annealing process and its resistivity values did not fluctuate with post annealing process. Also the lowest sheet resistance values were obtained from this group of films.

To summarize the effect of RF power and substrate temperature on the properties of the grown ITO films, the typical graph of resistivity values concerning different RF Power without post-annealing process are shown in Figure 4.1 (for the as grown ITO4, ITO5 and ITO6 samples). Increasing RF power results a slight decrease of the film resistivity.

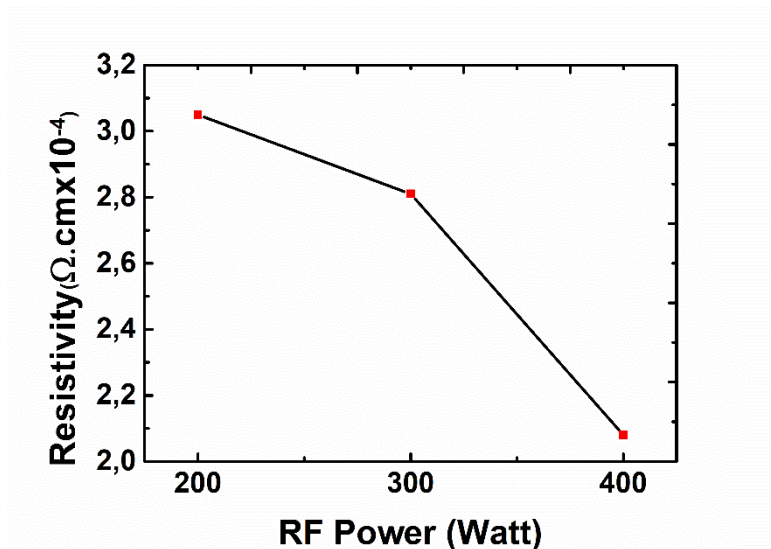


**Figure 4.1** Change of resistivity with RF Power (for samples *ITO6*, *ITO5* and *ITO4*).

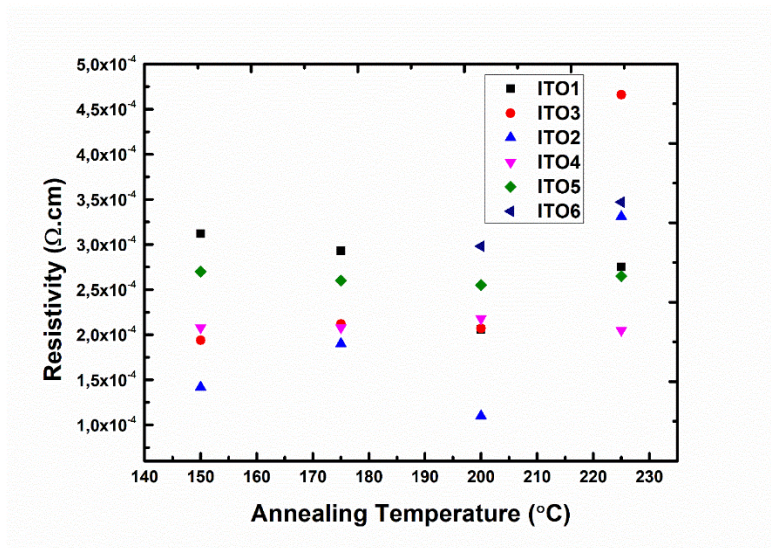


**Figure 4.2** Resistivity values at different annealing temperatures.

Moreover, to conclude the effect of post annealing process, resistivity values of the all six ITO samples concerning different post-annealing temperature are shown in Figure 4.2. For the samples annealed at 225 °C, resistivity values slightly increase, but there is no sharp variance of resistivity and lowest resistivity values, in general, they were found when the annealing temperature was kept 200 °C.

#### 4.2.2 Effect of Oxygen/Argon Ratio on the Resistivity of the ITO Films

To examine the effect of different gas mixtures and ratios in the deposition chamber, on the properties of ITO films, besides Argon, Oxygen was introduced to the sputtering chamber with different ratios during the depositions. A series of deposition cycles were performed by changing O<sub>2</sub>/Ar ratio, while the other deposition parameters were kept same as of reference sample (ITO4). In the first two deposition cycles with oxygen, O<sub>2</sub>/Ar ratio values were arranged as 5% and 3%. Sheet resistance and resistivity values of these samples are given in Table 4.7 and 4.8. Resistivity values of these samples, are higher when compared to the reference sample, but sheet resistance and resistivity values decrease with annealing. Post annealing process had more pronounced effect on the electrical properties of these samples than those deposited without oxygen. Besides, increasing oxygen content in the gas mixture leads to an increase in the resistivity values. When the O<sub>2</sub>/Ar ratio is equal to 1 %, 0.8 %, resistivity values of the films approach to almost the same resistivity values of ITO films grown without oxygen (Table 4.9 and 4.10).

**Table 4.7** Sheet resistance and resistivity results of ITO10 samples before and after annealing.

Sample Code	Annealing Temperature (°C)	Average sheet resistance (kΩ/square)		Resistivity (Ω.cm)	
		Before Annealing	After Annealing	Before Annealing	After Annealing
5% O <sub>2</sub> /Ar Ratio	150	9.4	3.7	7.4x10 <sup>-2</sup>	3.0x10 <sup>-2</sup>
	175	8.8	2.3	6.9x10 <sup>-2</sup>	2.0x10 <sup>-2</sup>
	200	8.0	1.1	6.3x10 <sup>-2</sup>	8.6x10 <sup>-3</sup>
	225	10.2		8.0x10 <sup>-2</sup>	5.5x10 <sup>-3</sup>

**Table 4.8** Sheet resistance and resistivity results of ITO11 samples before and after annealing.

Sample Code	Annealing Temperature (°C)	Average sheet resistance (kΩ/square)		Resistivity (Ω.cm)	
		Before Annealing	After Annealing	Before Annealing	After Annealing
3 % O <sub>2</sub> /Ar Ratio	150	6.6	2.6	5.8x10 <sup>-2</sup>	2.3x10 <sup>-2</sup>
	175	7.0	6.5	6.1x10 <sup>-2</sup>	5.6x10 <sup>-2</sup>
	200	4.5		3.9x10 <sup>-2</sup>	5.6x10 <sup>-3</sup>
	225	5.6	0.54	4.9x10 <sup>-2</sup>	4.7x10 <sup>-3</sup>

**Table 4.9** Sheet resistance and resistivity results ITO12 samples before and after annealing.

Sample Code	Annealing Temperature (°C)	Average sheet resistance (Ω/square)		Resistivity (Ω.cm)	
		Before Annealing	After Annealing	Before Annealing	After Annealing
1 % O <sub>2</sub> /Ar Ratio	150	62.4	59.5	8.6x10 <sup>-4</sup>	8.2x10 <sup>-4</sup>
	175	53.8	50.6	7.4x10 <sup>-4</sup>	6.9x10 <sup>-4</sup>
	200	59.7	57.8	8.2x10 <sup>-4</sup>	8.0x10 <sup>-4</sup>
	225	67.7	71.6	8.3x10 <sup>-4</sup>	9.8x10 <sup>-4</sup>

**Table 4.10** Sheet resistance and resistivity results of ITO13 samples before and after annealing.

Sample Code	Annealing Temperature (°C)	Average sheet resistance ( $\Omega$ /square)		Resistivity ( $\Omega$ .cm)	
		Before Annealing	After Annealing	Before Annealing	After Annealing
ITO13  0.8 % O <sub>2</sub> /Ar Ratio	150	35.7	34.6	$5.29 \times 10^{-4}$	$5.12 \times 10^{-4}$
	175	34.1	35.5	$5.05 \times 10^{-4}$	$5.05 \times 10^{-4}$
	200	35.8	37.4	$5.30 \times 10^{-4}$	$5.53 \times 10^{-4}$
	225	34.0	39.9	$5.03 \times 10^{-4}$	$5.9 \times 10^{-4}$

**Table 4.11** Sheet resistance and resistivity results of ITO17 samples before and after annealing.

Sample Code	Annealing Temperature (°C)	Average sheet resistance ( $\Omega$ /square)		Resistivity ( $\Omega$ .cm)	
		Before Annealing	After Annealing	Before Annealing	After Annealing
ITO17  0.6 % O <sub>2</sub> /Ar Ratio	150	28.5	27.0	$4.5 \times 10^{-4}$	$4.3 \times 10^{-4}$
	175	27.5	28.3	$4.4 \times 10^{-4}$	$4.5 \times 10^{-4}$
	200	28.7	26.2	$4.5 \times 10^{-4}$	$4.2 \times 10^{-4}$
	225	29.5	42.0	$4.6 \times 10^{-4}$	$6.6 \times 10^{-4}$

**Table 4.12** Sheet resistance and resistivity results of ITO23 samples before and after annealing.

Sample Code	Annealing Temperature (°C)	Average sheet resistance ( $\Omega$ /square)		Resistivity ( $\Omega$ .cm)	
		Before Annealing	After Annealing	Before Annealing	After Annealing
ITO23 0.4 % O <sub>2</sub> /Ar Ratio	150	24.4	21.5	$3.78 \times 10^{-4}$	$3.33 \times 10^{-4}$
	175	23.9	22.3	$3.64 \times 10^{-4}$	$3.45 \times 10^{-4}$
	200	22.5	24.4	$3.49 \times 10^{-4}$	$3.79 \times 10^{-4}$
	225	23.7	26.6	$3.67 \times 10^{-4}$	$4.12 \times 10^{-4}$

Decreasing O<sub>2</sub>/Ar ratio during the deposition led to decrease in resistivity values. In Table 4.11 and 4.12, average sheet resistance and resistivity values of ITO17 and ITO23 samples are given. They were deposited Oxygen/Argon ratio is equal to 0.6 % and 0.4 % respectively. For these samples, resistivity values were in the order of  $10^{-4}$   $\Omega$ .cm and they are almost equal to resistivity values with respect to reference sample.

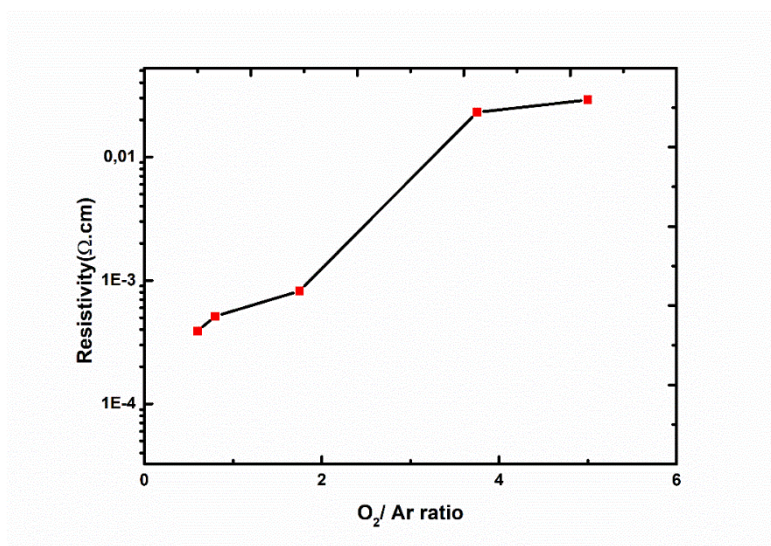


**Figure 4.3** Change of resistivity with O<sub>2</sub>/Ar ratio.

In Figure 4.3, different resistivity values concerning different O<sub>2</sub>/Ar ratio is illustrated as a summary. It can be concluded that increasing oxygen content leads to a strong increase in resistivity.

#### **4.1.3 Effect of Deposition Rate and Deposition Pressure on the Resistivity**

To investigate the effect of different deposition pressure and deposition rate (robot arm/holder speed) on the electrical properties, ITO thin film depositions were performed by changing these parameters. Other parameters were same as our reference sample (ITO4). Results showed that there was no substantial effect of holder speed and deposition pressure on the film resistivity. In Table 4.13 and 4.14, average sheet resistance and resistivity values of ITO thin films deposited with different robot arm speed are shown. In Table 4.15 and 4.16 average sheet resistance and resistivity values ITO films with different deposition pressure are given. In Figure 4.4 and 4.5, resistivity values of ITO thin films for different robot arm speed and deposition pressure values are shown for comparison. In both graphs, though there are some attenuation in resistivity values with respect to the different annealing temperature, the resistivity values of the samples are in the order of  $10^{-4} \Omega \cdot \text{cm}$  which is consistent with the literature and the previous results. These fluctuations might be related to standard deviation of resistivity calculations. Since there are no considerable differences when compared to the previous resistivity results, robot arm speed and deposition pressure values used for the deposition of reference sample (3 mTorr and 20 cm/min), were taken as the standard values for the deposition of all ITO thin films for further studies.

**Table 4.13** Sheet resistance and resistivity results of ITO19 samples before and after annealing.

Sample Code	Annealing Temperature (°C)	Average sheet resistance ( $\Omega$ /square)		Resistivity ( $\Omega$ .cm)	
		Before Annealing	After Annealing	Before Annealing	After Annealing
Speed 10 cm/min	150	12.2	11.8	$2.43 \times 10^{-4}$	$2.35 \times 10^{-4}$
	175	11.8	10.5	$2.35 \times 10^{-4}$	$2.11 \times 10^{-4}$
	200	12.05	11.0	$2.41 \times 10^{-4}$	$2.21 \times 10^{-4}$
	225	12.5	10.5	$2.5 \times 10^{-4}$	$2.1 \times 10^{-4}$

**Table 4.13** Sheet resistance and resistivity results of ITO20 samples before and after annealing.

Sample Code	Annealing Temperature (°C)	Average sheet resistance ( $\Omega$ /square)		Resistivity ( $\Omega$ .cm)	
		Before Annealing	After Annealing	Before Annealing	After Annealing
Speed 15 cm/min	150	11.09	11.18	$2.62 \times 10^{-4}$	$2.64 \times 10^{-4}$
	175	12.07	10.44	$2.85 \times 10^{-4}$	$2.46 \times 10^{-4}$
	200	10.97	9.32	$2.59 \times 10^{-4}$	$2.20 \times 10^{-4}$
	225	12.08	9.96	$2.85 \times 10^{-4}$	$2.35 \times 10^{-4}$

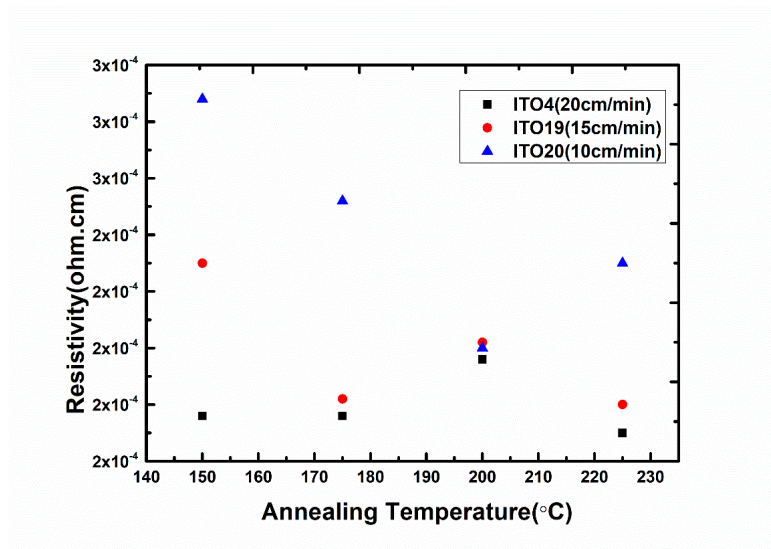


**Figure 4.4** Resistivity values with respect to different robot arm speed.

**Table 4.14** Sheet resistance and resistivity results of ITO21 samples before and after annealing.

Sample Code	Annealing Temperature (°C)	Average sheet resistance (Ω/square)		Resistivity (Ω.cm)	
		Before Annealing	After Annealing	Before Annealing	After Annealing
Deposition pressure 4 mTorr	150	16.7	15.9	2.72x10 <sup>-4</sup>	2.59x10 <sup>-4</sup>
	175	17.3	15.2	2.82x10 <sup>-4</sup>	2.47x10 <sup>-4</sup>
	200	16.5	20.2	2.69x10 <sup>-4</sup>	3.28x10 <sup>-4</sup>
	225	18.1	12.1	2.95x10 <sup>-4</sup>	1.97x10 <sup>-4</sup>

**Table 4.15** Sheet resistance and resistivity results of ITO22 samples before and after annealing.

Sample Code	Annealing Temperature (°C)	Average sheet resistance ( $\Omega$ /square)		Resistivity ( $\Omega$ .cm)	
		Before Annealing	After Annealing	Before Annealing	After Annealing
Deposition Pressure 2 mTorr	150	29.18	18.05	$4.44 \times 10^{-4}$	$2.74 \times 10^{-4}$
	175	19.55	17.12	$2.97 \times 10^{-4}$	$2.6 \times 10^{-4}$
	200	18.79	14.5	$2.86 \times 10^{-4}$	$2.2 \times 10^{-4}$
	225	20.24	9.46	$3.08 \times 10^{-4}$	$1.44 \times 10^{-4}$

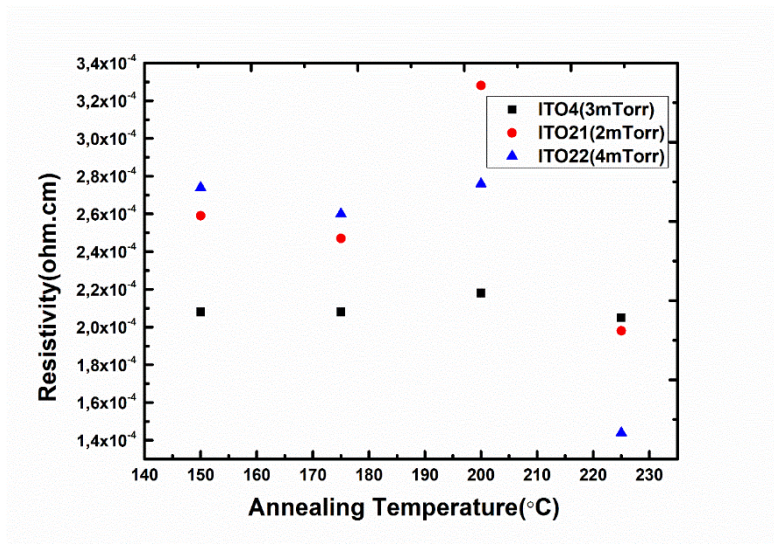


**Figure 4.5** Change of resistivity with respect to different deposition pressure.

### 4.2.3 Mobility and Scattering Mechanisms

Mobility values of grown ITO films without oxygen, changed between 10-22  $\text{cm}^2/\text{V}\cdot\text{s}$ . Carrier density of ITO films was in the range of  $10^{21} \text{ cm}^{-3}$ . In the first three ITO depositions, mobility and carrier density values of the films were in the range of 10-13  $\text{cm}^2/\text{V}\cdot\text{s}$  and  $10^{21} \text{ cm}^{-3}$  respectively (ITO1, ITO2, ITO3 samples). In these three deposition cycles, substrate temperature was kept constant at 100 °C, while RF power values were changed as 200W, 300W and 400W. In the other three deposition cycles (ITO4, ITO5 and ITO6 samples) for which the substrate temperature was 200 °C and RF powers are 400W, 300W, 200W, mobility values and the carrier density values of the films were obtained in the range of 18 and 22  $\text{cm}^2/\text{V}\cdot\text{s}$  and  $10^{21} \text{ cm}^{-3}$  respectively. Substrate temperature and RF power had no significant effect on the carrier density of ITO thin films. However, increasing RF power resulted in an increase in mobility.

Moreover, effect of the deposition pressure and robot arm speed on the mobility and carrier density values was also negligible. In Table 4.16, mobility, carrier density and resistivity values of ITO films deposited without oxygen, using different deposition parameters are presented. On the other hand, changing oxygen content strongly affected the carrier concentration and mobility values. In Table 4.17, mobility, carrier density and resistivity values of ITO thin films grown with different  $\text{O}_2/\text{Ar}$  ratio are given. The pronounced effect of oxygen content on the electrical properties of the films can be explained by the dominance of different scattering mechanisms [52]. Changing oxygen content might affect the scattering mechanism of the ITO thin films. When  $\text{O}_2/\text{Ar}$  ratio was 5% and 3%, grain boundary scattering mechanism might be the dominant scattering mechanism. In this case, mobility and carrier concentration were proportional to each other and this scattering mechanism caused the decrease in mobility and increase in resistivity values notably. As can be seen in Table 4.17, mobility and carrier density values give the indication of the dominance of the grain boundary scattering mechanism for these thin film samples. The main reason of presence of this scattering mechanism might be the excess of

oxygen content. Excess oxygen content resulted in depletion of free carriers by accumulating at the grain boundaries. This can be considered as a potential barrier for electrons. [45].

Lowering oxygen content resulted the decrease in the accumulation of excess oxygen at the grain boundaries which leads the change in scattering mechanism. In contrast to the samples deposited with 5% and 3 % O<sub>2</sub>/Ar ratio, ionized impurity scattering mechanism can be dominant scattering mechanism for the samples deposited with O<sub>2</sub>/Ar ratio less than 3 %. In this case, carrier density and mobility values were inversely proportional to each other and the highest contribution to the mobility was related to the scattering of active impurity atoms (Sn<sup>+</sup> atoms and Oxygen vacancies) in the lattice structure. They scatter under the influence of Coulomb interaction. When O<sub>2</sub>/Ar ratio was 1 %, ionized impurity scattering starts to dominate the motion of charge carriers and it was also dominant scattering mechanism for the samples grown without oxygen.

To summarize the results of the study on the electrical properties of the deposited ITO thin films, the optimum electrical parameters were obtained when O<sub>2</sub>/ Ar ratio was 0.6 % (ITO17). For this sample, mobility has the highest value of 30 cm<sup>2</sup>/V. s and resistivity is in the order of 10<sup>-4</sup>Ω.cm. Moreover, carrier density was around 10<sup>20</sup> cm<sup>-3</sup> which was lower one order of magnitude than that of ITO films deposited without oxygen. Therefore, it was concluded that the films deposited with the parameters of the samples labeled as ITO17 had the appropriate electrical parameters for their usage in the suitable layer for SHJ structure, to decrease the parasitic absorption and improve the electrical transport mechanism between the a-Si:H layers.

**Table 4.16** Mobility, carrier density, Hall coefficient and resistivity of ITO thin films with different deposition parameters.

<b>Sample Code</b>	<b>R<sub>H</sub> (cm<sup>3</sup>/Columb)</b>	<b>Mobility (cm<sup>2</sup>/V.s)</b>	<b>Resistivity (Ω.cm)</b>	<b>Carrier Density (cm<sup>-3</sup>)</b>
ITO1	1.74x10 <sup>-3</sup>	10	4.83x10 <sup>-4</sup>	3.59x10 <sup>21</sup>
ITO2	1.08x10 <sup>-3</sup>	12	3.17x10 <sup>-4</sup>	3.47x10 <sup>21</sup>
ITO3	1.65x10 <sup>-3</sup>	13	3.61x10 <sup>-4</sup>	3.79x10 <sup>21</sup>
ITO4	7.75x10 <sup>-3</sup>	18	2.1x10 <sup>-4</sup>	8.05x10 <sup>21</sup>
ITO5	2.38x10 <sup>-3</sup>	20	2.84x10 <sup>-4</sup>	2.61x10 <sup>21</sup>
ITO6	4.32x10 <sup>-3</sup>	19	3.73x10 <sup>-4</sup>	1.44x10 <sup>21</sup>
ITO19	3.34x10 <sup>-3</sup>	18	2.43x10 <sup>-4</sup>	1.87x10 <sup>21</sup>
ITO20	2.63x10 <sup>-3</sup>	17	2.62x10 <sup>-4</sup>	2.36x10 <sup>21</sup>
ITO21	3.66x10 <sup>-3</sup>	18	2.72x10 <sup>-4</sup>	1.78x10 <sup>21</sup>
ITO22	3.43x10 <sup>-3</sup>	18	4.44x10 <sup>-4</sup>	1.82x10 <sup>21</sup>

**Table 4.17** Mobility, carrier density, Hall coefficient and resistivity with respect to different oxygen content.

<b>Sample Code</b>	<b>O<sub>2</sub>/Ar Ratio</b>	<b>R<sub>H</sub> (cm<sup>3</sup>/Columb)</b>	<b>Mobility (cm<sup>2</sup>/V.s)</b>	<b>Resistivity (Ω.cm)</b>	<b>Carrier Density (cm<sup>-3</sup>)</b>
ITO10	5%	4.98x10 <sup>-1</sup>	8	7.4x10 <sup>-2</sup>	1.25x10 <sup>19</sup>
ITO11	3%	7.81x10 <sup>-2</sup>	15	5.8x10 <sup>-2</sup>	7.99x10 <sup>19</sup>
ITO12	1%	2.25x10 <sup>-2</sup>	22	8.6x10 <sup>-4</sup>	2.77x10 <sup>20</sup>
ITO13	0.8%	1.10x10 <sup>-2</sup>	25	5.3x10 <sup>-4</sup>	5.65x10 <sup>20</sup>
ITO17	0.6%	1.07x10 <sup>-2</sup>	30	4.5x10 <sup>-4</sup>	5.80x10 <sup>20</sup>
ITO23	0.4%	7.65x10 <sup>-2</sup>	25	3.8x10 <sup>-4</sup>	7.80x10 <sup>20</sup>

### 4.3 Structural Characterization

#### 4.3.1 XRD Measurement Results

To investigate the effect of deposition parameters on the crystal structure of ITO thin films, XRD measurements of ITO films deposited with different deposition parameters were performed. XRD pattern of ITO4 sample (reference sample) with different post annealing temperature are given in Figure 4.6. XRD pattern of this sample is compared to XRD of ITO films grown with different O<sub>2</sub>/Ar ratio (Figure 4.7 and Figure 4.6).

XRD analysis of ITO thin films revealed that changing annealing temperature and oxygen content in the gas mixture resulted in the change of XRD patterns of ITO thin films. ITO films grown without oxygen showed different crystallographic orientations compared to those grown with oxygen [74]. Adding oxygen content to the gas mixture fills the oxygen vacancy sites of ITO structure. Oxygen atoms diffuse through the oxygen vacancy [56]. This causes the disappearance of some peaks in XRD pattern. Also, using oxygen during the sputtering process can decrease the film growth rate [75]. This can also affect crystal growth of ITO films.

For ITO4 sample, increasing post annealing temperature led to a change in preferential orientation of the peaks (Figure 4.6). Preferential orientation of the as deposited sample is (222), while its intensity decreases with the increasing post-annealing temperature. The dominant orientation of the film annealed at 225 °C is (400). This can be evaluated as the increasing annealing temperature leads to change in preferred crystal orientation. Annealing process causes the increasing thermal energy. Increment of thermal energy might lead to change in preferential orientation.

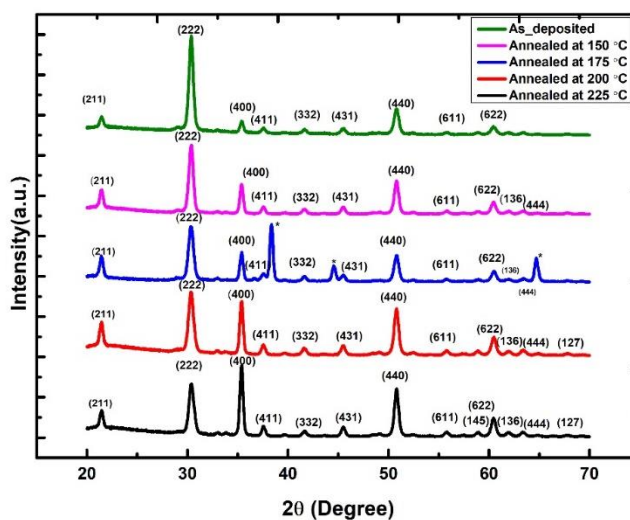


**Figure 4.6** XRD Pattern of ITO4 film with different annealing temperature.

The peak (\*) is belong to the  $\text{AgO}_2$  structure.

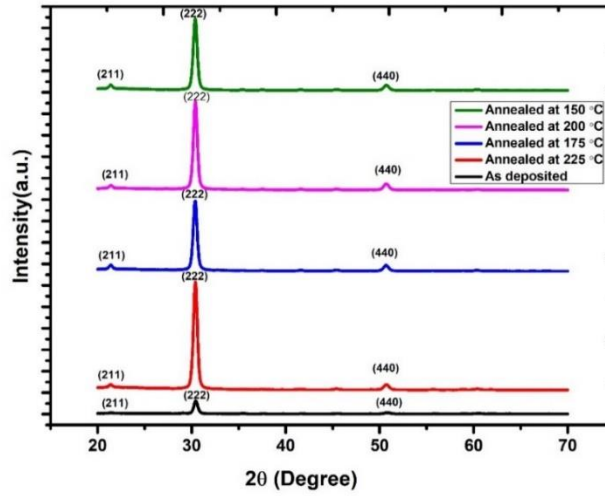


**Figure 4.7** XRD pattern of ITO12 (1 % O<sub>2</sub>/Ar ratio) sample with different annealing temperature.

When O<sub>2</sub>/Ar ratio is equal to 1 %, preferential orientation is still along (222) plane; however, some peaks disappear due to filling of oxygen vacancies (Figure 4.7). On the other hand, when O<sub>2</sub>/Ar ratio is equal to 0.4 %, intensity of (662) and (400) peaks are more prominent (Figure 4.8). This may be interpreted as, decreasing oxygen content can cause the appearance of some peaks and stabilize the crystal structure of In<sub>2</sub>O<sub>3</sub>[76].[56].

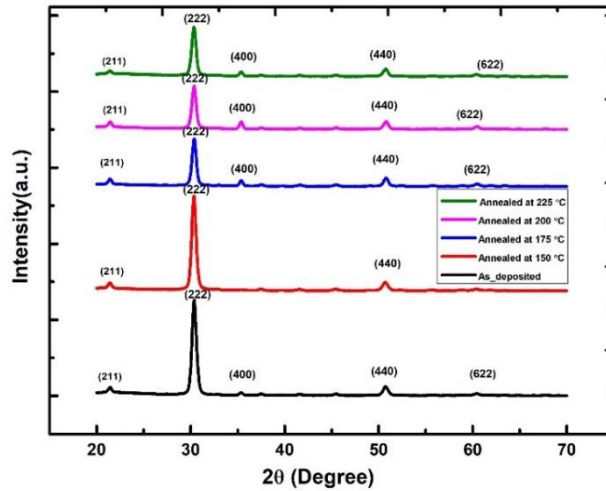


**Figure 4.8** XRD Pattern of ITO23 (0.4 % O<sub>2</sub>/Ar ratio) sample.

In Figure 4.9 XRD pattern of ITO films grown with different O<sub>2</sub>/Ar ratios are shown for comparison. Preferential orientation is along (222) plane for all as-deposited samples. However, the intensity of (222) plane of ITO film grown without oxygen has higher intensity than those grown with oxygen. In addition, for samples grown with O<sub>2</sub>/Ar ratio of 0.4 % and 1 %, some peaks disappear due to diffusion of oxygen atoms through the oxygen vacancies.

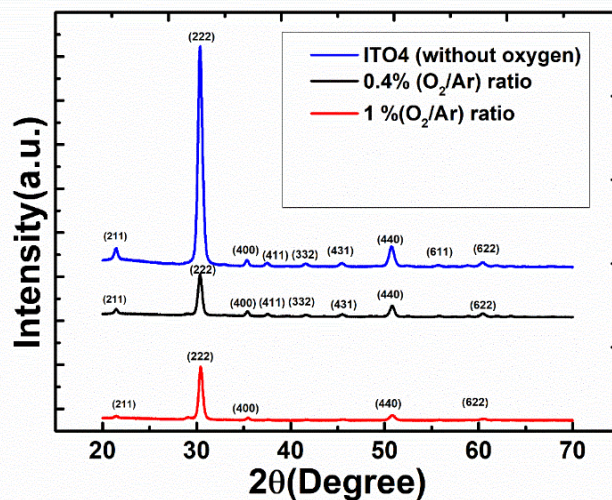


**Figure 4.9** XRD Pattern of ITO Thin Films ( As deposited ITO4, ITO23, ITO12)

### Crystallite Sizes

Crystallite sizes were calculated by using Scherrer Formula. Full Width of Half Maximum (FWHM) values were calculated from XRD graphs of ITO thin films with the help of Gaussian Fit. The results show that there is no strong correlation between annealing temperature and crystallite sizes. In Table 4.19, crystallite size, interplanar distance and Full Width of Half Maximum values of some ITO samples are given.

**Table 4.18** Crystallite size, interplanar distance and FWHM values of deposited films.

Sample Code	Annealing Temperature (°C)	2 $\theta$	FWHM	Crystallite size (nm)	d <sub>222</sub> (Å)
ITO4	As deposited	30.38	0.5	17.21	2.94
ITO4	150	30.32	0.59	14.58	2.94
ITO4	175	30.36	0.505	17.04	2.94
ITO4	200	30.33	0.57	15.09	2.94
ITO12	As deposited	30.40	0.54	15.93	2.93
ITO12	150	30.38	0.48	17.93	2.93
ITO12	175	30.35	0.47	18.31	2.94
ITO12	200	30.38	0.47	18.31	2.94
ITO12	225	30.36	0.48	17.92	2.94

### 4.4 AFM Measurements

To investigate the effect of deposition parameters and post annealing process on the surface topography of ITO films, AFM images of ITO film deposited with different parameters were taken. AFM images of ITO thin films showed that the depending on the oxygen content the surface roughness of the film and topography was going to change. In addition, the post-annealing process yielded to slight difference in surface roughness and topography.

In Figure 4.10, 4.11 and 4.12, AFM images of ITO thin films deposited with different  $O_2/Ar$  ratio are given. There are some differences between the AFM images related to oxygen content and annealing temperature. ITO films grown with 1%  $O_2/Ar$  ratio have more columnar structure than those grown without oxygen. Oxygen content might affect the surface topography of the films [77]. However, ITO films grown with 0.4 %  $O_2/Ar$  ratio has not notable columnar structure. In this sample, effect of oxygen content on the film properties decrease.

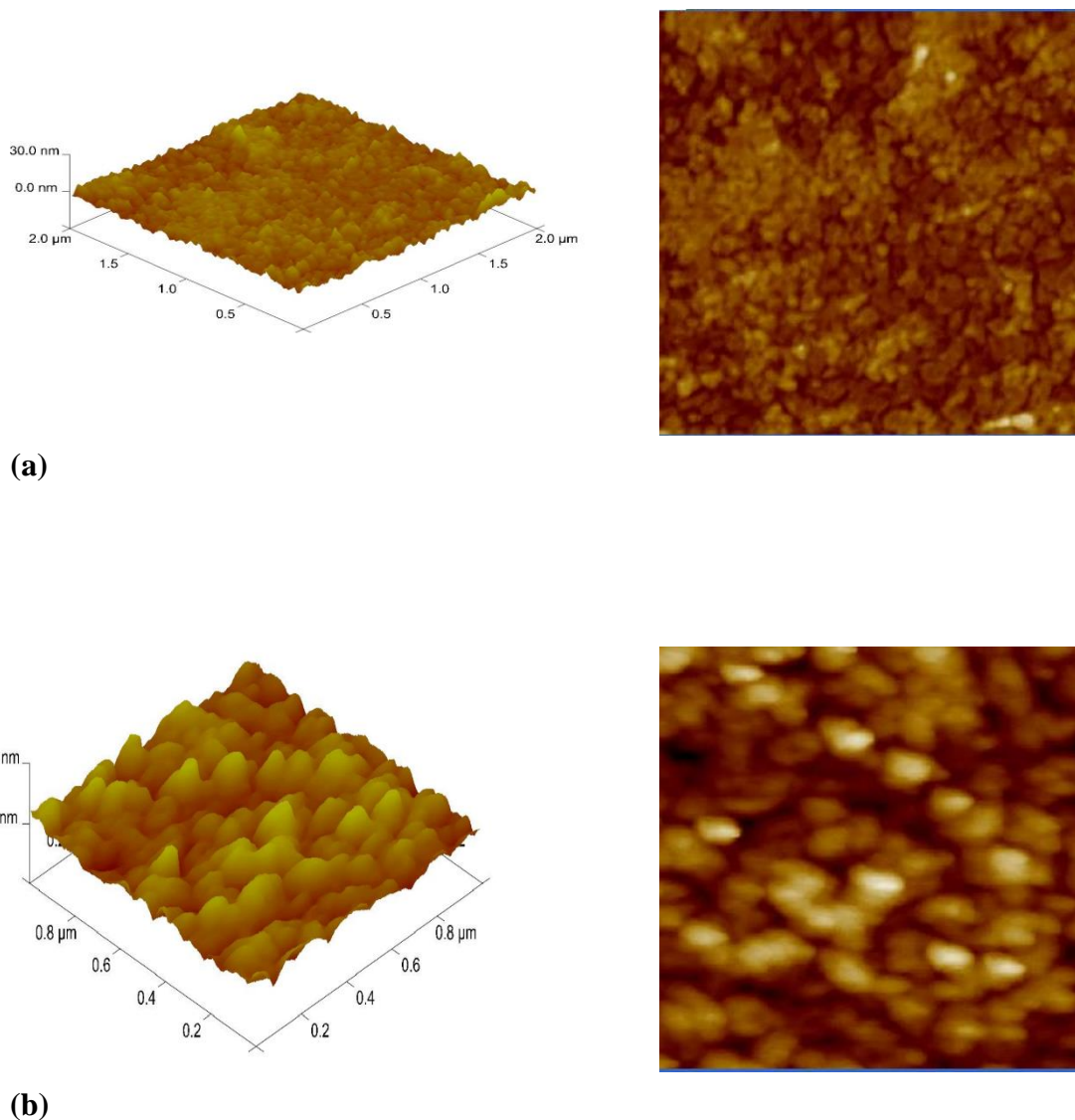
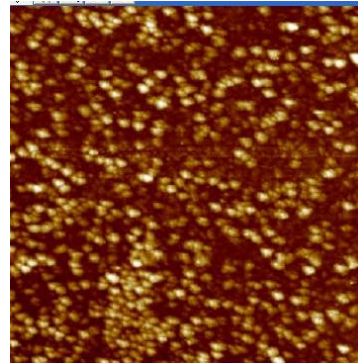
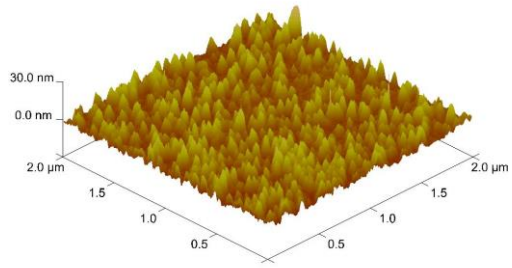
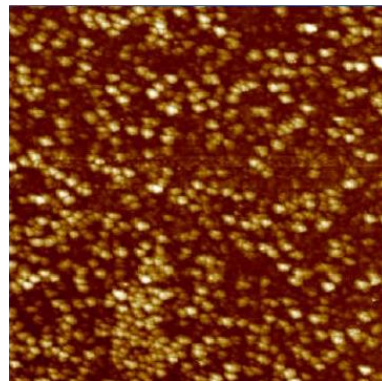
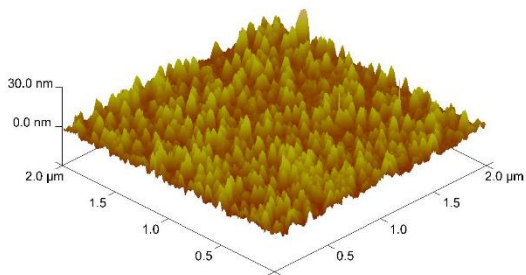


**Figure 4.10** AFM Image of ITO4 (reference) sample (a) without annealing, (b) annealed at 225 °C.

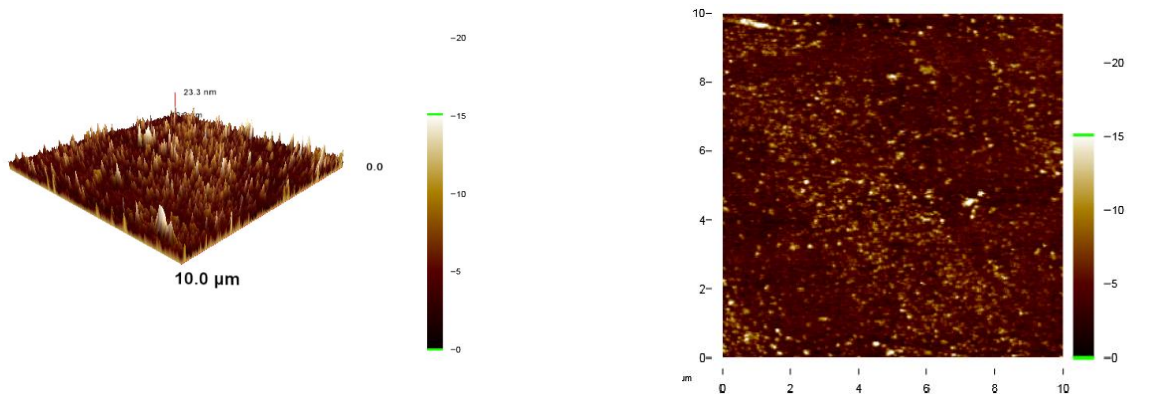


(a)

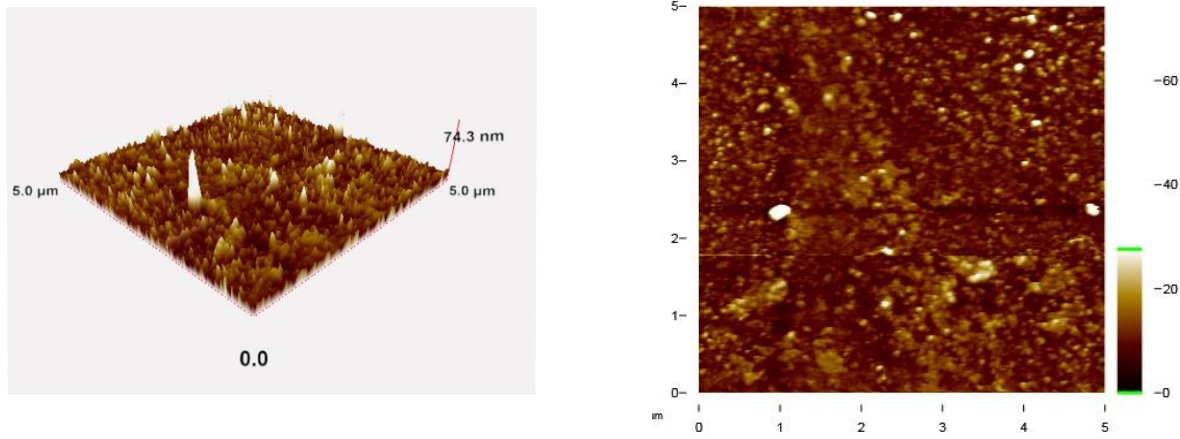


(b)

**Figure 4.11** AFM Image of ITO12 sample grown with 1 % O<sub>2</sub>/Ar ratio (a) without annealing, (b) annealed at 225 °C.



(a)



(b)

**Figure 4.12** AFM Image of ITO23 sample grown with 0.4% O<sub>2</sub>/Ar ratio (a) without annealing, (b) annealed at 225 °C.

Surface roughness of the films were obtained by using the root mean square (RMS) and there are no big differences between of surface roughness values as deposited and annealed samples. Also, O<sub>2</sub>/Ar ratio did not make important alteration on the surface roughness values. In table 4.19, surface roughness values of different ITO samples for different annealing temperature are given. The surface roughness of the samples changes between 1.88-3.03 nm. Surface roughness values of ITO12 sample (O<sub>2</sub>/Ar ratio is 1%), has more rough surface than those grown without oxygen. Moreover, surface roughness value of ITO23 sample (deposited with 0.4 % O<sub>2</sub>/Ar ratio) has lower surface roughness value than surface roughness of ITO12. In this sample, effect of oxygen content can be negligible. Although surface roughness

values and surface topography are affected by the deposition parameters, the surface roughness of ITO thin films can be considered in the negligible range.

**Table 4.19** Surface Roughness values of ITO films with and without post annealing.

<b>Sample Code</b>	<b>Surface Roughness (nm)</b>	<b>Annealing Temperature (°C)</b>	<b>Surface Roughness After Annealing (nm)</b>
<b>ITO4</b>	1.93	225	2.34
<b>ITO12</b>	3.03	225	3.03
<b>ITO23</b>	1.88	225	2.34

## **4.5 Optical Measurements**

Optical measurements were carried out using the transmission and absorption spectra and including calculated optical bandgap values of ITO films. However, in this study, only the bandgap values of as-deposited samples were presented since notable effect of post annealing temperature on the bandgap values was not measured.

### **4.5.1 UV-Visible Spectra**

Transmission and absorption spectra of ITO thin films are obtained typically as 85 - 90 % in the visible range of the spectrum. In Figure 4.13, transmittance and absorption spectra of as deposited ITO4, ITO5 and ITO6 films are given. Due to the thickness differences of the films, interference fringes were observed in some of the transmission spectra of the ITO samples. Moreover, as presented in Figure 4.13, transmission of ITO films sharply decreases in the wavelength range 300 nm.

In addition, for some ITO samples, it is possible to observe the influence of oxygen content on the transmission spectra (Figure 4.14). Increment of oxygen content gave rise to the decrease of optical transmittance of the film. Thus, oxygen content affects the optical properties of ITO thin films, as well as its electrical properties.

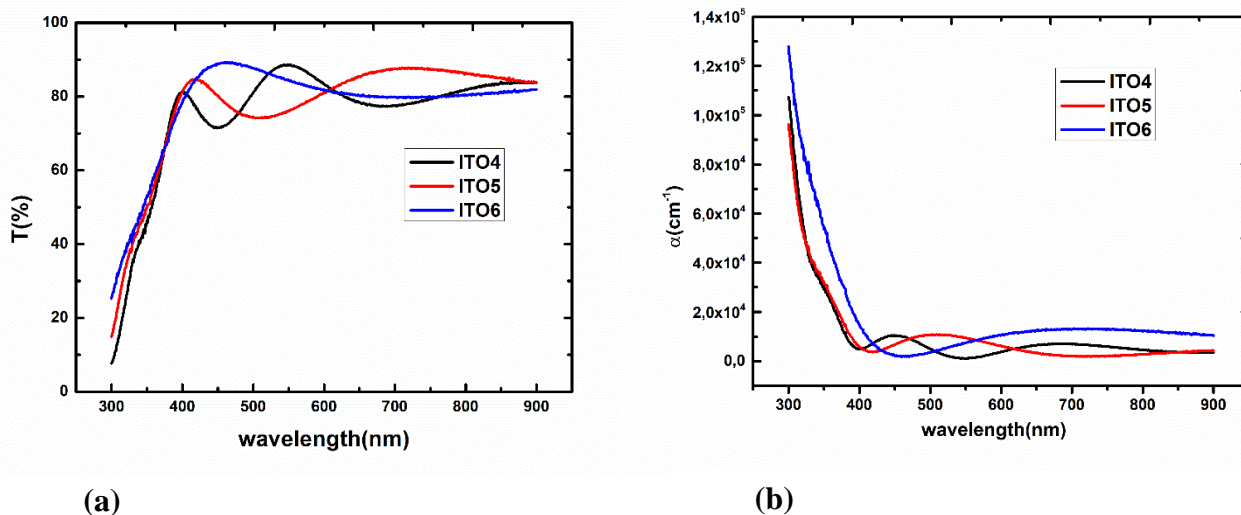


**Figure 4.13** Transmission (a) and Absorption (b) Spectra of ITO4, ITO5 and ITO6 samples.

*\*In Figure 4.13, transmission and absorption spectra of ITO4, ITO5 and ITO6 samples are given. All films are deposited without oxygen and substrate temperature are 200 °C for all samples. Only changing parameter is RF power which are 400,300,200 respectively.*

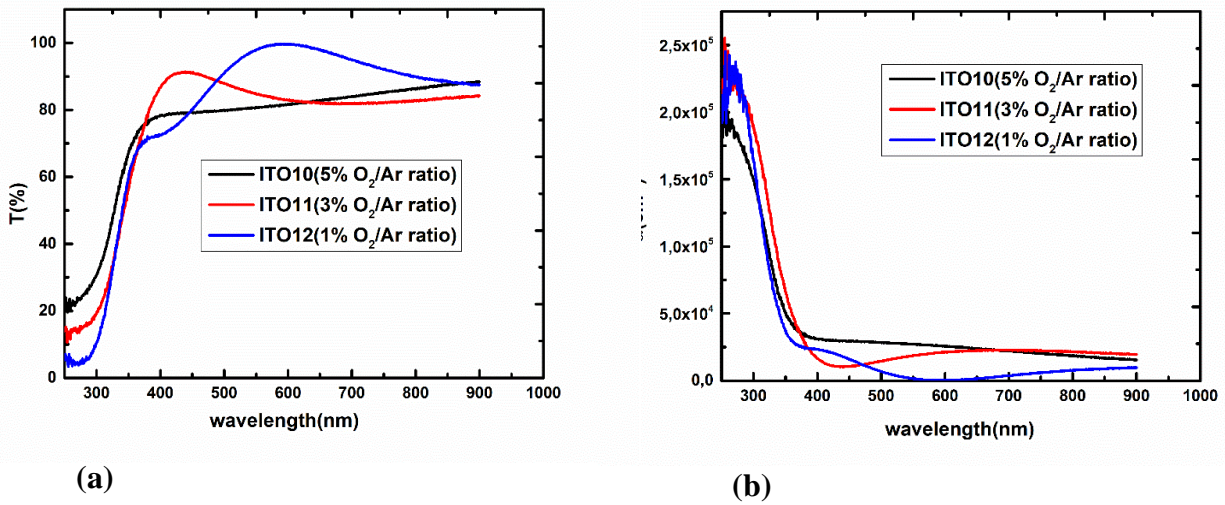


**Figure 4.14** Transmission (a) and Absorption (b) Spectra of ITO films grown with different Oxygen/Ar ratio.

*\* In Figure 4.14, transmission and absorption spectra of ITO thin film deposited with different O<sub>2</sub>/Ar ratio are given. Apart from the gas ratio, other parameters are the same as our reference sample(ITO4).*

Optical bandgap values of ITO thin films were calculated by using Tauc plots. In Figure 4.15 and 4.16, Tauc plots of ITO4, ITO5 and ITO6 samples are given for representation. The bandgap values of as deposited ITO thin films grown without oxygen changed between 3.5-3.8 eV (Table 4.21) Since ITO has bandgap range, these values are expected. According to Burstein- Moss Shift Theory, for heavily doped n type degenerate semiconductor like ITO, transmission and absorption spectra are shifted depending on the carrier concentration. In our results, the carrier concentration is related to oxygen content.[78]. Only parameter changes carrier concentration of deposited ITO films is O<sub>2</sub>/Ar ratio. Increasing oxygen content in the gas mixture decreases the carrier concentration of the films. Declination of carrier concentration leads to decrease in optical bandgap values of ITO films. The bandgap values of as deposited ITO thin films grown with oxygen change between 3.62 and 3.8 eV. Attenuation of bandgap values can be seen in Table 4.22. This can be explained by Burstein–Moss Shift Effect. However, some experimental errors during

the UV-Visible measurements can cause the unrelated bandgap values with Burstein Moss Phenomena. Also, Tauc plots of some ITO samples deposited with oxygen are given in Figure 4.17 and Figure 4.18.

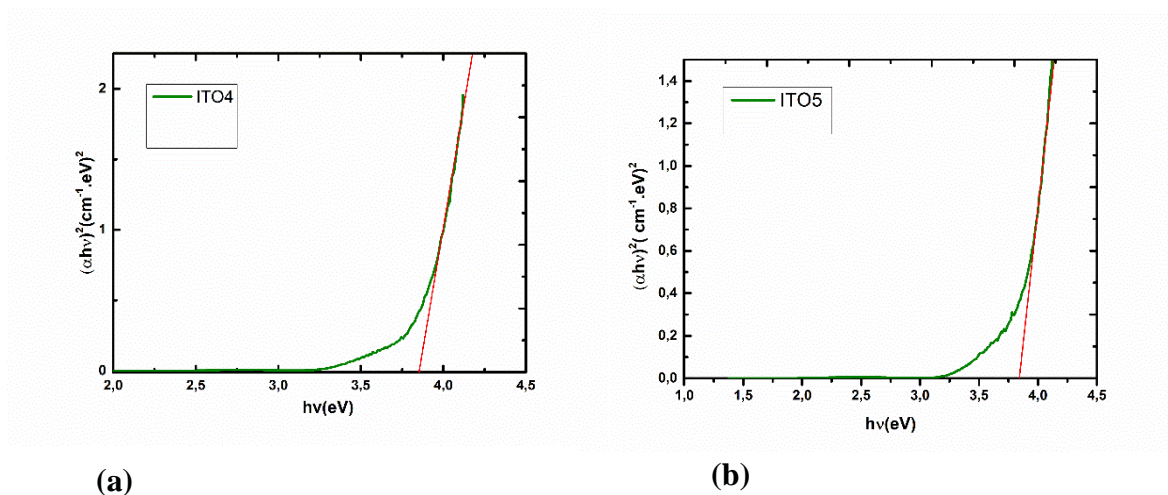


**Figure 4.15** Tauc plot of ITO4 (a) and ITO5 (b) samples.

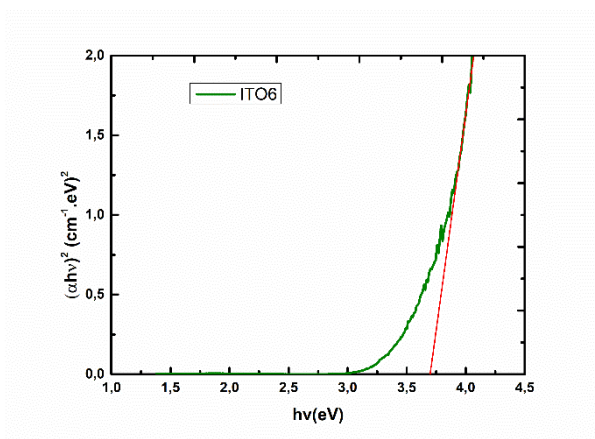
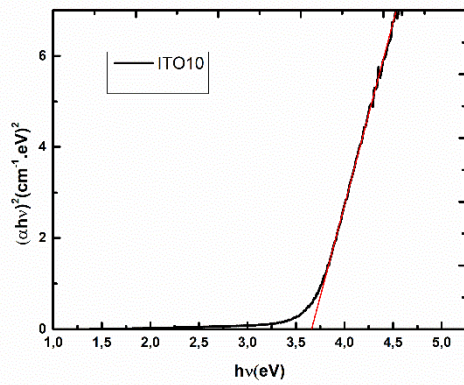


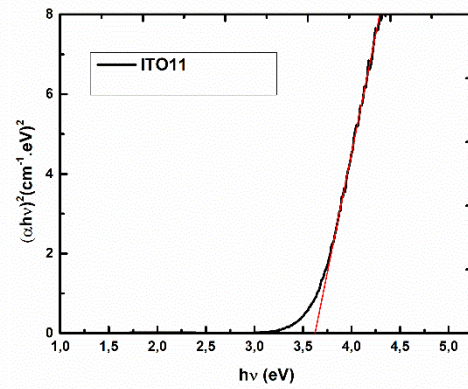
**Figure 4.16** Tauc Plot of ITO6 sample.

**Table 4.20** Optical Bandgap values as deposited ITO films deposited without oxygen.

<b>Sample Code</b>	<b>Thickness (nm)</b>	<b>Bandgap (eV)</b>	<b>Substrate Temperature ( °C)</b>	<b>RF Power (Watt)</b>	<b>Deposition Pressure (mTorr)</b>	<b>Speed (cm/min)</b>
ITO1	96	3.72	100	200	3	20
ITO2	93	3.55	100	300	3	20
ITO3	180	3.76	100	400	3	20
ITO4	230	3.79	200	400	3	20
ITO5	188	3.85	200	300	3	20
ITO6	100	3.70	200	200	3	20
ITO19	200	3.70	200	400	3	10
ITO20	236	3.61	200	400	3	15
ITO21	163	3.49	200	400	4	20
ITO22	152	3.63	200	400	2	20

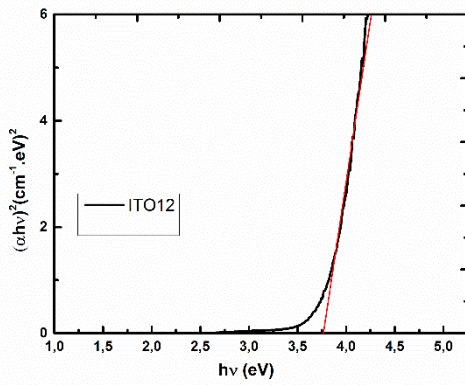


(a)

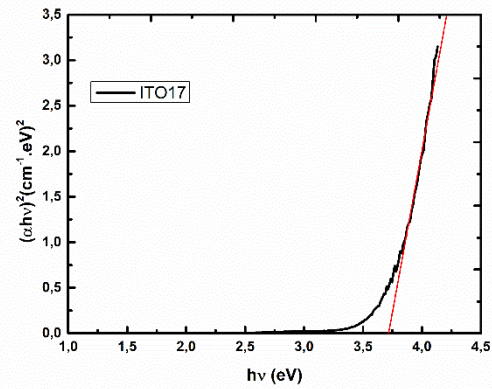


(b)

**Figure 4.17** Tauc Plot of ITO10 (a) and ITO11 (b) samples.



(a)



(b)

**Figure 4.18** Tauc Plot of ITO12 (a) and ITO17 (b) samples.

**Table 4.21** Optical bandgap of grown ITO Thin films grown with different O<sub>2</sub>/ Ar ratio.

<b>Sample Code</b>	<b>Thickness (nm)</b>	<b>O<sub>2</sub>/Ar Ratio</b>	<b>Bandgap (eV)</b>
ITO10	79	5%	3.66
ITO11	88	3%	3.62
ITO12	138	1%	3.70
ITO13	148	0.8%	3.64
ITO17	158	0.6%	3.68
ITO23	155	0.4%	3.80

#### **4.6 Contact Resistivity Analysis**

For contact resistivity analysis, TLM and Cox and Strack Method were performed to measure the contact resistivity between different layers in SHJ structure. Contact resistivity of ITO/Ag layer was calculated by using TLM. While a-Si:H layers have very high resistivity compared to ITO and metal contacts, very high contact resistivity values were obtained by using TLM [79]. The reason is that TLM may not be suitable method to measure the contact resistivity between a-Si:H/ITO layers [28]. The direction of current flow strongly affects the contact resistivity analysis. In TLM structure, the lateral current flow has been taken into account. For resistive layers like p type a-Si:H and n type a-Si:H layers, lateral current flow can affect the current flow path. For this reason, TLM may give inconsistent contact resistivity results.

#### 4.6.1 Contact Resistivity Measurements by TLM

To analyze the specific contact resistivity by TLM, I-V measurements were performed by using different mask designs given in Chapter 3. From the measured I-V graphs, contact resistance, specific contact resistivity and transfer length values were calculated for different mask designs.

##### ITO/Ag contact resistivity

For different contact designs, I-V measurements were performed to calculate ITO/Ag layer specific contact resistivity (Chapter 3, Figure 3.14). I-V characteristic of ITO/Ag layer is linear and there is a relationship between distance and resistance which can be seen from Figure 4.19. For specific contact resistivity analysis, ITO films were deposited with the standard recipe used for the deposition of ITO4. Deposition parameters of doped a-Si:H layers were the same except the deposition time. In Figure 4.19 I-V measurement results for different contact designs are given.

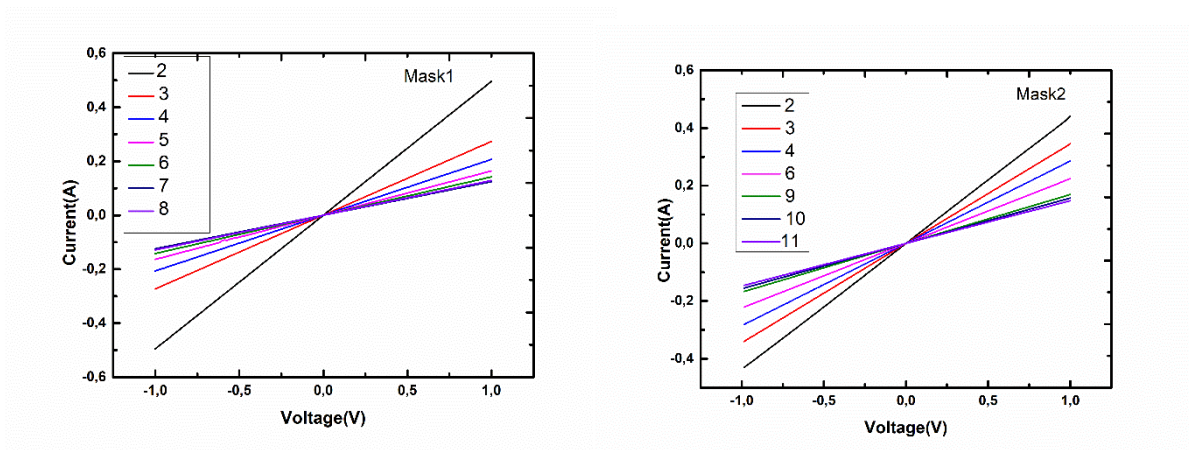


**Figure 4.19** I-V characteristic of TLM patterns with different contact diameters.

\*The numbers shown in Figure 4.21 represents the contact numbers with different contact separation. Contact design for different masks are shown in Chapter 3, Figure 3.14.

Using the I-V measurements, from the graph of resistance vs. contact separation, specific contact resistivity values of ITO/Ag layer were extracted. In Figure 4.20a and 4.20b resistance vs. contact separation graphs for different mask designs are shown. Cross section of the test structure and contact design are shown in Figure 4.20.c and 4.20.d as a reminder.

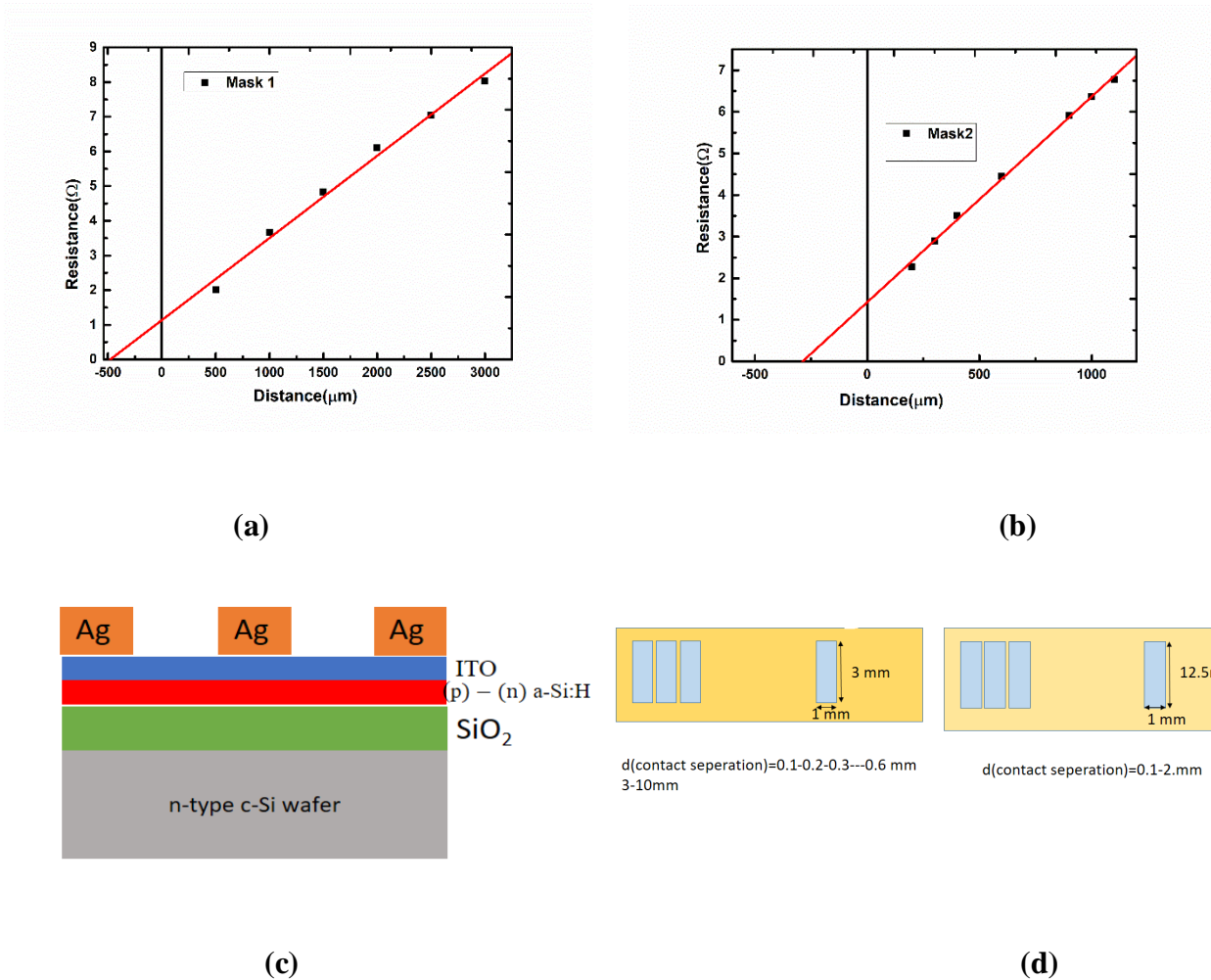


**Figure 4.20** (a) and (b) Resistance vs. contact separation graphs (c) designed test structure, (d) contact designs.

Resultant specific contact resistivity values from above graphs were in the order of  $10^{-3} \Omega \cdot \text{cm}^2$  and  $10^{-4} \Omega \cdot \text{cm}^2$ , which was consistent with the literature [30]. However,

due to the contact designs, there are some differences between the contact resistivity values (Table 4.23). Apart from contact resistance, contact resistivity should be independent from contact length and contact width, but in our results, slight differences are observed between the different contact designs. The reason may be related to standard deviation of 1 dimensional TLM analysis [67]. In Table 4.23, transfer length, contact resistance and specific contact results are given.

Since n type Si wafers were used as a base material for contact resistivity analysis, it leads to some current loss due to the blanked, opposite direction of current flow occurs [72]. To prevent current loss to the opposite direction, intrinsic and doped p-a Si:H layers deposited onto rear side of the wafer. For ITO/Ag layer, this structure gives consistent results. I-V graphs, the test structure and resistance vs. distance graph related with this structure is given in Figure 4.21.

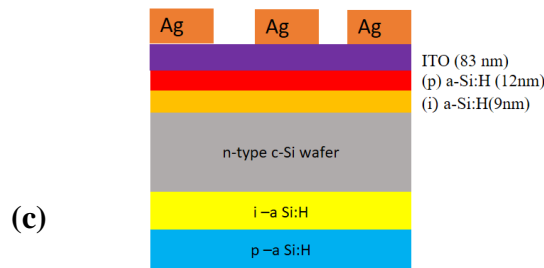
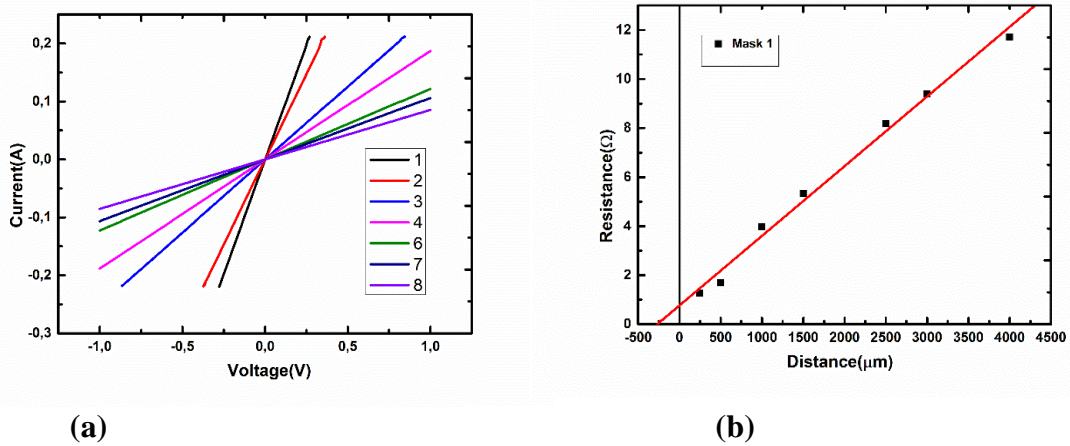


**Figure 4.21** (a) I-V measurements of TLM test structure with passivating layer for ITO/Ag layer (b) Resistance vs Distance graph, (c) cross view of test structure.

**Table 4.22** Transfer length, contact resistance and contact resistivity of ITO/Ag layer.

Sample Code	Transfer Length ( $\mu\text{m}$ )	Contact Resistance ( $\Omega$ )	Contact Resistivity ( $\Omega\cdot\text{cm}^2$ )
Mask 1	235	0.57	$8 \times 10^{-3}$
Mask 2	145	0.71	$3 \times 10^{-3}$
Mask 1	328	0.36	$7 \times 10^{-3}$
Mask 2	87	0.24	$6 \times 10^{-4}$
Mask1 (Passivating layer)	136	0.38	$3.1 \times 10^{-3}$

#### **ITO/a-Si:H contact resistivity**

Even though TLM gives reliable results for the ITO/Ag specific contact resistivity, by using TLM, we obtained very high specific contact resistivity values for ITO and a-Si:H layers. Resistivity values of ITO/a-Si:H layers were in the order  $10^5, 10^6 \Omega\cdot\text{cm}^2$ . In literature, different methods were tried to measure contact resistivity between ITO and a-Si:H layers by using different test structures [31]. In our first experiment design,  $\text{SiO}_2$  layer was used to prevent current loss to the opposite direction. However, calculated specific contact resistivity values were not representing the experimental expectations.

In the second experiment design, intrinsic and p a-Si:H layer were deposited onto rear side of the wafer to improve passivation quality and decrease current loss. In Figure 4.22, the test structure and I-V graph of this structure is given. Although passivating layer was coated on rear side of the wafer, we could not get rid of s shape structure of I-V graphs. For this reason, only linear part of I-V measurements were taken into account for TLM calculation. To get rid of the s shape and calculate specific contact resistivity between ITO/p a-Si:H layer, temperature dependent I-V measurements can be taken into consideration [80].

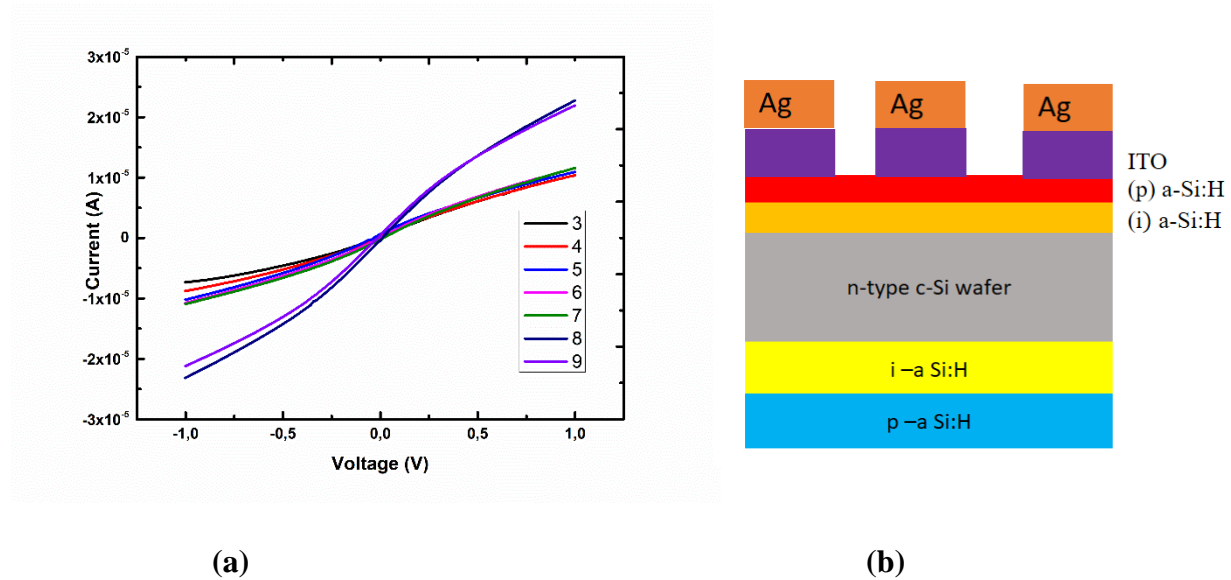


**Figure 4.22** (a) I-V characteristic of TLM test structure with passivating layer to determine specific contact resistivity of ITO/p a-Si:H layer  
 (b) schematic view of the structure.

#### 4.7 SHJ Cells Results

Two different SHJ cells were deposited by changing only the deposition parameters of ITO layer. In the first deposition, deposition parameters of our standard recipe used for representative samples was used for ITO deposition. In the second SHJ cell deposition cycle, best reactive sputtering parameters (ITO17 sample) were chosen and effect of ITO layer on SHJ cell performance was investigated.

##### **EQE Results of SHJ cells with Different ITO Layers**

To investigate effect of ITO layer on the SHJ cell performance, external quantum efficiency measurements were performed. In the first SHJ cell deposition cycle, ITO layer was deposited by using our standard recipe with a thickness of 77 nm. In the second SHJ cell deposition, the best reactive sputtering parameter was used during

the ITO deposition (ITO17). ITO17 sample deposited with 0.6 % Oxygen/Argon ratio and other parameters were the same as our standard recipe. This sample have highest mobility and lower carrier density compared to our reference ITO film. For this ITO layer, thickness was around 74 nm which was slightly lower than the anti-reflective coating layer. This showed that the sample with reactively sputtered ITO layer has slightly high reflectance loss compared to other. Despite the lower thickness of ITO layer, effect of ITO layer on SHJ cells can be seen from EQE graphs. In the first cell, parasitic absorption is higher than compared the second one. Decrease in free carrier absorption in NIR region can be explained by low carrier density of ITO film deposited with reactive sputtering.

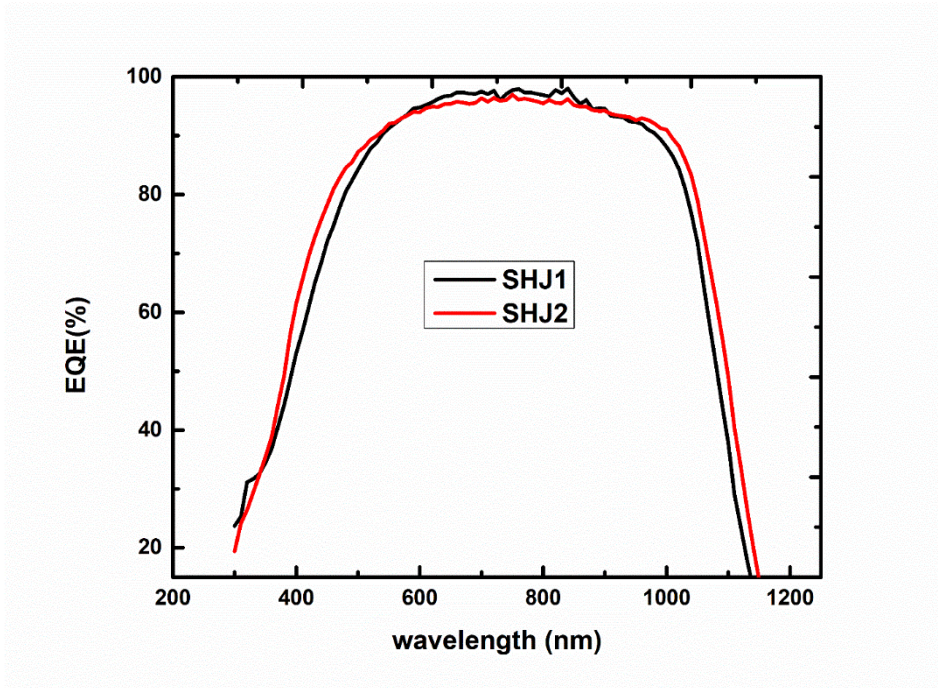


**Figure 4.23** EQE results of SHJ cells deposited with different ITO layer.

### **I-V characteristics**

I-V characteristics of SHJ cells were performed by solar simulator with an area of 156x156 cm<sup>2</sup>. Current density of the first cell was equal to 37.49 mA/cm<sup>2</sup>, while current density of the second cell was 38.08 mA/cm<sup>2</sup>. The enhancement of Jsc value two is related to decrease in free carrier absorption and parasitic absorption by

reactive sputtering and also mobility values have impact on the improvement of  $J_{sc}$  value. ITO film deposited with reactive sputtering (sputtering with both oxygen and argon content) had highest mobility ( $30 \text{ cm}^2/\text{V} \cdot \text{s}$ ) between the deposited films. Increase in mobility implied to improvement of carrier transport mechanism a-Si:H layers. For this reason,  $J_{sc}$  value slightly increases [81].

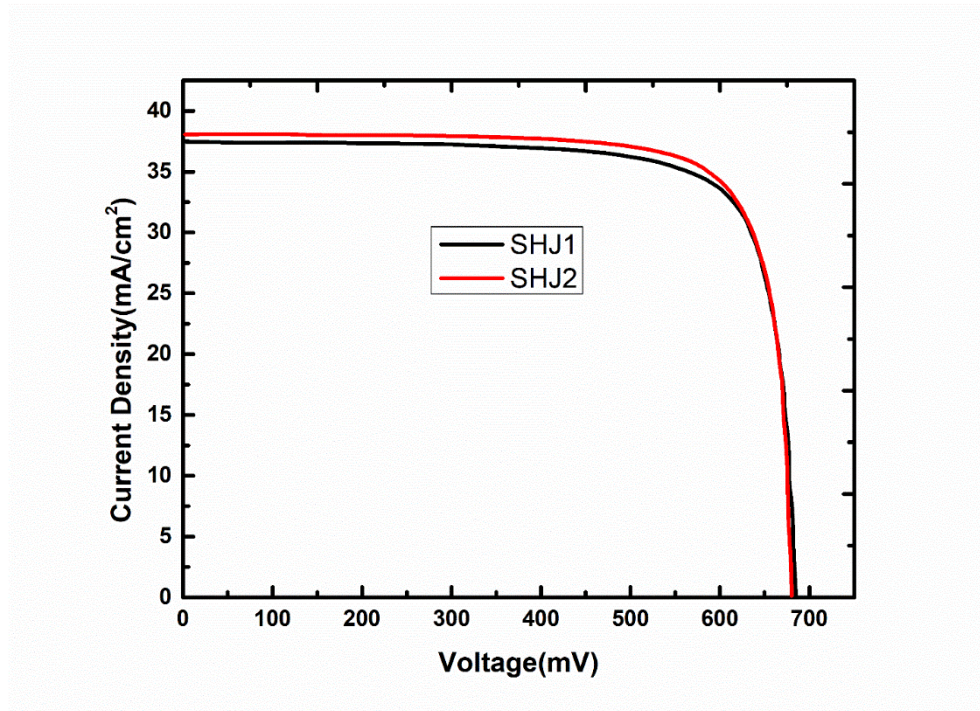


**Figure 4.24** I-V characteristic of SHJ cells deposited with different ITO layer.

### Cell Parameters

In Table 4.24, results of SHJ cell parameters deposited with two different ITO layers are given. In both cells, Fill Factor values are the same; however, other parameters are variable due to the ITO layer properties. Shunt resistance are almost same for the two samples; however, there is a certain difference between series resistance values. This differences cannot be explained conclusively with the data at hand.  $V_{oc}$  value of first cell is higher than second cell. This differences are related to small variation

of passivation quality of intrinsic a-Si:H layer. Power conversion efficiency of second cell is a bit more from the first cell which is related to differences of short circuit current density values.

**Table 4.24** SHJ cell parameters.

<b>Sample Code</b>	<b>Voc (mV)</b>	<b>Jsc (mA/cm<sup>2</sup>)</b>	<b>FF (%)</b>	<b>R<sub>shunt</sub> (Ω)</b>	<b>R<sub>series</sub> (Ω)</b>	<b>Efficiency (%)</b>
SHJ1	685	37.45	78.63	108251	0.75	20.17
SHJ2	681	38.06	79.38	106312	0.31	20.56

In this study, optimization studies of ITO thin films were performed for use as an anti-reflective coating layer in SHJ cells. Afterwards, two different optimized ITO layers were used for SHJ cells and effect of ITO layer on SHJ cell performance were investigated. Besides the optimization studies of ITO layer, contact resistivity studies were performed for different layer in SHJ cells. However, a certain method cannot be determined to measure contact resistivity between ITO/a-Si:H layers in SHJ structure even though contact resistivity of ITO/Ag layer was extracted from TLM.

## CHAPTER 5

### CONCLUSION

In this study, to enhance SHJ cell performance, characterization and optimization studies of ITO thin films as TCO layer were carried out. The main aim was to find suitable deposition parameters in order to be able to use ITO as anti-reflective coating layer in SHJ structures. To find the optimum deposition parameters for the ITO films, several sets of depositions were performed. The films were deposited onto borosilicate glass substrates as well as n-type wafers by RF magnetron sputtering. Various deposition parameters such as, RF power, deposition pressure, substrate temperature, O<sub>2</sub>/Ar ratio, and deposition pressure, were tested for the sputtering process. The deposition parameter which has the strongest effect on the film properties, is the O<sub>2</sub>/Ar ratio. Changing O<sub>2</sub>/Ar ratio led to changes in electrical, optical and structural properties of the ITO thin films.

After each ITO deposition, in order to determine the optimum ITO film properties matching the anti-reflective layer properties in SHJ, the films were characterized by different techniques. For ITO thin films deposited without oxygen, the most suitable parameters in terms of RF power, substrate temperature and deposition pressure were determined as 400 W, 200 °C, 3 mTorr. For the ITO films with reactively deposited (including oxygen), the O<sub>2</sub>/Ar ratio was varied while the other parameters were kept constant. The optimum O<sub>2</sub>/Ar ratio was found to be 0.6 %. ITO film deposited with this parameter had maximum mobility while its carrier density was lower by one order of magnitude than that of ITO films grown without oxygen. For this reason, the ITO films deposited with these deposition parameters were applied in SHJ cells fabrication. The effect of the ITO layer on SHJ cells parameters were investigated.

Two SHJ cells were fabricated using two different ITO layers. In the first cell deposition, the previously determined optimum deposition parameters of ITO film

were applied, however no oxygen was added to the sputter gas. For the second cell, besides the optimum parameters, the ITO layer was deposited with 0.6 % O<sub>2</sub>/Ar ratio. The results demonstrated that carrier density and mobility values of ITO thin films have an effect on the SHJ parameters. The SHJ cell fabricated using ITO with reactive (including oxygen) sputtering had a low free carrier absorption in the NIR region which affects the collection of charge carriers. Conversion efficiency of the SHJ cell deposited with reactive sputtering is 20.56 % while conversion efficiency of the SHJ cell deposited with reference ITO is 20.17 %. Also, there was an increase of J<sub>sc</sub> value in the second cell. These differences were related to decreasing free carrier absorption in the NIR region.

In this study, in addition to optimization and characterization studies of ITO thin films, specific contact resistivity studies were performed by using TLM. Specific contact resistivity of ITO/Ag layer was calculated via TLM. Corresponding specific contact resistivity values of ITO/Ag layer are in the order of mΩ.cm<sup>2</sup> which is consistent with the literature. On the other hand, this method did not give reliable specific contact resistivity results for other layers in SHJ structure.

## REFERENCES

- [1] M. Ratner, 'The Physics of Solar Cells ; Third Generation Photovoltaics: Advanced Solar Energy Conversion The Physics of Solar Cells , Jenny Nelson Imperial College Press, London, 2003. \$82.00, \$46.00 paper (363 pp.). ISBN 1-86094-340-3, ISBN 1-86094-349-7 paper Thir', *Phys. Today*, 2004.
- [2] D. J. HARRIS and P. N. ROBSON, 'Fundamentals of Solid State Electronics', in *The Physical Basis of Electronics*, 1974.
- [3] 'Poly vs Mono Crystalline | Tindo Solar'. [Online]. Available: <https://www.tindosolar.com.au/learn-more/poly-vs-mono-crystalline/>. [Accessed: 03-Nov-2019].
- [4] M. Powalla, S. Paetel, E. Ahlswede, R. Wuerz, C. D. Wessendorf, and T. Magorian Friedlmeier, 'Thin-film solar cells exceeding 22% solar cell efficiency: An overview on CdTe-, Cu(In,Ga)Se<sub>2</sub> -, and perovskite-based materials', *Appl. Phys. Rev.*, 2018.
- [5] T. D. Lee and A. U. Ebong, 'A review of thin film solar cell technologies and challenges', *Renewable and Sustainable Energy Reviews*. 2017.
- [6] 'Second Generation Thin Film Solar Cells'. [Online]. Available: <https://scottamyx.com/2019/05/21/second-generation-thin-film-solar-cells/>. [Accessed: 03-Nov-2019].
- [7] L. Escoubas, J. J. Simon, J. Le Rouzo, and V. Bermudez, 'Innovative approaches in thin film photovoltaic cells', in *Optical Thin Films and Coatings: From Materials to Applications*, 2013.
- [8] W. Shockley, H. Queisser, and H. J. Queisser, 'The Shockley-Queisser limit', *J. Appl. Phys.*, 1961.
- [9] 'PHOTOVOLTAICS REPORT', 2019.

- [10] ‘Complete Solid-State Dye-Sensitized Solar Cell | Global | Ricoh’. [Online]. Available: [https://www.ricoh.com/technology/tech/066\\_dssc](https://www.ricoh.com/technology/tech/066_dssc). [Accessed: 03-Nov-2019].
- [11] NREL, ‘Best Research-Cell Efficiency Chart | Photovoltaic Research | NREL’, *National Renewable Energy Laboratory*, 2019. .
- [12] W. Fuhs, K. Niemann, and J. Stuke, ‘HETEROJUNCTIONS OF AMORPHOUS SILICON AND SILICON SINGLE CRYSTALS.’, in *AIP Conf Proc*, 1974.
- [13] T. Kanbara *et al.*, ‘Amorphous Si / Polycrystalline Si Stacked Solar Cell Having More Than 12 % Conversion Efficiency’, 1983.
- [14] M. Tanaka *et al.*, ‘Development of new a-si/c-si heterojunction solar cells: Acj-hit (artificially constructed junction- heterojunction with intrinsic thin-layer)’, *Jpn. J. Appl. Phys.*, 1992.
- [15] D. Adachi, J. L. Hernández, and K. Yamamoto, ‘Impact of carrier recombination on fill factor for large area heterojunction crystalline silicon solar cell with 25.1% efficiency’, *Appl. Phys. Lett.*, 2015.
- [16] J. Haschke, O. Dupré, M. Boccard, and C. Ballif, ‘Silicon heterojunction solar cells: Recent technological development and practical aspects - from lab to industry’, *Sol. Energy Mater. Sol. Cells*, vol. 187, no. August, pp. 140–153, 2018.
- [17] ‘Sanyo (now Panasonic) Sanyo HIT-195BA20 195-watt solar panel Solar Panel - Wholesale Solar’. [Online]. Available: [www.wholesalesolar.com/1941970/sanyo-now-panasonic/solar-panels/sanyo-now-panasonic-sanyo-hit-195ba20-195-watt-solar-panel-solar-panel](http://www.wholesalesolar.com/1941970/sanyo-now-panasonic/solar-panels/sanyo-now-panasonic-sanyo-hit-195ba20-195-watt-solar-panel-solar-panel). [Accessed: 09-Nov-2019].
- [18] K. Badeker, ‘fiber d&e elelctrische Leitf&hdgkedt und die themnoelektrische E’raft eimiger Sch wermetal Luerbindungew ; von’, *Ann. Phys.*, vol. 22, pp.

749–766, 1907.

- [19] H. Park *et al.*, ‘Front and Back TCO Research Review of a-Si/c-Si Heterojunction with Intrinsic Thin Layer (HIT) Solar Cell’, *Trans. Electr. Electron. Mater.*, vol. 19, no. 3, pp. 165–172, 2018.
- [20] R. K. Gupta, K. Ghosh, and P. K. Kahol, ‘Thickness dependence of optoelectrical properties of tungsten-doped indium oxide films’, *Appl. Surf. Sci.*, vol. 255, no. 21, pp. 8926–8930, 2009.
- [21] A. Thøgersen, M. Rein, E. Monakhov, J. Mayandi, and S. Diplas, ‘Elemental distribution and oxygen deficiency of magnetron sputtered indium tin oxide films’, *J. Appl. Phys.*, vol. 109, no. 11, 2011.
- [22] G. Rupprecht, ‘Untersuchungen der elektrischen und lichtelektrischen Leitfähigkeit dünner Indiumoxydschichten’, *Zeitschrift für Phys.*, 1954.
- [23] I. A. Rauf, ‘Structure and properties of tin-doped indium oxide thin films prepared by reactive electron-beam evaporation with a zone-confining arrangement’, *J. Appl. Phys.*, 1996.
- [24] S. Q. Hussain *et al.*, ‘RF magnetron sputtered indium tin oxide films with high transmittance and work function for a-Si:H/c-Si heterojunction solar cells’, *Vacuum*, vol. 101, pp. 18–21, 2014.
- [25] G. Phipps, C. Mikolajczak, and T. Guckes, ‘Indium and Gallium: long-term supply’, *Renew. Energy Focus*, 2008.
- [26] L. Kerkache, A. Layadi, E. Dogheche, and D. Rémiens, ‘Physical properties of RF sputtered ITO thin films and annealing effect’, *J. Phys. D. Appl. Phys.*, vol. 39, no. 1, pp. 184–189, 2006.
- [27] D. Das and L. Karmakar, ‘Further optimization of ITO films at the melting point of Sn and configuration of Ohmic contact at the c-Si/ITO interface’, *Appl. Surf. Sci.*, vol. 481, no. March, pp. 16–24, 2019.

- [28] B. Demaurex, ‘Passivating contacts for homojunction solar cells using a-Si : H / c-Si hetero-interfaces’, École Polytechnique Federale de Lausanne, 2014.
- [29] R. Gogolin *et al.*, ‘Analysis of series resistance losses in a-Si:H/c-Si heterojunction solar cells’, *IEEE J. Photovoltaics*, vol. 4, no. 5, pp. 1169–1176, 2014.
- [30] S. Y. Lee *et al.*, ‘Analysis of a-Si:H/TCO contact resistance for the Si heterojunction back-contact solar cell’, *Sol. Energy Mater. Sol. Cells*, vol. 120, no. PART A, pp. 412–416, 2014.
- [31] M. Leilaoui, W. Weigand, M. Boccard, Z. J. Yu, K. Fisher, and Z. C. Holman, ‘Contact Resistivity of the p-Type Amorphous Silicon Hole Contact in Silicon Heterojunction Solar Cells’, *IEEE J. Photovoltaics*, 2019.
- [32] W. Shockley, ‘RESEARCH AND INVESTIGATION OF INVERSE EPITAXIAL UHF POWER TRANSISTORS’, 1964.
- [33] G. Oliveti, L. Marletta, N. Arcuri, M. De Simone, R. Bruno, and G. Evola, ‘Solar Energy’, pp. 159–214, 2014.
- [34] M. A. Green, *Solar Cells: Operating Principles, Technology, and System Applications*. Englewood Cliffs: Prentice-Hall, Inc., 1982.
- [35] C. Hornsberg and S. Bowden, ‘Silicon Solar Cell Parameters | PVEducation’, *PV Education*, 2018. .
- [36] E. Dönerçark, ‘Surface Preparation, Passivation and Patterning Techniques used in Silicon Based Solar Cells’, Middle East Technical University, 2017.
- [37] ‘Physics of Solar Cells’. [Online]. Available: [http://depts.washington.edu/cmditr/modules/opv/physics\\_of\\_solar\\_cells.html](http://depts.washington.edu/cmditr/modules/opv/physics_of_solar_cells.html) . [Accessed: 06-Jan-2020].
- [38] P. K. Nayak, S. Mahesh, H. J. Snaith, and D. Cahen, ‘Photovoltaic solar cell technologies: analysing the state of the art’, *Nat. Rev. Mater.*, 2019.

- [39] S. DeWolf, A. Descoedres, Z. C. Holman, and C. Ballif, 'High-efficiency silicon heterojunction solar cells: A review', *Green*, vol. 2, no. 1, pp. 7–24, 2012.
- [40] M. Taguchi *et al.*, '24.7% Record efficiency HIT solar cell on thin silicon wafer', *IEEE J. Photovoltaics*, vol. 4, no. 1, pp. 96–99, 2014.
- [41] W. R. Fahrner, *Amorphous Silicon Heterojunction Solar Cells*. 2001.
- [42] D. Rached and R. Mostefaoui, 'Influence of the front contact barrier height on the Indium Tin Oxide/hydrogenated p-doped amorphous silicon heterojunction solar cells', *Thin Solid Films*, vol. 516, no. 15, pp. 5087–5092, 2008.
- [43] P. Drude, 'No Title', *Ann. Phys.(4)*, vol., p. 306 (566), 1900.
- [44] W. Zawadzki, *Handbook on Semiconductor*. 1982.
- [45] T. Pisarkiewicz, K. Zakrzewska, and E. Leja, 'Scattering of charge carriers in transparent and conducting thin oxide films with a non-parabolic conduction band', *Thin Solid Films*, vol. 174, no. PART 1, pp. 217–223, 1989.
- [46] J. Y. W. Seto, 'The electrical properties of polycrystalline silicon films', *J. Appl. Phys.*, 1975.
- [47] C. Erginsoy, 'Neutral Impurity Scattering in Semiconductors', pp. 118–121, 1950.
- [48] D. Mergel and Z. Qiao, 'Correlation of lattice distortion with optical and electrical properties of In<sub>2</sub>O<sub>3</sub>:Sn films', *J. Appl. Phys.*, vol. 95, no. 10, pp. 5608–5615, 2004.
- [49] F. S. GALASSO, 'SUMMARY OF THE STRUCTURE OF PHASES', in *Structure and Properties of Inorganic Solids*, 1970.
- [50] H. Arslan, 'Indium Tin Oxide (ITO) Coating On Cylindrical Surfaces: Electrical and Structural Characterization', no. October, p. 97s, 2015.

- [51] A. Klein *et al.*, ‘Surface potentials of magnetron sputtered transparent conducting oxides’, *Thin Solid Films*, vol. 518, no. 4, pp. 1197–1203, 2009.
- [52] A. Valla, P. Carroy, F. Ozanne, and D. Muñoz, ‘Understanding the role of mobility of ITO films for silicon heterojunction solar cell applications’, *Sol. Energy Mater. Sol. Cells*, vol. 157, pp. 874–880, 2016.
- [53] E. Burstein, ‘Anomalous optical absorption limit in InSb [4]’, *Physical Review*. 1954.
- [54] A. Chen, K. Zhu, H. Zhong, Q. Shao, and G. Ge, ‘A new investigation of oxygen flow influence on ITO thin films by magnetron sputtering’, *Sol. Energy Mater. Sol. Cells*, vol. 120, no. PART A, pp. 157–162, 2014.
- [55] S. Li, Z. Shi, Z. Tang, and X. Li, ‘Comparison of ITO, In<sub>2</sub>O<sub>3</sub>:Zn and In<sub>2</sub>O<sub>3</sub>:H transparent conductive oxides as front electrodes for silicon heterojunction solar cell applications’, *Vacuum*, vol. 145, pp. 262–267, 2017.
- [56] S. Q. Hussain *et al.*, ‘Study of Low Resistivity and High Work Function ITO Films Prepared by Oxygen Flow Rates and N<sub>2</sub>O Plasma Treatment for Amorphous/Crystalline Silicon Heterojunction Solar Cells’, *J. Nanosci. Nanotechnol.*, vol. 14, no. 12, pp. 9237–9241, 2014.
- [57] Z. Qiao, ‘Fabrication and study of ito thin films prepared by magnetron sputtering’, p. 157, 2003.
- [58] E. H. , R. H. W. Rhoderick, ‘Metal-semiconductor contacts’, *Phys. Technol.*, vol. 5, no. 4, pp. 223–223, 1988.
- [59] S. M. Sze and K. K. Ng, ‘Physics of Semiconductor Devices, 3rd Edition - Simon M. Sze, Kwok K. Ng’, *Phys. Semicond. Devices, 3rd Ed. John Wiley Sons, Inc.; NJ*, 2007.
- [60] M. F. Size, ‘Metal/Semiconductor Ohmic Contacts Technology or Gate Length Series Resistance (ohms)’, 1997.

- [61] B. G. STREETMAN and S. BANERJEE, 'Solid state electronic devices', in *Prentice Hall series in solid state physical electronics*, 2016.
- [62] BEN G. STREETMAN AND SANJAY KUMAR BANERJEE, *Solid State Electronic Devices*. 2009.
- [63] P. N. Vinod, 'Specific contact resistance measurements of the screen-printed Ag thick film contacts in the silicon solar cells by three-point probe methodology and TLM method', *J. Mater. Sci. Mater. Electron.*, 2011.
- [64] D. P. Kennedy and P. C. Murley, 'A Two-Dimensional Mathematical Analysis of the Diffused Semiconductor Resistor', *IBM J. Res. Dev.*, 2010.
- [65] H. Murrmann and D. Widmann, 'Current Crowding on Metal Contacts to Planar Devices', *IEEE Trans. Electron Devices*, 1969.
- [66] H. H. Berger, 'Contact Resistance and Contact Resistivity', *J. Electrochem. Soc.*, vol. 119, no. 4, p. 507, 2007.
- [67] D. K. Schroder, *Semiconductor Devices and Material Characterization Third Edition*, vol. 44, no. 4. 2006.
- [68] K. A. Reinhardt and W. Kern, *Handbook of Silicon Wafer Cleaning Technology*. 2018.
- [69] E.Özkol, 'Modeling and Optimization of PECVD Process and Equipment Used for Manufacturing Thin Film Photovoltaic Devices', Middle East Technical University, 2015.
- [70] 'PVE300 Photovoltaic EQE (IPCE) and IQE solution - Bentham'. [Online]. Available: <https://www.bentham.co.uk/products/systems/pve300-photovoltaic-eqe-ipce-and-iqe-solution-16/>. [Accessed: 07-Jan-2020].
- [71] M. Balestrieri, D. Pysch, J. P. Becker, M. Hermle, W. Warta, and S. W. Glunz, 'Characterization and optimization of indium tin oxide films for heterojunction solar cells', *Sol. Energy Mater. Sol. Cells*, vol. 95, no. 8, pp.

2390–2399, 2011.

- [72] W. Weigand, A. M. Leilaoui, T. Ngo, S. Mercado, and Z. C. Holman, ‘Contact resistivity of n-type amorphous silicon electron contacts in silicon heterojunction solar cells’, *2018 IEEE 7th World Conf. Photovolt. Energy Conversion, WCPEC 2018 - A Jt. Conf. 45th IEEE PVSC, 28th PVSEC 34th EU PVSEC*, pp. 3905–3907, 2018.
- [73] G. Nogay, ‘Full-Area Passivating Contacts with High and Low Thermal Budgets: Solutions for High Efficiency c-Si Solar Cells’, 2018.
- [74] P. Thilakan, C. Minarini, S. Loreti, and E. Terzini, ‘Investigations on the crystallisation properties of RF magnetron sputtered indium tin oxide thin films’, *Thin Solid Films*, vol. 388, no. 1–2, pp. 34–40, 2001.
- [75] C. Guillén and J. Herrero, ‘Polycrystalline growth and recrystallization processes in sputtered ITO thin films’, *Thin Solid Films*, vol. 510, no. 1–2, pp. 260–264, 2006.
- [76] S. T. H. and C. B. Park, ‘No Title’, *Trans. Electr. Electron. Mater.*, vol. 11, p. 81, 2010.
- [77] J. Gwamuri, M. Marikkannan, J. Mayandi, P. K. Bowen, and J. M. Pearce, ‘Influence of oxygen concentration on the performance of ultra-thin RF magnetron sputter deposited indium tin oxide films as a top electrode for photovoltaic devices’, *Materials (Basel)*, 2016.
- [78] M. Bender, W. Seelig, C. Daube, H. Frankenberger, B. Ocker, and J. Stollenwerk, ‘Dependence of oxygen flow on optical and electrical properties of DC-magnetron sputtered ITO films’, *Thin Solid Films*, vol. 326, no. 1–2, pp. 72–77, 1998.
- [79] R. P. Gupta, J. B. White, O. D. Iyore, U. Chakrabarti, H. N. Alshareef, and B. E. Gnade, ‘Determination of contact resistivity by the cox and strack method for metal contacts to bulk bismuth antimony telluride’, *Electrochem. Solid-*

*State Lett.*, 2009.

- [80] G. Nogay *et al.*, ‘Nanocrystalline Silicon Carrier Collectors for Silicon Heterojunction Solar Cells and Impact on Low-Temperature Device Characteristics’, *IEEE J. Photovoltaics*, 2016.
- [81] J. Haschke *et al.*, ‘Annealing of Silicon Heterojunction Solar Cells: Interplay of Solar Cell and Indium Tin Oxide Properties’, *IEEE J. Photovoltaics*, vol. 9, no. 5, pp. 1202–1207, 2019.







